Cooling and Cooperative Coupling of Single Atoms in an Optical Cavity

Dissertation

zur
Erlangung des Doktorgrades (Dr. rer. nat.)
der
Mathematisch-Naturwissenschaftlichen Fakultät
der
Rheinischen Friedrich-Wilhelms-Universität Bonn

vorgelegt von

René Reimann

aus
Bamberg in Oberfranken

Bonn 2014

Angefertigt mit Genehmigung
der Mathematisch-Naturwissenschaftlichen Fakultät
der Rheinischen Friedrich-Wilhelms-Universität Bonn

1. Gutachter: Prof. Dr. Dieter Meschede
2. Gutachter: Prof. Dr. Stephan Schlemmer

Tag der Promotion: 05. November 2014

Erscheinungsjahr: 2014

Abstract

In this work the motional state of single cesium atoms strongly coupled to an optical high-finesse cavity is controlled and manipulated by a novel Raman cooling scheme. Furthermore, cavity-modified super- and subradiant Rayleigh scattering of two atoms is observed and explained by collective coupling of the atoms to the cavity mode.

We start with the description and comparison of different intra-cavity cooling schemes that allow us to control the motional states of atoms. Cavity cooling is experimentally and theoretically investigated for the two cases of pumping the cavity and driving the atom. In contrast to other cooling schemes, such as EIT- or Raman cooling, our analysis shows that we cannot use cavity cooling for efficient ground-state preparation, but it serves as a precooling scheme for the sideband-cooling methods. Comparing the more efficient sideband cooling techniques EIT and Raman cooling, we find that the experimental efficiency of EIT cooling could not be determined.

Therefore we choose a novel, easily implemented Raman cooling technique that features an intrinsic suppression of the carrier transition. This is achieved by trapping the atom at the node of a blue detuned intra-cavity standing wave dipole trap that simultaneously acts as one field for the two-photon Raman coupling. We apply this method to perform carrier-free Raman cooling to the two-dimensional vibrational ground state and to coherently manipulate the atomic motion. The motional state of the atom after Raman cooling is extracted by Raman spectroscopy using a fast and non-destructive atomic state detection scheme, whereby high repetition rates and good signal-to-noise ratios of sideband spectra are achieved.

In a last experiment we observe cooperative radiation of exactly two neutral atoms strongly coupled to our cavity. Driving both atoms with a common laser beam, we measure super- and subradiant Rayleigh scattering into the cavity mode depending on the relative distance between the two atoms. Surprisingly, due to cavity backaction onto the atoms, the cavity output power for superradiant scattering by two atoms is almost equal to the single atom case. We explain these effects quantitatively by a classical model as well as by a quantum mechanical one based on Dicke states. Furthermore, information on the relative phases of the light fields at the atom positions are extracted, and the carrier-free Raman cooling scheme is applied to reduce the jump rate between super- and subradiant configurations.

Parts of this thesis have been published in the following articles:

- R. Reimann, W. Alt, T. Kampschulte, T. Macha, L. Ratschbacher, N. Thau, S. Yoon, D. Meschede, *Cavity-Modified Super- and Subradiant Rayleigh Scattering of Two Atoms*, (2014), arXiv:1408.5874
- R. Reimann, W. Alt, T. Macha, D. Meschede, N. Thau, S. Yoon, L. Ratschbacher, *Carrier-free Raman manipulation of trapped neutral atoms*, (2014), arXiv:1406.2047

Contents

Introduction

It is commonly believed that the usage of tools takes a central role in the evolution of mankind. Starting about 2.3 million years ago with the *Homo habilis* the development towards us, the *Homo sapiens*, was accompanied by the invention of more and more complex and versatile tools. As the *Homo habilis* tried to control his macroscopic environment by using stone tools, we have come a long way to be able to control a world that was invisible to him: the world of single atoms and single photons [1].

Nowadays, we can enter this world via the route of cavity quantum electrodynamics (CQED) where single atoms interact with a single quantized cavity mode [2,3]. Besides the fascinating experimental realization of the for fundamental research important toy model "Single atoms and single photons in a box", the modern perspective is to fully control light-matter interaction at the quantum level, e.g. in applications such as quantum memories [4, 5], single photon sources [6–8] or single photon transistors [9]. Atom-cavity systems and their variants are therefore regarded as promising building blocks for the implementation of quantum information protocols [10] or the creation of quantum networks [11, 12].

Crucial to many of these experiments is the capability to efficiently control the motional degree of freedom of the atoms. In order to localize and prepare neutral atoms with high probability in their motional ground states two different approaches exist. Evaporative cooling of large atomic ensembles has been the established route towards ultracold temperatures in free space [13] and also in cavities [14]. The exact atom number, however, is not controllable in these experiments. .

For a smaller number of atoms various cooling schemes like cavity cooling approaches [15], EIT [16]- or different Raman [17]-sideband cooling schemes have emerged. Here, for the first time these schemes are quantitatively compared to each other in experiments with exactly one single atom coupled to the cavity.

Using a Raman scheme strongly confined neutral atoms can directly be laser cooled into the vibrational ground state of their respective conservative trapping potentials, as has recently been shown with single neutral atoms in optical tweezers [18, 19] and cavities [20, 21].

In contrast to this, I describe the realization of a novel enhanced Raman control scheme for neutral atoms strongly coupled to an optical cavity that features an intrinsic suppression of the two-photon carrier transition, but retains the sidebands which couple to the external degrees of freedom of the trapped atoms. This method is applied to perform Raman cooling to the 2D vibrational ground state and to coherently manipulate the atomic motion.

All cooling experiments mentioned so far are performed with a single atom inside the cavity. We know that a single human being can be described quite well from a biological point of view. As a second human being is added things change. The humans start to interact, and a new theory describing the system dynamics has to be developed: Sociology that is fundamentally different from biology and enables us to understand the interaction of the two humans. The fact that a system can significantly change as new parts are added is generally called emergence and described by a famous paper of Philip W. Anderson titled "More Is Different" [22].

With the step from one to two atoms coupled to a cavity we realize a toy model of emergence in physical systems: One externally driven atom positioned at an antinode of the intra-cavity field does not change its light emission into the cavity mode as it hops from one to the next antinode of the field. The situation drastically changes as a second atom is added to another antinode of the field: Now the two atoms "talk" to each other via the cavity field and – dependent on the relative two-atom distance – constructive or destructive interference between the emitted light fields leads to super- or subradiant Rayleigh scattering into the cavity, respectively.

For large atomic ensembles similar super- and subradiant phenomena [23, 24] as well as cooling and self-organization [15, 25] have been observed in cavities.

With exactly two neutral atoms strongly coupled to a cavity field our experiment realizes the most elementary situation where cooperative radiation and additionally cavity backaction become relevant. The latter explains our observation that the cavity output power for superradiant scattering by two atoms is almost equal to the single-atom case.

We adapt an intuitive classical model form [26] to describe the observed effects and compare this model to a quantum mechanical approach, which – reflecting the system symmetry – clearly shows the connection of our research to Dicke dynamics [27].

Finally we apply the carrier-free Raman cooling method, which we developed with a single atom, to two driven atoms inside the cavity and are thereby able to observe stable relative atom distances for extended periods of time.

1 Experimental Setup

Parts of the experimental setup in our laboratory serve their purpose for more than a decade. Our research began with controlling single cesium atoms [28–31] and evolved to the realization of a cavity quantum electrodynamics (CQED) system [32–35]. Within this chapter I will concentrate on the main working principles of our experimental apparatus, with an emphasis on the technical improvements I was directly involved in during my thesis work.

1.1 Overview

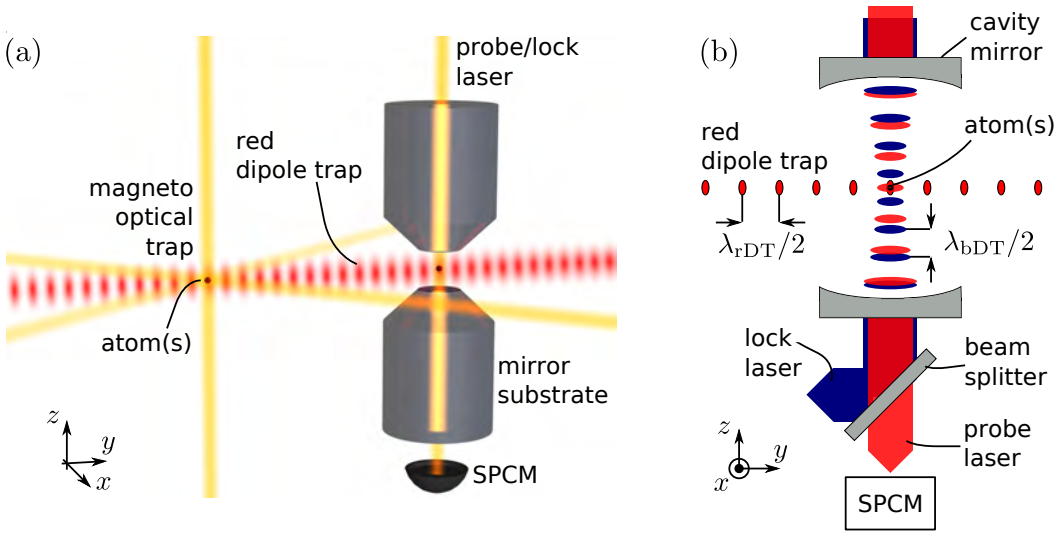

Figure 1.1: Experimental cavity setup (not to scale). (a) 3D drawing (with kind permission of T. Kampschulte [35]) and (b) 2D schematics of the setup. The atoms inside the cavity are trapped in the antinodes of the red detuned dipole trap and in the nodes of the blue detuned dipole trap which is formed by the intra-cavity lock laser. Note that the coordinate system introduced here will be used throughout the thesis.

The heart of the experimental apparatus is shown in Fig. 1.1. It consists of a Fabry-Pérot cavity and gaseous neutral ^{133}Cs atoms, and is situated in an ultra-high vacuum (UHV, pressure $< 10^{-10}$ mbar), which is enclosed by a glass cell [29].

Parameter	Symbol	Value
Mirror spacing	ℓ_0	$158.5\,\mu$m
Cavity mode waist	$w_{0,c}$	$23.15\,\mu$m
Free spectral range	$\omega_{\mathrm{FSR}} = \pi c/\ell_0$	$2\pi \cdot 946\,$GHz
Mirror field transmission	t	$77(6) \cdot 10^{-5}$
Mirror field absorption	a	$141(7) \cdot 10^{-5}$
Mirror field reflectivity	$r = \sqrt{1-t^2-a^2}$	0.9999986(1)
Cavity field decay rate	$\kappa = (1-r^2)c/(2\ell_0)$	$2\pi \cdot 0.40(3)\,$MHz
Cavity line width (intensity)	$\omega_{\mathrm{FWHM}} = 2\kappa$	$2\pi \cdot 0.80(4)\,$MHz
Finesse	$\mathcal{F} = \pi r/(1-r^2)$	$1.2(1) \cdot 10^6$
Birefringent splitting	$\Delta\omega_{\mathrm{br}}$	$2\pi \cdot 3.9\,$MHz
Coupling strength	g_0	$2\pi \cdot 12.7\,$MHz
Atomic dipole decay rate	$\gamma = \Gamma/2$	$2\pi \cdot 2.6\,$MHz
Wavelength D_2-line	λ_0	$852.3\,$nm
Atomic mass	M	$132.9\,$u
Single-atom cooperativity	$C_1 = g_0^2/(2\kappa\gamma)$	78
Detection efficiency (see Eq. 1.36 in [34])	$\eta_{\mathrm{det}} = \eta_{\mathrm{opt}}\eta_{\mathrm{fiber}} \times$ $\times\eta_{\mathrm{VHG}}\eta_{\mathrm{SPCM}}$	0.25(3)
Trap frequencies inside cavity	$2\pi \cdot \{\nu_x, \nu_y, \nu_z\}$	$\approx 2\pi \cdot \{2, 400, 200\}\,$kHz
Red detuned dipole trap waist at the cavity position	w_{rDT}	$35(3)\,\mu$m

Table 1.1: Important system parameters [34–37]. The cavity supports two orthogonal linear polarization modes with frequencies ω_x and ω_y. The polarizations of these modes are parallel to the x- and y-axis (see Fig. 1.1), respectively. The birefringent splitting is defined by $\Delta\omega_{\mathrm{br}} = \omega_y - \omega_x$ [32]. Meaning, if an unpolarized probe beam is coupled into the ω_x-mode, it would populate the ω_y-mode after increasing its frequency by $\Delta\omega_{\mathrm{br}}$. The coupling strength g_0 is calculated for the $|F = 4, m_F = 4\rangle \leftrightarrow |F' = 5, m_{F'} = 5\rangle$ transition and $1/\sqrt{2}(\sigma^+ + \sigma^-)$-polarized light.

In our experiments up to ten atoms are captured from background gas by a high-gradient magneto-optical trap (MOT). The loading of the MOT is repeated until the fluorescence of a desired atom number N is detected [29]. Subsequently these N atoms are transferred into the red standing-wave trap at $\lambda_{\mathrm{rDT}} = 1030\,$nm [33], where an intensified CCD (ICCD) camera (Roper Scientific, PI-MAX:1K) is used to determine their positions by fluorescence imaging [29]. Using the red dipole trap as a conveyor belt (see section 1.2) the atoms are deterministically transported into an orthogonal standing wave, which is formed by the blue detuned locking light ($\lambda_{\mathrm{bDT}} = 845.5\,$nm) of an optical high-finesse Fabry-Pérot cavity [32, 33], see Fig. 1.1(a).

As shown in Fig. 1.1(b) the atoms are trapped along all directions in the intensity

maxima of the red detuned dipole trap. Along the x-direction the atoms are weakly confined by the Gaussian profile of the red dipole trap, whereas tight confinement along the y-direction is guaranteed by the standing wave pattern of the trap. Tight confinement along the z-direction is created by the repulsive force of the intensity maxima of the standing wave, which is formed by the blue intra-cavity lock laser. Typical trap frequencies along all directions are shown in table 1.1.

As sketched in Fig. 1.1(b) the frequencies of the lock and the probe beam are different, leading to a beating between the two standing waves. The distance between positions with equal phase of the two standing waves is called beat length and given with [34]

$$d_{\mathrm{beat}} = \frac{\pi c}{|\omega_{\mathrm{lock}} - \omega_{\mathrm{probe}}|}. \tag{1.1}$$

The longer the beat length, the less significant is the change of the position-dependent atom-cavity coupling g if an atom hops from one to the next lattice site of the lock potential. Lock and probe laser frequencies are both equal to a cavity resonance and therefore multiples of the cavity free spectral range ω_{FSR}. Therefore the beat length in Eq. (1.1) becomes ℓ_0/n where n is the difference between lock and probe frequencies measured in free spectral ranges of the cavity.

To generate light near resonant to the cesium D_2-line transitions we utilize diode lasers. The lasers are used for multiple purposes [33] by splitting the beams and shifting the initially emitted frequencies with acousto-optic modulators (AOMs). All experimentally important diode lasers have been upgraded to stable and reliable interference filter lasers (IFLs, see section 1.3).

As the near-resonant laser light is interacting with the atom-cavity system, photons eventually leak out of the lower cavity mirror. These photons are separated from the lock laser light [34] and detected by a single photon counting module (SPCM, Perkin Elmer SPCM-AQRH-13). The SPCM has a time resolution of 50 ns and a dark count rate of about $0.5\,\mathrm{ms}^{-1}$. Using the values in table 1.1, intra-cavity photons are detected with an overall efficiency of

$$\eta_{\mathrm{oa}} = \frac{t^2}{t^2 + a^2}\eta_{\mathrm{det}} \approx 6\%, \tag{1.2}$$

where the losses due to photon absorption within the lower cavity mirror coating are included.

Given the parameters summarized in table 1.1, the experimental apparatus allows us to enter the regime of strong coupling which is equivalent to a single-atom cooperativity $C_1 \gg 1$. Our coherent atom-cavity energy exchange rate g is significantly bigger than both, the atomic loss channel (γ) and the cavity loss channel (κ). Compared to conventional free space light-matter interaction, the qualitatively new regime of CQED is entered [10]. In this regime the number of atoms $N_0 \approx 1/C_1$ needed to have a significant effect on the intra-cavity field and the number of photons $n_0 \approx (\gamma/g)^2$ that is needed to saturate atoms inside the cavity are both smaller than unity.

Furthermore, our system is close to the perfect cavity limit ($\kappa = 0$) since $\kappa \ll (g_0, \gamma)$, which leads to significant cavity-backaction effects, described in chapter 5.

1.2 An Improved Conveyor Belt Drive

The afore mentioned optical conveyor belt consists of a standing wave formed by two counterpropagating laser beams, each of which has a power of about 2 W and a wavelength λ_{rDT} close to 1030 nm. Details on the working principle of the conveyor belt are described in references [28–30]. In short, atoms, which are trapped in the antinodes of the standing wave, are moved with velocity $v = \lambda_{\mathrm{rDT}}\Delta\nu/2$ along the conveyor belt axis, where $\Delta\nu$ is the frequency detuning between the two counterpropagating laser beams. Typical velocities of 5 m/s are reached on the millisecond scale, corresponding to accelerations on the order of $10^4\,\mathrm{m/s^2}$. In our experiment the atoms are transported with sub-micrometer precision from the MOT position over a distance of about 4 mm into the center of the cavity mode.

Technically the transport is implemented by changing the frequencies of each of the two counterpropagating laser beams with a radio frequency driven acousto-optic modulator (AOM) in the double-pass configuration. Two main requirements have to be fulfilled: First, in order to achieve sub-micrometer precision, these radio frequencies and their relative phase have to be well controlled on a microsecond timescale. Second, the relative phase noise between the two applied frequencies needs to be minimal to avoid resonant heating the atoms by shaking the standing-wave lattice [38].

1.2.1 Characterization

The above mentioned requirements can be met by using a dual digital frequency synthesizer (DDFS) as drive.

Compared to our former conveyor belt drive (APE Berlin, model DFD 100) the current DDFS is a state-of-the-art device which is more versatile (arbitrary frequency ramps can be programmed) and has a lower phase noise.

DDFS Hardware

The dual digital frequency synthesizer (DDFS) evaluation board from Analog Devices is composed of two AD9954 direct digital synthesizer (DDS) chips. We use a mbed microcontroller (ARM mbed NXP LPCL768) to communicate with the DDFS.

The evaluation board has two frequency output channels with a frequency range from DC to 160 MHz, each. Two individual DDS chips (DDS1: Ch1 and DDS2: Ch2) enable the user to change the frequencies of these two output channels in an independent but phase-coherent way. Both chips have an identical hardware configuration. Fig. 1.2 shows the circuit layout for one DDS chip. The DDS chip

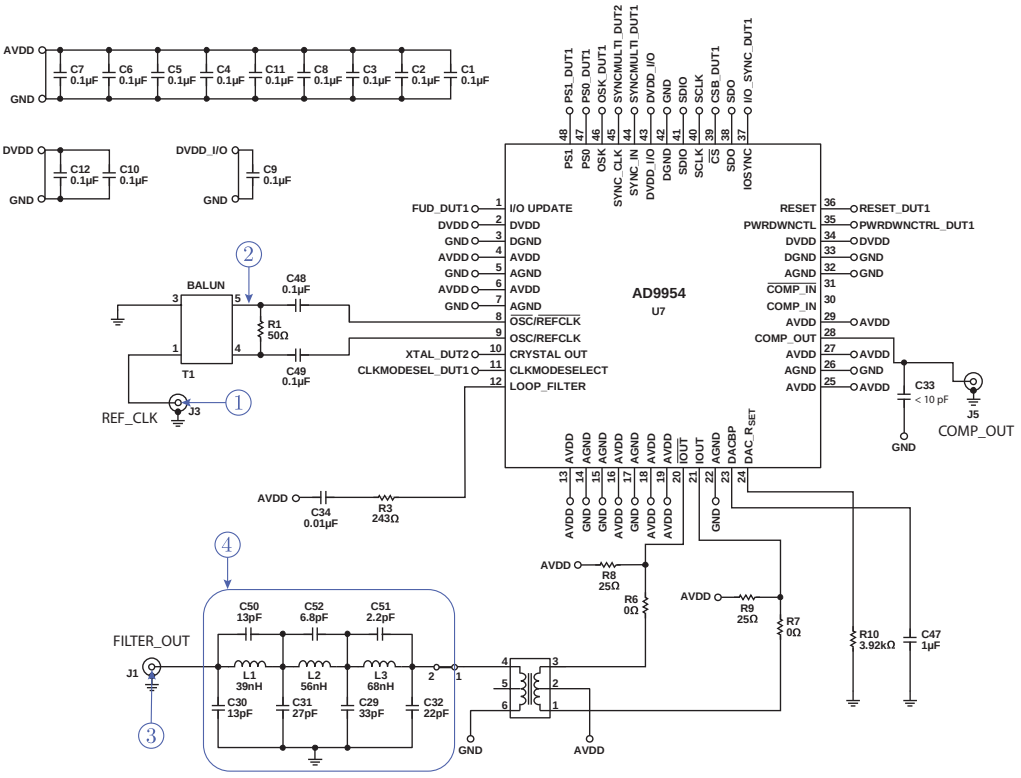

Figure 1.2: Hardware layout of the AD9954, adapted from [39]. The meaning of the encircled numbers is given in the text.

requires an external reference clock running at a maximal and optimal frequency of 400 MHz, which is applied at Pos. 1 in Fig 1.2. A maximum and optimal peak-to-peak voltage of 0.5 V should be set at Pos. 2 [39], which corresponds to a power of 4 dBm at Pos. 1. The output power of the DDS within a range from 0 W to −5 dBm is delivered at Pos. 3. Pos. 4 marks a higher order low-pass filter with its −3 dBm cutoff frequency at 175 MHz. Up to 165 MHz the filter is completely flat.

Phase Noise Measurement

In order to quantify the experimentally relevant phase noise of the DDFS, the device is operated at the optimal reference-clock conditions and all external noise sources, which could be detrimental to the measurement, are eliminated. Measuring the DDFS output signals at Ch1 and Ch2 one faces the fact that – even though both channels are set to the exact same frequency and phase, – the signals are slightly different. This noise is arising from the digitalization and sampling of frequencies and is called phase noise.

To quantify this relative phase noise between Ch1 and Ch2 it is common practice [40] to mix the two channels as depicted in Fig. 1.3. Using a sensitive mixer – phase detector – is advantageous. To match the specifications of the phase de-

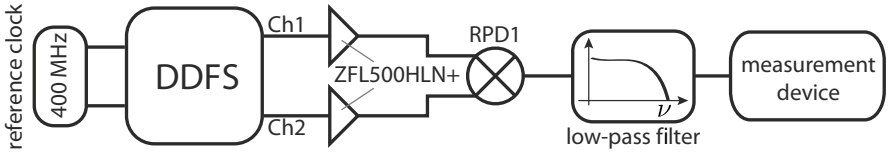

Figure 1.3: Setup for detecting the phase-noise signal. DDS1 and DDS2 give out high frequency signals ($\approx 100\,\mathrm{MHz}$) at Ch1 and Ch2, respectively. The pre-amplifiers ZFL500HLN+ (Mini-Circuits) amplify the signals to 7 dBm at the RPD1 phase-detector (Mini-Circuits) inputs. After the phase detector the signal is filtered by a low-pass filter (3 dB cutoff frequency at 10 MHz) and measured.

tector, the input impedance of the low-pass filter in the setup is designed to be $500\,\Omega$. Further the output powers of Ch1 and Ch2 are set to $-12\,\mathrm{dBm}$ by using on-chip amplitude scaling [39]. The filtered signal is recorded with a digital oscilloscope (Agilent DSO-X 2004A, $1\,\mathrm{M}\Omega$ input resistance, bandwidth = 20 MHz) or a spectrum analyzer (HP 3589A, $1\,\mathrm{M}\Omega$ input resistance).

To calibrate the required parameters for a phase noise measurement, the channels Ch1 and Ch2 are operated at different but constant frequencies. The resulting signal oscillates with a frequency[1] $\Delta\nu$ is measured with the oscilloscope and described by

$$V[t] = V_0 \cdot \sin[2\pi\Delta\nu \cdot t + \Delta\varphi]. \tag{1.3}$$

The value $V_0 = 879(2)\,\mathrm{mV}$ depends on the mixer and becomes important for normalization.

After the measurement of V_0 the frequency difference between the channels $\Delta\nu$ is set to 0. Now the signal at the measurement device is placed close to a zero-crossing, by adjusting the relative phase $\Delta\varphi$ between the Ch1 and Ch2 signals (e.g. by changing the cable lengths before the mixer). Here and for small noise signals ($V_{\mathrm{rms}} \ll V_0$) Eq. (1.3) behaves linear and the phase noise (units: rad) is proportional to the measured noise signal:

$$\Delta\phi_{\mathrm{rms}} = V_{\mathrm{rms}}/V_0. \tag{1.4}$$

The standard deviation of V_{rms} can be measured with the oscilloscope, or for spectral resolution, with the spectrum analyzer, as described below.

Quantitative noise measurement

For a quantitative phase noise characterization the spectrum analyzer is used with the setup shown in Fig. 1.3 to measure the root-mean-square noise voltage $V_{\mathrm{rms}}^{(\mathrm{m})}$ (units: $V/\sqrt{\mathrm{Hz}}$).

[1] Typical used values are $\nu(\mathrm{Ch1}) = 100\,\mathrm{MHz}$, $\nu(\mathrm{Ch2}) = 99\,\mathrm{MHz}$, $\Delta\nu = 1\,\mathrm{MHz}$.

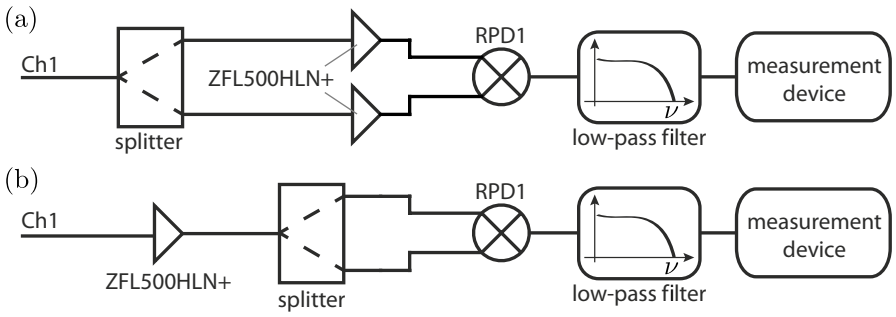

Figure 1.4: Setups for reference measurements. (a) Reference setup to normalize the measurements done with the spectrum analyzer in the configuration of Fig. 1.3). (b) Setup used to quantify the influence of the amplifier ZFL500HLN+.

To correct for the noise that couples in via ground loops or due to other imperfections of the setup (mixer, amplifiers), reference measurements are needed. Fig. 1.4(a) shows the setup used to quantify the influence of the mixer and the amplifiers. Fig. 1.4(b) sketches how to check the sole influence of the amplifier. Compared to Fig. 1.4(a) there was no measurable difference. The influence of the amplifiers is therefore negligible and both setups can be used for the reference measurement ($V_{\mathrm{rms}}^{(\mathrm{r})}$).

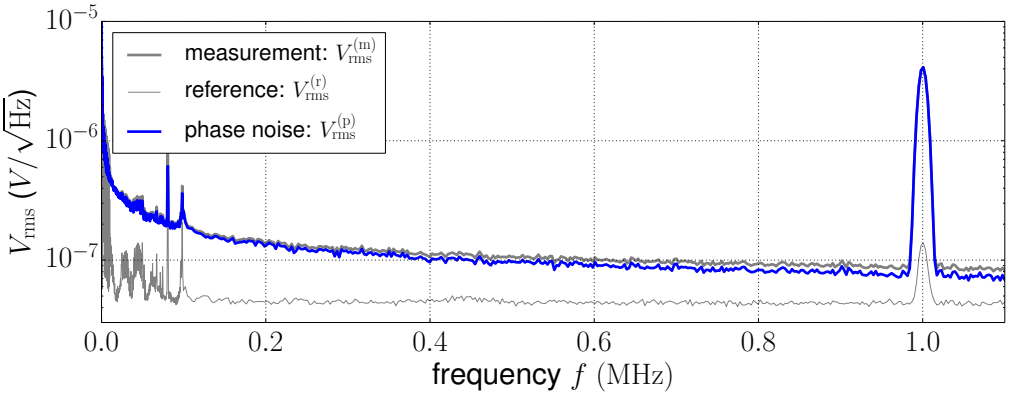

Figure 1.5: Noise measurement with the spectrum analyzer (details see text). The well pronounced peak at 1 MHz is an artifact from the DDS frequency-generation process. Here the output frequency of Ch1 and Ch2 were set to 99 MHz. Depending on this frequency different spurious peaks at different positions appear in the spectrum.

Figure 1.5 shows the recorded noise data: The phase noise is given by

$$V_{\mathrm{rms}}^{(\mathrm{p})} = \sqrt{\left(V_{\mathrm{rms}}^{(\mathrm{m})}\right)^2 - \left(V_{\mathrm{rms}}^{(\mathrm{r})}\right)^2}. \tag{1.5}$$

Eq. (1.5) originates from the fact that powers have to be added linearly due to energy conservation.

A comparison between our measurements and graphs shown in the AD9954 data sheet shows that our hardware is well within the claimed specifications.

1.2.2 Heating and Atom Lifetime

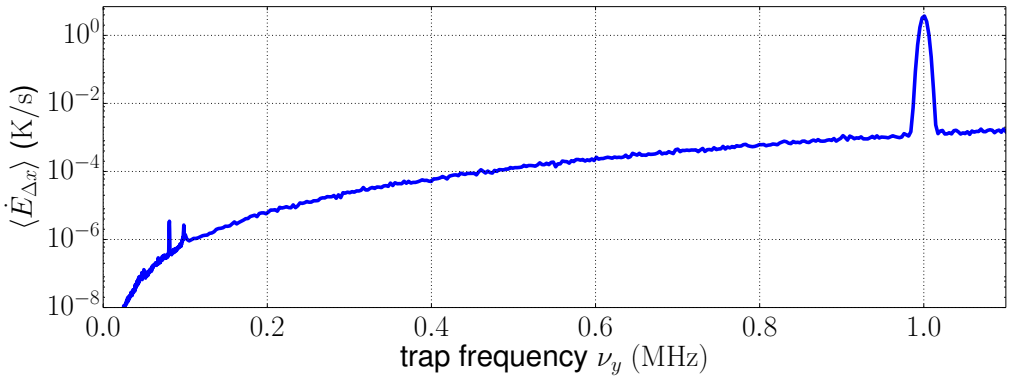

Figure 1.6: Calculated mean heating rate as function of axial trap frequency ν_y for Ch1 and Ch2 at 99 MHz.

The data in Fig. 1.5 allows one to calculate the expected heating rate of atoms that are trapped within the previously introduced conveyor belt with wavelength $\lambda_{\mathrm{rDT}} = 1030\,\mathrm{nm}$.

Phase noise in the frequency band $[\nu_1, \nu_2]$ is calculated with Eq. (1.5) and Eq. (1.4) and reads

$$\Delta\phi_{\mathrm{rms}} = \frac{\sqrt{\int_{\nu_1}^{\nu_2} \left(V_{\mathrm{rms}}^{(\mathrm{p})}[\nu]\right)^2 \mathrm{d}\nu}}{V_0}. \tag{1.6}$$

This relative phase noise is transferred to the atoms inside the dipole trap via the AOMs and leads to an axial shaking of the dipole trap with a mean-square amplitude of [29]

$$\langle (\Delta x)^2 \rangle = \left(\frac{\Delta\phi_{\mathrm{rms}}}{2\pi/\lambda_{\mathrm{rDT}}} \right)^2 = \int_{\nu_1}^{\nu_2} S_{\Delta x}[\nu] \mathrm{d}\nu. \tag{1.7}$$

The power spectrum of position fluctuations $S_{\Delta x}[\nu]$ is directly connected to the heating rate the atoms experience inside the trap [38]. Combining Eqs. (1.6) and (1.7) one finds

$$S_{\Delta x}[\nu] = \left(\frac{V_{\mathrm{rms}}^{(\mathrm{p})}[\nu]}{V_0 \cdot 2\pi/\lambda_{\mathrm{rDT}}} \right)^2. \tag{1.8}$$

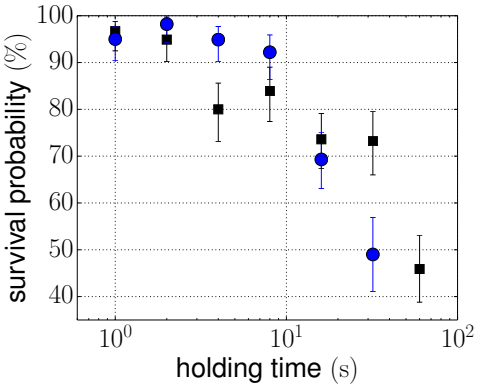

Figure 1.7: Atom survival probability as a function of the holding time (logarithmic plot) in the conveyor belt at the MOT position. The conveyor belt AOMs are driven by Ch1 and Ch2 of the DDFS (blue circles) and, for comparison, with a common source. Error bars are statistical.

In the harmonic trap limit the mean heating rate for small excitations is given by [38]

$$\langle \dot{E}_{\Delta x}[\nu_0] \rangle = 4\pi^4 m \cdot \nu_0^4 S_{\Delta x}[\nu_0]/k_{\mathrm{B}}, \tag{1.9}$$

with M being the mass of a cesium atom (see table 1.1), ν_y the axial trap frequency, and k_{B} the Boltzmann constant. Based on the measured phase noise, the calculated heating rate as a function of the axial trap frequency is shown in Fig. 1.6.

Our axial trap frequency at the MOT position is $\nu_z^{(\mathrm{MOT})} \approx 300\,\mathrm{kHz}$. With a trap depth of about 1 mK the atomic survival time is estimated to be on the ten second scale.

To benchmark the DDFS drive, an atom-survival measurement at the MOT position is performed, see Fig. 1.7. After a certain holding time inside the static conveyor belt trap, the fraction of atoms still being trapped is measured. For comparison the first data set is recorded with the DDFS driving the conveyor belt AOMs (blue circles) while a second set is recorded with a common drive (black squares). In the later case no relative phase noise is present and the lifetime (half-life) of about 60 s is limited by collisions with the background gas. In the first case the lifetime of about 30 s is limited due to the resonant phase-noise heating. This result is in good agreement with the estimation above, based on Fig. 1.6 and is an improvement of one order of magnitude compared to the old conveyor belt drive [29].

1.3 A Stable Laser Source: The Interference Filter Laser

Diode lasers are the workhorses of quantum optic experiments. In our laboratory four diode lasers are operated simultaneously. These lasers have to meet two main requirements. First, it is required to lock the laser on a sub-MHz scale. Second, and most important for the daily work, the reliability and stability of the system is crucial. To improve the uptime of the experiment we upgraded our experiment from Littrow lasers to interference-filter-stabilized diode lasers (IFL). A Littrow laser stabilizes the frequency of the laser by optical feedback from an angle-sensitive

grating [41], while the frequency selection of the IFL is accomplished by a narrow-band ($\lesssim 1\,\mathrm{nm}$) interference filter and a rather angle-insensitive outcoupling mirror. Fig. 1.8(a) shows the design of our IFLs[2], which is based on the original design of Peter Rosenbusch's group [42]. The light, emitted by the laser diode, is collimated by lens 1, passes the interference filter and is focused onto the outcoupling mirror by lens 2. This cat's-eye configuration, and the fact that all optical components are mounted on a solid aluminum block, ensure a good long term mechanical stability of the laser resonator and a high insensitivity against acoustical noise. Lens 3 collimates the output laser beam. The rather long resonator (about 12 cm between laser diode and outcoupling mirror) leads to a measured linewidth on the ten kHz scale.

Another important characteristic of the IFL is its response to frequency modulation, applied to the laser diodes driving current. Practically, feeding an additional

[2]Our IFL design has mainly been developed and optimized by Andrea Alberti, Wolfgang Alt, Dietmar Haubrich and Carsten Robens.

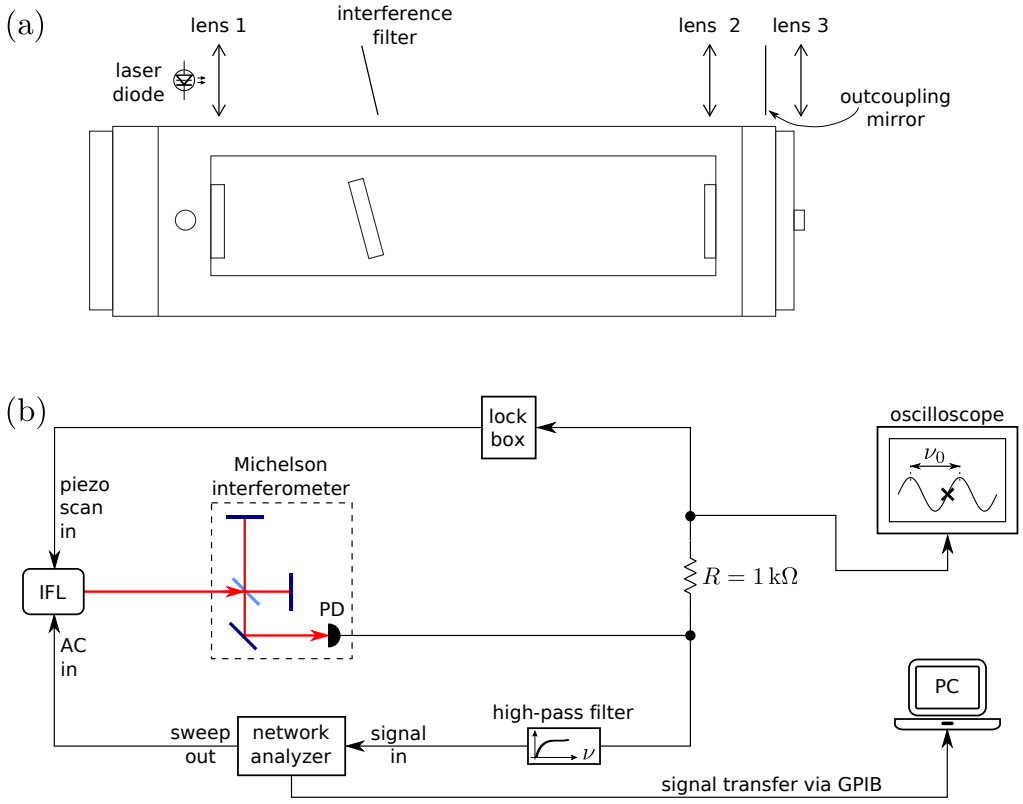

Figure 1.8: (a) To scale top view of the interference filter laser (IFL) with the outcoupling mirror mounted on a piezoelectric tube (not shown). The drawing is adapted from an image by Ricardo Gómez. (b) Simplified setup for measuring the IFL frequency-modulation transfer function. The two arms of the Michelson interferometer are adjusted to be power balanced.

alternating current into the DC powered laser diode is used for fast frequency stabilization ("current locking") and for modulating sidebands onto the lasers output (see section 1.4).

Fig. 1.8(b) illustrates the setup for measuring the frequency-modulation transfer function of the IFL that is powered with a constant current of $I_0 \approx 100\,\mathrm{mA}$ and operated at about 852 nm. The laser diode current is modulated by the frequency sweep of a network analyzer (HP 3589A). A constant power of $-50\,\mathrm{dBm}$ is applied, corresponding to a root-mean-square current of $I_{\mathrm{mod}} = 14\,\mu\mathrm{A}$ at the laser diode. This small modulation amplitude of the frequency sweep assures that the frequency of the laser light is modulated while the optical output power stays constant to good approximation.

The laser light is sent through a Michelson interferometer with a fixed arm length difference $\Delta L = 26.0(2)\,\mathrm{cm}$. The Michelson interferometer converts the frequency modulation of the light to a power modulation that is detected by a fast photodiode (Thorlabs PDA10A-EC, bandwidth = 150 MHz). The photo diode signal is split in two parts. In order to block direct currents, one part is high pass filtered (3.2 kHz cutoff frequency) and measured with the network analyzer. The network analyzer averages over ten full sweeps and transfers the measured spectra via a GPIB-interface to a computer. The second part is measured with an oscilloscope and fed into a self-built lock box. To avoid open-end reflections from the cables ending at the oscilloscope ($1\,\mathrm{M}\Omega$ input impedance) and the lock box ($100\,\mathrm{k}\Omega$ input impedance) a $1\,\mathrm{k}\Omega$ resistor is added.

The output signal of the lock box is used to either scan or stabilize (lock) the IFL output frequency. The lock is realized via a slow feedback (bandwidth $\lesssim 100\,\mathrm{Hz}$) to the piezoelectric tube, which is controlling the IFL outcoupling mirror position. Such the fast frequency modulation of the laser is not affected by the lock.

For measuring the voltage-to-frequency conversion of the interferometer, the sweep out of the network analyzer is switched off and the lock box is used in the scanning mode with a scanning frequency of about 100 Hz. At this scanning frequency the photodiode output is connected to an impedance much bigger than $50\,\Omega$ and recorded with the oscilloscope. The recorded signal is fit with $V[t] = \mathrm{off} + V_0 \sin[2\pi\nu/\nu_0 + \phi]$, where ν is the laser frequency and the offset off and the phase ϕ are constants. The Michelson interferometer fringe distance in frequency space is given by $\nu_0 = c/(2\Delta L) = 577(4)\,\mathrm{MHz}$. Knowing the voltage amplitude $V_0 = 3.65(5)\,\mathrm{V}$ from the fit, one calculates the root-mean-square voltage-to-frequency conversion with

$$\nu_{\mathrm{mod}}[V_{\mathrm{rms}}] = \frac{\nu_0}{2\pi V_0} V_{\mathrm{rms}}. \tag{1.10}$$

This relation holds for side-of-fringe measurements where the frequency sensitivity is maximal and $\sin[2\pi\nu/\nu_0 + \phi] \approx 2\pi\nu/\nu_0$.

We proceed with measuring the IFL's current-frequency response function by weakly locking the system to the side of a fringe (see cross on oscilloscope screen in Fig. 1.8(b)). In this measurement we use the network analyzer to sweep the

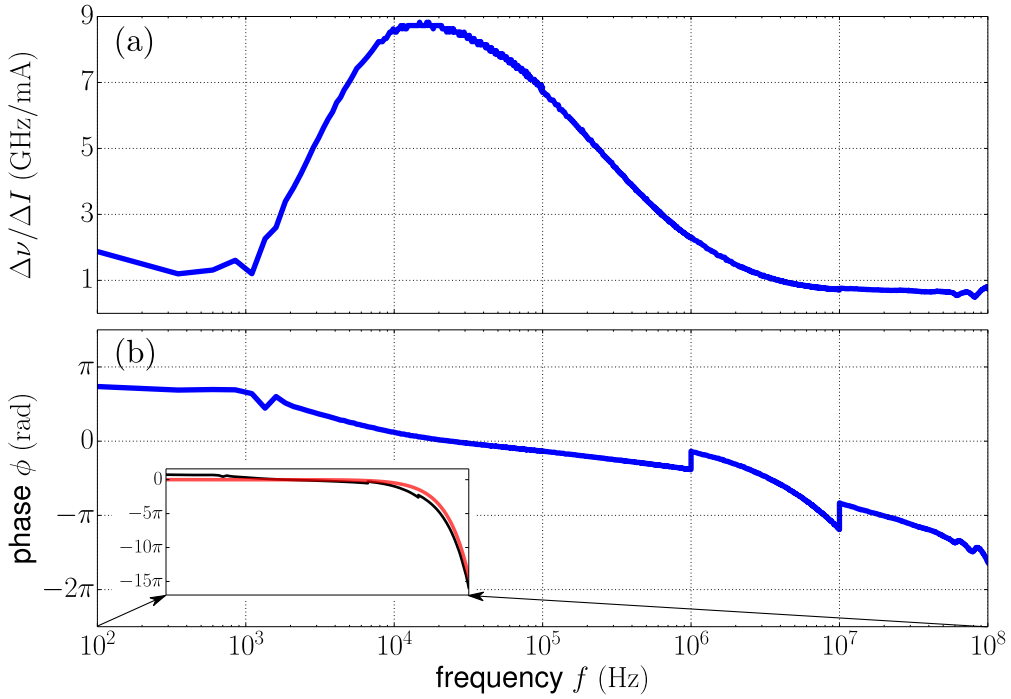

Figure 1.9: Measured frequency-modulation transfer function of a IFL. (a) shows the laser's frequency amplitude response to current modulation, as the output frequency f of the network analyzer is swept. (b) shows the phase answer (blue) of the laser diode, which is calculated from the inset. The original data (black) is shown in the inset, after a standard phase unwrapping algorithm has been applied to it. The red line shows the expected influence of additional path lengths (see text).

frequency of the modulation current and to record power (P_{dBm}) and phase spectra. Concerning the power spectra and their voltage-to-frequency conversion one has to note that the photodiode output is now matched by the $R_0 = 50\,\Omega$ input impedance of the network analyzer for all relevant frequencies. This reduces the output voltage of the photodiode by a factor of two which enters Eq. (1.10) by $V_0 \to V_0/2$. With the conversion of P_{dBm} to V_{rms} and with Eq. (1.10) we write the frequency-current dependence of the laser diode as

$$\frac{\Delta\nu}{\Delta I} = \frac{\nu_{\mathrm{mod}}}{I_{\mathrm{mod}}} = \frac{\nu_0}{\pi V_0 I_{\mathrm{mod}}} \sqrt{R_0 P_0 10^{P_{\mathrm{dBm}}/10}}, \tag{1.11}$$

where $P_0 = 1\,\mathrm{mW}$. Fig. 1.9(a) shows the frequency change of the laser for a certain modulation current, as the frequency f of this modulation is varied. For lower frequencies an AC coupling capacitor inside the IFL casing acts as high-pass filter. For higher modulation frequencies $f \gtrsim 10\,\mathrm{MHz}$ the laser diode cannot follow the fast modulation current, due to an interplay between counteracting fast

current and slower current induced temperature effects inside the laser diode [43]. The maximum measured current modulation capability of about 9 GHz/mA around 20 kHz is an order of magnitude larger than recorded values of comparable IFLs under DC variation. This – for unclear reasons – is in contrast to the expectation that these values should be comparable.

Fig. 1.9(b) shows the phase answer of the laser diode. The inset shows the measured data, after unwrapping the phase, in black. To account for additional path lengths L of coaxial cables and optical fibres their phase delay (red curve) is calculated. For our setup L is estimated to be 15 m and a group velocity of 0.7 times the speed of light is assumed inside cables and fibers. Subtracting the red line from the black data leads to a good estimate of the IFL phase response, shown in blue. As $\Delta\nu/\Delta I$ in (a) has its flat maximum, neither the described high-pass filter for coupling the current to the diode, nor the low-pass like behavior of the diode itself contribute, which leads to a phase $\phi = 0$ in this region. At $\phi = 0$ the laser diode is modulated most efficiently. Therefore this point is taken as reference for finding the maximum bandwidth for a current feedback applied to the laser.

At the maximum current feedback bandwidth of about 8 MHz the phase has changed to $-\pi$. At this frequency also $\Delta\nu/\Delta I$ has asympotically reached a value of less than 1 GHz/mA. The maximum bandwidth of a system shrinks with additional path lengths such as cables, fibers or free space beam distances, inducing a delay of the signal. Especially for fast feedback with a high bandwidth the path lengths should be kept as short as possible. An example for such a fast feedback system is the optical phase lock loop described in section 4.1.

The results from this section can be used for estimating the performance of an IFL in a negative feedback loop that acts back on the laser via the current. The specific laser, which frequency-modulation transfer function has been described within this section, is now used as lock laser (see following section). All IFLs in our laboratory show stable long term operation: no relocking of the lasers over several days is necessary.

1.4 An Optimized High-Finesse Cavity Lock

The technically most advanced piece of our experimental apparatus is the frequency stabilization (lock) of the high-finesse cavity. Given the cavity parameters shown in table 1.1, one finds that the needed frequency stabilization of $\sim \kappa/10$ is equivalent to a length stabilization on the order of $\Delta\ell_0 \sim 10$ fm [35]. The cavity length $\ell_0 \approx 160\,\mu$m is stabilized with a feedback loop acting on shear-piezoelectric transducers, glued to the cavity mirror substrates [32]. We use the Pound-Drever-Hall (PDH) method [44, 45] to lock the cavity to a frequency-stabilized laser (lock laser). Our specific implementation is described in references [29, 32]. The details of the lock have continuously been improved, with the last major modification – a cross-lock of the lock laser back onto the cavity – explained in [35].

The PDH method requires the light of the lock laser to be phase modulated with

a frequency $\omega_{\mathrm{LO}} \gg \kappa$. The phase-modulated light is partially reflected back from the cavity, detected and processed with analog electronics, whereby an error signal with a steep slope is produced; for details see [29].

We used to imprint the phase modulation (PM) directly onto a laser in Littrow configuration [41] by modulating the laser diode current. However, to achieve better long-term stability the laser was exchanged by an IFL, introduced in section 1.3. The IFL current has to be modulated more strongly at $\omega_{\mathrm{LO}} \approx 2\pi \cdot 40\,\mathrm{MHz}$ than the Littrow laser for a comparable signal-to-noise ratio of the PDH error signal. This can be explained by the higher intrinsic frequency stability of the IFL: The optical feedback via the long IFL resonator leads to a narrow and stable linewidth. It therefore tends to counteract the current modulation induced change in frequency. This is indicated by the measurement shown in Fig.1.9.

1.4.1 Influence of Parasitic Amplitude Modulation

The required strong IFL current modulation leads to an additional amplitude modulation (AM), which distorts the PDH error signal and produces an offset of the signal. The offset is detrimental because it varies with the laser power coupled into the cavity, which again depends on the power and pointing stability of the lock laser beam in front of the cavity, introducing unnecessary instability.

We describe the effect of parasitic AM on the PDH error signal in a model and start with pure phase modulation (for a good introduction on PM see [46]) of the electric field:

$$\begin{aligned} E_{\mathrm{PM}} &= E_0 \cos[\omega_{\mathrm{c}} t + p \sin[\omega_{\mathrm{LO}} t + \varphi_p]] = \\ &= E_0 \sum_{n=-\infty}^{\infty} J_n[p] \cos[(\omega_{\mathrm{c}} + n\omega_{\mathrm{LO}})t + n\varphi_p], \end{aligned} \tag{1.12}$$

where E_0 is the field amplitude, ω_{c} is the carrier frequency (unmodulated optical frequency of the lock laser) and φ_p is the phase of the PM. The dimensionless amplitude p is called PM index and determines the strength of the modulation. Eq. (1.12) is rewritten using the Jacobi-Anger expansion, which introduces the n^{th} order Bessel functions of the first kind J_n. In our case the strength of the PM is moderate ($p \lesssim 1$) and the summation is truncated at $n = -3$ and 3, since no higher-order sidebands are generated.

In contrast to pure PM, pure AM only generates first-order sidebands for any AM index a and is described by

$$\begin{aligned} E_{\mathrm{AM}} &= E_0(1 + a \sin[\omega_{\mathrm{LO}} t + \varphi_a]) \cos[\omega_{\mathrm{c}} t] = \\ &= E_0 \left(\cos[\omega_{\mathrm{c}} t] + \frac{a}{2} (\sin[(\omega_{\mathrm{c}} + \omega_{\mathrm{LO}})t + \varphi_a] - \sin[(\omega_{\mathrm{c}} - \omega_{\mathrm{LO}})t - \varphi_a]) \right), \end{aligned} \tag{1.13}$$

where standard trigonometric relations are used to show the second equal sign.

Using Eqs. (1.12) and (1.13), PM and AM present at the same time is written

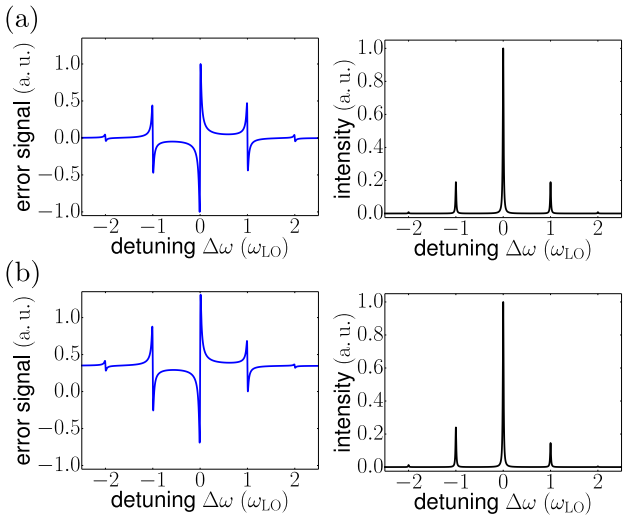

Figure 1.10: Calculated PDH error signals (blue) and corresponding cavity transmissions (black) as functions of the detuning of the carrier frequency ω_c from a cavity resonance. (a) Pure PM with $p = 0.8$, $a = 0$. (b) Additional AM with $a = 0.1$, $\varphi_a = \varphi_p + 0.46\pi$. The settings in (b) are chosen to produce the features, which were observed as the IFL current was modulated with ω_{LO}.

down as

$$E_{\mathrm{PM,AM}} = E_0(1 + a\sin[\omega_{\mathrm{LO}}t + \varphi_a]) \sum_{n=-3}^{3} J_n[p]\cos[(\omega_c + n\omega_{\mathrm{LO}})t + n\varphi_p]. \qquad (1.14)$$

Applying the same trigonometric relations as above, one finds that additional AM adds out-of-phase components to all bands n of the PM. An intuitive understanding of parasitic AM effects on the cavity lock is therefore not easily developed.

Therefore we choose Eq. (1.14) as the input field for the cavity response functions and calculate – as described in detail in [47] – the expected PDH error signal and the transmitted lock laser intensity after the cavity. Fig. 1.10 illustrates these calculations with (a) no AM, and (b) for a moderate AM ($a = \frac{1}{8}p$). The parameters in (b) are chosen to match the observed phenomena for the current modulated IFL: a distortion as well as a DC offset of the PDH error signal and an asymmetry in the signal transmitted through the cavity.

1.4.2 The Final Cavity-Lock Setup

The described parasitic AM of the IFL reduces the stability advantages of the laser, when using it for locking the cavity. The problem is solved by phase modulating the lock laser light with a self-built resonant electro-optic modulator (EOM). The resonant circuit is composed of a small air-core coil and the electro-optic crystal as capacitor. By changing the inductance of the coil the resonance frequency of the circuit is adjusted. Another small coil is used to inductively couple a few Watts of radio-frequency (RF) power at ω_{LO} into the resonant circuit. With this technique nearly pure PM with a modulation index $p \lesssim 1$ is realized, leading to signals similar to those in Fig. 1.10(a).

Furthermore, a constant trap depth and trap frequency ν_z need to be guaranteed for the Raman sideband measurements in chapter 4 where motional sideband transitions along the z-axis are investigated. We meet this requirement by stabilizing

the intra-cavity lock laser power with an additional slow negative feedback loop. The loop with a bandwidth below 1 kHz is based on a self-built lock box. The lock box feeds back the lock laser power after the locked cavity onto the RF power driving an AOM that controls the optical lock laser power before the cavity.

In conclusion, the usage of the IFL leads to better long- and short-term stability of the cavity lock. Together with the actively stabilized intra-cavity lock laser power the machine is capable of efficiently performing Raman sideband measurements: Gaining data with a high signal-to-noise ratio under stable conditions is now possible.

1.5 Motional Harmonic Oscillator Quantities

For the Raman sideband measurements in chapter 4 and also for the cooperative coupling of two atoms to the cavity in chapter 5 it is essential that the atoms are trapped and cooled in standing wave potentials. These potentials are described by a sinus or a Gaussian for the axial or radial direction, respectively. Here characteristic motional quantities like the spatial extension of the trapped particles, the mean motional state number $\overline{m}$ or the mean energy $\overline{E}$, which are of use throughout this thesis, are calculated and summarized.

If the atoms are cooled close to the bottom of the trap, a harmonic approximation of the potential is possible. Quantum mechanically, the spatial Eigenfunctions $\psi_m[x]$ of a particle in a harmonic potential $U[x] = 1/2 \cdot M(2\pi \cdot \nu)^2 x^2$ can be written in terms of the Hermite polynomials $H_m[\xi]$ as

$$\psi_m[x] = \frac{1}{\sqrt{2^m\, m!\, \Delta x_0 \cdot \sqrt{2\pi}}} \exp\left[-\frac{x^2}{4\Delta x_0^2}\right] \cdot H_m\left[\frac{x}{\sqrt{2}\,\Delta x_0}\right], \tag{1.15}$$

with n being the atomic vibrational quantum number, M being the mass of the trapped particle and ν being the trap frequency [48].

$$\Delta x_0[\nu] = \sqrt{\hbar/(2M \cdot 2\pi \cdot \nu)} \tag{1.16}$$

is the natural length scale of the harmonic oscillator. For the limiting case $T = 0$ the atom is in its motional ground state ($n = 0$), which has a Gaussian probability distribution $|\psi_0[x]|^2$ with a 1σ half width of Δx_0. The probability density of a Gaussian distributed variable x is

$$\rho_\sigma[x] = \frac{1}{\sigma\sqrt{2\pi}} \cdot \exp\left[-\frac{1}{2}\frac{x^2}{\sigma^2}\right], \tag{1.17}$$

where the probability of being within the spatial dimensions of σ is given by $\int_{-\sigma}^{\sigma} \rho_\sigma[x]\,\mathrm{d}x \approx 68\%$.

A particle's probability density is calculated by a Boltzmann-weighted sum over the wave function probabilities $1/Z \cdot \sum_{m=0}^{\infty} \exp[-mh\nu/(k_\mathrm{B}T)] \cdot |\psi_m[x]|^2$ with Z as a

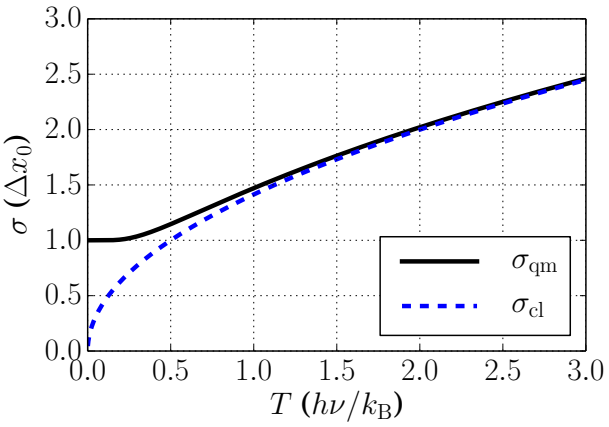

Figure 1.11: Gaussian 1σ half width of a harmonically trapped particle as a function of the temperature. Temperature and half width are plotted in their natural units. The classical half width is a very good approximation to the quantum mechanical solution for $k_\mathrm{B}T > h\nu$ (T in natural units > 1).

normalization constant. This infinite sum can be evaluated by using operator relations of the annihilation and creation operators of the quantum harmonic oscillator (see [49]). The result is a Gaussian probability density given by Eq. (1.17) with

$$\sigma_\mathrm{qm} = \sqrt{\frac{\hbar}{2M2\pi\cdot\nu}\coth\left[\frac{h\nu}{2k_\mathrm{B}T}\right]} = \Delta x_0\cdot\sqrt{\coth\left[\frac{h\nu}{2k_\mathrm{B}T}\right]}\,. \tag{1.18}$$

For the limiting case of high temperatures ($k_\mathrm{B}T \gg h\nu$) the problem can be solved classically yielding a Boltzmann probability density $\propto \exp[-U[x]/(k_\mathrm{B}T)]$ [29, 49]. Normalization leads to the probability density that is Gaussian again and is described by Eq. (1.17) with

$$\sigma_\mathrm{cl} = \sqrt{\frac{k_\mathrm{B}T}{M(2\pi\cdot\nu)^2}}\,. \tag{1.19}$$

Fig. 1.11 shows the width of the wave packet as a function of the temperature. For $T \to 0$ the classical width – not knowing about the uncertainty principle – underestimates the real width.

Practically we start all experiments described here with atoms in a dipole trap molasses-cooled to about $30\,\mu$K [35]. Our trap frequencies in table 1.1 lead to $k_\mathrm{B}T \gg h\nu$. Therefore the classical approximation can be used.

Within the Raman cooling experiments described in chapter 4 ground state cooling is achieved. Here the quantum mechanical description should be applied. Further, the mean motional state number $\overline{m}$ and the mean vibrational energy $\overline{E}$ become important. Using again Boltzmann-weighted sums one finds their connection to temperature [49]:

$$\begin{aligned}\overline{m} &= \frac{1}{\exp\left[\frac{h\nu}{k_\mathrm{B}T}\right]-1} \xrightarrow{k_\mathrm{B}T\gg h\nu} \frac{k_\mathrm{B}T}{h\nu}\\ \overline{E} &= (\overline{m}+1/2)\cdot h\nu \xrightarrow{k_\mathrm{B}T\gg h\nu} k_\mathrm{B}T\,.\end{aligned} \tag{1.20}$$

For high temperatures these quantities converge to the classical cases, as expected. For very cold temperatures the probability p_0 of being in the motional ground state is often chosen as a figure of merit [20, 21, 50]. In thermal equilibrium it is given with

$$p_0 = 1 - \exp\left[-\frac{h\nu}{k_\mathrm{B}T}\right] \overset{\text{Eq. (1.20)}}{=} \frac{1}{1+\overline{m}} \overset{p_0 \approx 1}{\longrightarrow} 1 - \overline{m}. \tag{1.21}$$

2 The Art of Cooling Inside an Optical Cavity

The control over internal and external degrees of freedom is the key to many modern experiments in quantum optics. The internal states of neutral atoms and ions are manipulated by standard techniques as optical pumping for state initialization [51] and microwave radiation or Raman beams for coherent state transfer [1]. Cooling to the 3D motional ground state is achieved in ion experiments by various techniques [52]. Ground-state cooling of trapped ions and of neutral atoms in optical potentials has been shown two decades ago [50,53]. However, neutral atom systems strongly coupled to an optical cavity have only very recently been cooled to the 3D motional ground state [21]. The main difficulty in cooling atom-cavity systems lies in the fact that the cavity blocks most of the solid angle around the atoms. This leads to very limited optical access. Therefore the experimental implementation of cooling schemes can be a challenging task.

In this chapter I will focus on theoretical results of different cooling approaches for atoms coupled to an optical cavity that have been realized within this thesis. All three realizations have in common that the atoms were tightly trapped along the dimensions where cooling has been shown. Cavity cooling can be used for pre-cooling the atoms before Raman and EIT cooling are applied. The latter two are also realized in other laboratories without a cavity enclosing the atoms. Their principles can therefore be explained by describing the cooling of tightly trapped atoms, where the cavity adds modifications but does not change the line of thought.

2.1 Cavity Cooling

Atoms (not necessarily trapped) that are coupled to a cavity mode can be addressed by a single near-resonant laser. For certain laser-atom ($\Delta = \omega_L - \omega_0$) and laser-cavity ($\delta = \omega_L - \omega_c$) detunings cooling of the atomic motional state is observed and referred to as cavity cooling [15].

Many theoretical proposals explain the fundamentals without considering traps that are often confining the atoms in experiments [54–56]. Ideas from these proposals working in the cavity Doppler cooling regime with free atoms, however, often remain valid for trapped atoms [57], where cooling happens in the regime of cavity sideband cooling.

Here the two possible cases of cavity cooling are discussed. Either the near-resonant laser drives the atom or it pumps the cavity.

2.1.1 Pumping the cavity

In our group cavity cooling by pumping the cavity has been applied as a starting point for various experiments [33–35] and is treated extensively in [34] with many references therein.

In [58] an intuitive explanation for this scenario is given by drawing an analogy to Sisyphus cooling [59]. The energies of the singly-excited two atom-cavity dressed states depend on the atom-cavity coupling strength g and therefore on the position of the atom in the intra-cavity standing wave that is formed by the pump light. For properly chosen detunings one of the two dressed states is more likely to get excited at low energies, which happens at certain positions in the standing wave along the cavity axis. As the atom moves along the cavity axis the energy of the excited dressed state increases. If the dressed state now decays and emits a photon, the motional energy of the atom is reduced. Many excitation processes in an energy valley and corresponding emission processes at higher energies lead to Sisyphus-like cooling of the atom.

Within this thesis this mechanism is used to cool the atoms in chapter 4 in the context of non-destructive hyperfine state detection and for initiating the system. There we operate the probe (= pump laser) on resonance with the cavity ($\delta = 0$) and blue detuned from the atomic resonance ($\Delta \approx 2\pi \cdot 20\,\mathrm{MHz}$). In this configuration the state that is used for cooling is the cavity-like dressed state with an excitation width of about the cavity linewidth κ. In analogy to Doppler limited cooling [59] where the atomic linewidth γ_0 limits the final temperature to $T \approx \hbar\gamma_0/k_\mathrm{B}$ the steady-state cooling limit in our case is given by [58]

$$T_z \approx \hbar\kappa/k_\mathrm{B}. \tag{2.1}$$

This equation only holds for non-trapped or weakly confined atoms.

A more rigorous model taking the presence of a deep lattice along the z-axis into account is described in [60]. There for a good cavity ($\Gamma \gg 2\kappa$) the mean vibrational state number in the steady state under cavity cooling is derived as

$$\overline{m}_z \approx \left(\frac{\kappa}{2\pi \cdot \nu_z}\right)^2, \tag{2.2}$$

implying that ground-state cooling can only be reached for $\kappa \ll 2\pi \cdot \nu_z$, which is not the case for our system (cf. table 1.1).

2.1.2 Transversally driving the atom

In the experiments described in chapter 5 transversally driven trapped atoms are strongly coupled to our cavity. The cavity cooling effects which are expected in this situation are published by Stefano Zippilli *et al.* in [61, 62].

The two main results which are relevant to us are: First, the steady-state phonon number after cavity cooling in the good cavity limit is similar to the result for

pumping the cavity and reads

$$\overline{m}_z \approx \left(\frac{2\kappa}{2\pi \cdot \nu_z}\right)^2. \tag{2.3}$$

The second important result from [61] is the laser-atom detuning Δ leading to optimal cooling conditions as a function of the laser-cavity detuning δ and the atom-cavity coupling g

$$\Delta_{\text{opt}}[\delta, g] = \frac{g^2 + \Gamma\kappa/2}{\delta + 2\pi \cdot \nu_z} - 2\pi \cdot \nu_z. \tag{2.4}$$

This implies that optimal cooling close to the laser-cavity resonance ($\delta \approx 0$) and for a typical atom-cavity coupling $g \lesssim g_0$ is realized for $\Delta_{\text{opt}} \sim$ few hundred MHz.

2.1.3 Experimental Realizations

In 1999, the Kimble group – pioneering atom-cavity experiments – realized cavity cooling in the strong coupling regime for the first time. With driven single atoms an atomic lifetime of a few ten ms was reported [63]. In another experiment the group extended the lifetime to the second range utilizing a state-insensitive intra-cavity dipole trap and both atom driving and cavity pumping [64].

Other single-atom experiments in the Rempe group followed [65], reaching a parametric heating limited lifetime on the ten ms scale by pumping the cavity. They were able to extend the lifetime to the 10 s scale by driving the atom inside the cavity, leading to 3D-cooling that was possible due to an additional optical lattice perpendicular to the cavity axis [66]. Also our team was recently able to extend the lifetime to the 10 s scale using cavity cooling with a pumped cavity. Fig. 2.1 shows a gallery shot with a single-atom lifetime of more than one minute. As described in section 1.4 this progress was possible by improving the cavity lock, thereby reducing the parametric heating rate (see section 2.3).

Recently, cavity cooling has also been applied to single trapped ions. In [67, 68] cooling and heating rates as well as temperatures are extracted after driving an ion inside the cavity.

Atomic ensembles in cavities are cooled collectively because the atoms interact via intra-cavity photons. Thereby collective atomic motional modes are addressed, which differs significantly from single-atom cooling. In this context the Vuletić group [69] reports on very strong decelerations and cooling below the Doppler limit. Entering the optomechanical domain in [70] the group cools a collective atomic mode to a mean phonon occupation number $\overline{m} = 2$. Another interesting experiment with a Bose-Einstein condensate (BEC) inside a cavity is published in [71]. A pumped cavity with a very small linewidth of $\kappa = 2\pi \cdot 4.5\,\text{kHz}$ is used to heat and cool the BEC below the atomic recoil limit.

The versatile power of cavity cooling is shown in a review on cavity optomechanics where cavity coupling and cooling of mesoscopic objects like cantilevers, nanoparticles and membranes are discussed [72].

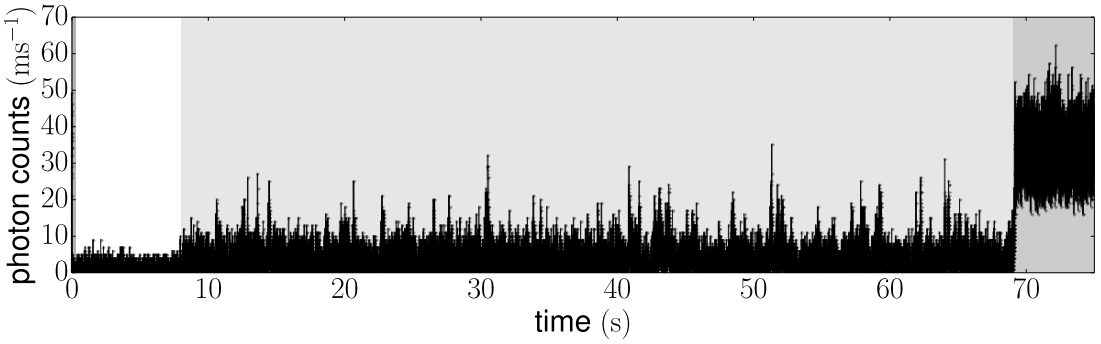

Figure 2.1: Cavity cooling by pumping the cavity. The background colors of the plot indicate the intra-cavity atom number. White corresponds to two, light gray to one and dark gray to zero atoms inside the cavity, respectively. Between 50 ms and 69.1 s the measured cavity transmission is strongly suppressed since first two atoms and then one atom couple to the cavity. The laser is pumping the cavity on resonance ($\delta = 0$) and is blue detuned from the $F = 4$ to $F' = 5$ transiton on the D_2-line of cesium ($\Delta \approx 2\pi \cdot 20\,\mathrm{MHz}$). During cooling a 1 G magnetic field along the y-direction is applied and a repumping laser assures that the atom is held in the $F = 4$ ground state manifold.

A recent review on cavity cooling, covering many of the above cited topics and more can be found in [15].

2.2 Ground-State Cooling of Atoms Inside a Cavity

In contrast to cavity cooling, EIT (= electromagnetically induced transparency) and Raman sideband cooling require the atom to be tightly trapped along the cooling directions. This requirement is connected to the fact that a cooling cycle in these two cases starts with coherently lowering the motional state number m_i but needs to be completed by an incoherent scattering event. The incoherent scattering event should not change $|m_i\rangle$ (see subsection 2.2.1 on Raman cooling). Assuming a harmonic trapping potential (see subsection 1.5), this condition is fulfilled if the recoil frequency $\omega_{\mathrm{rec}} = \hbar k_0^2/(2M)$ is much smaller than the trap frequency $2\pi \cdot \nu_i$. In other words: the recoil from a scattered photon with wavelength $\lambda_0 = 2\pi/k_0$ is very unlikely to change the atomic motional state number along the cooling direction i. This condition can also be stated by introducing the Lamb-Dicke parameter η_i

$$\eta_i = \sqrt{\omega_{\mathrm{rec}}/(2\pi \cdot \nu_i)} \overset{\text{Eq. (1.16)}}{=} k_0 \Delta x_0[\nu_i] \overset{!}{\ll} 1, \tag{2.5}$$

which needs to be much smaller than unity. For our system parameters in table 1.1 the Lamb-Dicke parameters along the trap axes (see Fig. 1.1) are calculated to be $\{\eta_x, \eta_y, \eta_z\} \approx \{1, 0.07, 0.1\}$. Therefore EIT and Raman cooling could work along

the cavity- and along the red dipole trap-axis but not along the weakly confined x-axis.

Lowering the momentum of a trapped atom by a coherent two-photon process is only possible if the momentum taken from the particle can be transferred to one of the two laser beams. For counterpropagating laser beams with wave vectors $\vec{k}_1$ and $\vec{k}_2$ this momentum transfer becomes maximal while it vanishes for copropagating beams. The figure of merit is the two-photon Lamb-Dicke parameter [35, 73, 74]

$$\eta_i^{(\mathrm{tp})} = \vec{e}_i \cdot (\vec{k}_1 - \vec{k}_2)\Delta x_0[\nu_i], \tag{2.6}$$

where $\vec{e}_i$ is the unit vector along the cooling direction i. For $\eta_i^{(\mathrm{tp})} = 0$ the cooling sideband cannot be addressed and cooling is suppressed.

Finally one last condition concerning the onset of cooling has to be met. If the atom is well-localized (better than $1/k_0$) along the cooling axis it is said to be in the Lamb-Dicke regime. Within this regime higher order transitions during the repumping process (see following subsection) are suppressed and sideband cooling is efficient. Entering the Lamb-Dicke regime means fulfilling [75]

$$\eta_i\sqrt{2m_i + 1} \ll 1. \tag{2.7}$$

Reports on experiments with relatively hot atoms at the beginning of the sideband cooling process stress the difficulty to reach the motional ground state [18]. In chapter 4 we solve this problem by applying cavity cooling in a precooling stage.

All the above criteria have to be met for efficiently cooling atoms by EIT or Raman sideband cooling with and without coupling the atoms to an optical cavity.

2.2.1 Raman Cooling

Raman sideband cooling[1] is one of the most prominent cooling schemes for trapped ions and atoms. The general scheme is reviewed in [75]. In contrast to EIT cooling, here the cavity does not modify the cooling dynamics [17]. Therefore we can neglect the cavity for an introduction to the scheme. Fig. 2.2 illustrates the general Raman cooling scheme. Two lasers with frequencies ω_L and ω_R and Rabi frequencies Ω_L and Ω_R couple the two ground states $|\uparrow\rangle$ and $|\downarrow\rangle$ to a common excited state $|e\rangle$. The detunings Δ_L and Δ_R of the lasers are huge compared to the often power-broadened width of the excited state ($\Delta_{L,R} \gg \Gamma, \Omega_{L,R}$) and nearly equivalent $\Delta_L \approx \Delta_R$. The dynamics depend on the two-photon detuning $\delta_{\mathrm{tp}} = \Delta_R - \Delta_L$. Setting δ_{tp} to $-2\pi\nu_i$, 0 and $2\pi\nu_i$ the transitions $|\uparrow, m_i\rangle \leftrightarrow |\downarrow, m_i + 1\rangle$, $|\uparrow, m_i\rangle \leftrightarrow |\downarrow, m_i\rangle$ and $|\uparrow, m_i\rangle \leftrightarrow |\downarrow, m_i - 1\rangle$ are addressed. These transitions are named heating sideband, carrier and cooling sideband transition, respectively.

Fig. 2.2 shows the case of sideband cooling where the two-photon detuning matches the trap frequency along the cooling direction i: $\delta_{\mathrm{tp}} = 2\pi \cdot \nu_i$. A cooling

[1] Within this thesis we do only discuss the case of trapped particles with motional sidebands that can be resolved by the Raman beams. The terms "Raman cooling" and "Raman sideband cooling" are used as synonyms.

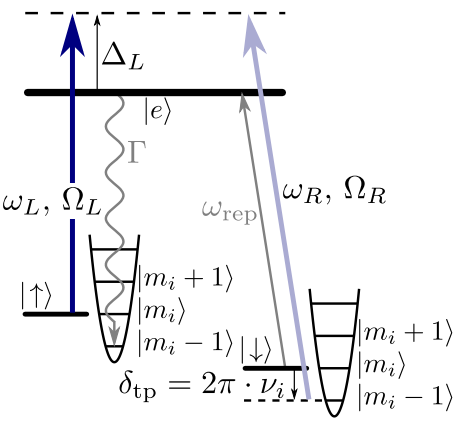

Figure 2.2: Illustration of Raman sideband cooling. An atom with two stable electronic ground states $|\uparrow\rangle$ and $|\downarrow\rangle$ is cooled by driving the transitions $|\uparrow, m_i\rangle \rightarrow |\downarrow, m_i\rangle$ on the cooling sideband, followed by a repumping process. For optimal cooling the two-photon detuning is adjusted to $\delta_{\mathrm{tp}} = 2\pi \cdot \nu_i$.

cycle is started with the Raman beams coherently transferring the atomic population from $|\uparrow, m_i\rangle$ to $|\downarrow, m_i - 1\rangle$, driving the cooling sideband. The cooling cycle is completed by scattering repumper photons with frequency ω_{rep}. In the Lamb-Dicke regime (cf. Eq. (2.7)), this mainly leads to incoherent pumping from $|\downarrow, m_i - 1\rangle$ to $|\uparrow, m_i - 1\rangle$, not changing the motional state. During the Raman cooling all three lasers can be permanently on. The scattering rate of the repumping laser Γ_{rep} should be on the same order of magnitude as the Raman Rabi frequency $\Omega_L\Omega_R/\Delta_L$ [20]; pulsed Raman cooling schemes, which drive π-pulses on the cooling sideband, are more efficient [74, 75].

The limit imposed on the minimal steady-state average phonon number after Raman cooling comes from off-resonant stimulated Raman transitions (= off-resonantly driving transitions which are not on the cooling sideband) [74] and an imperfect suppression of m_i-changing transitions during the repumping process due to a non-zero Lamb-Dicke factor η_i [17]. Reference [75] estimates the cooling limit for an optimized system with

$$\overline{m}_i \approx \frac{5}{4}\left(\frac{\Gamma_{\mathrm{rep}}}{2 \cdot 2\pi\nu_i}\right)^2 . \tag{2.8}$$

In 1995 the Wineland group first showed Raman ground-state cooling of a single $^9Be^+$ ion in a Paul trap. In more than 90% of the cooling attempts the 3D motional ground state was reached ($p_0 = 90\%$, see Eq. (1.21)) [74].

Shortly thereafter, the Jessen group achieved to cool neutral atoms in an optical lattice to the 2D ground state with $p_0 > 95\%$ [50]. In the Chu group ensembles of cesium atoms were trapped in optical lattices and Raman cooled to high phase-space densities. A modified Raman sideband cooling method was used. Instead of using different hyperfine levels as ground states, degenerate Zeeman levels with different motional state numbers but the same stable hyperfine level were addressed [76, 77].

Recently, Raman ground-state cooling of a single atom in a tightly-focused optical tweezer has been performed by different groups [18, 19].

Neutral atoms strongly coupled to an optical cavity were first Raman cooled by the Kimble group. A single atom in an optical cavity reached the 1D motional

ground state along the cavity axis with a probability of $p_0 = 95\%$ [20]. Reference [17] gives a detailed description of Raman transitions and Raman cooling in the context of CQED. Finally in 2013, about 20 years after the first realization of Raman sideband cooling, the Rempe group was able to apply the technique to cool an atom strongly coupled to an optical cavity for the first time to its 3D motional ground state with $p_0 = 89\%$ [21].

2.2.2 EIT cooling

EIT (= electromagnetically induced transparency) [78] is an effect where two near-resonant laser beams alter the dispersive and absorptive response of an effective three-level atom. The system of two beams, coupling two ground states to the same excited state, is characterized by the beams' relative detuning with respect to the excited state. If this relative detuning δ_{tp} vanishes, the atom becomes transparent for both beams. The transparency is based on destructive interference between the two excitation paths addressed by the two lasers.

Fig. 2.3 shows a cartoon of the situation. Part (a) shows the atomic level scheme with the driving lasers. The atoms are tightly trapped along the cooling direction with trap frequency ν_i but no cavity coupling is present. The situation is well described by assuming a positive but near-resonant one-photon detuning $\Delta_{\mathrm{con}} \gtrsim \Gamma$ and a strong control laser ($\Omega_{\mathrm{con}} > \Omega_p$). Fig. 2.3(b) shows the narrow EIT absorption peak which can be used for cooling. The figure is drawn for $2\pi \cdot \nu_i = \delta_{\mathrm{abs}}$ where the optimal cooling conditions are realized. For $\delta_{\mathrm{tp}} = 2\pi \cdot \nu_i$ the carrier transitions $|m_i\rangle \rightarrow |m_i\rangle$ are completely suppressed while cooling transitions $|m_i\rangle \rightarrow |m_i - 1\rangle$, sitting on the absorptive peak, are enhanced [73]. A cooling cycle is closed by an incoherent repumping process due to off-resonant Raman-scattering of the near-resonant laser beams.

One of the main parts in Tobias Kampschulte's thesis [35] is the description of EIT cooling for our system. Here I want to quote two equations written and referenced in his thesis. These two facts become important for the experimental considerations in section 2.3. First the distance in frequency space between the two-photon resonance ($\delta_{\mathrm{tp}} = 0$) and the narrow EIT absorption peak is

$$\delta_{\mathrm{abs}} \approx \Omega_{\mathrm{con}}^2/(4\Delta_{\mathrm{con}}). \tag{2.9}$$

Second, the full width at half maximum of the absorption peak is well approximated by

$$\Delta\delta_{\mathrm{abs}} \approx \Gamma\Omega_{\mathrm{con}}^2/(4\Delta_{\mathrm{con}}^2). \tag{2.10}$$

The theory of EIT cooling is described in [79] without and in [16] with a cavity. EIT cooling within a cavity is richer and more complicated than standard EIT cooling. For our parameters, however, the limiting cooling temperature is independent of cavity parameters and for low saturation given by [73]

$$\overline{m}_i \approx \Gamma\Delta\delta_{\mathrm{abs}}/\Omega_{\mathrm{con}}^2. \tag{2.11}$$

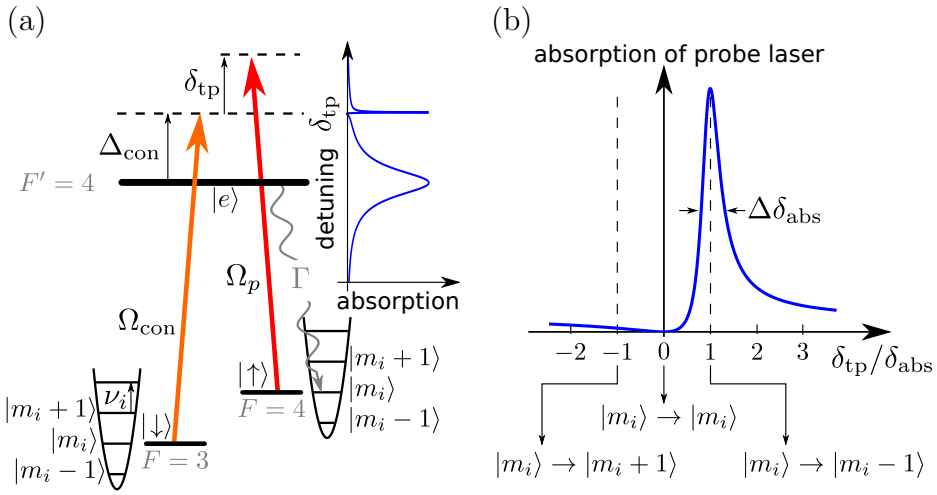

Figure 2.3: Illustration of EIT cooling adapted from [35, 79]. (a) EIT Λ-configuration of the two ground states $|\uparrow\rangle$ and $|\downarrow\rangle$ being coupled by the control and the probe laser with Rabi frequencies Ω_{con}, Ω_p, respectively. (b) Calculated narrow EIT resonance. The two-photon detuning δ_{tp} is plotted in multiples of the EIT absorption shift δ_{abs}. The resonance has a width of $\Delta\delta_{\mathrm{abs}}$.

Theoretically this implies that colder temperatures can be reached for larger single photon detunings Δ_{con} since the width of the EIT resonance becomes smaller. Standard EIT ground-state cooling has been first realized with ions in the Blatt group [80]. Our group was the first one to show standard EIT cooling of atoms [81] and cavity-EIT cooling [82].

2.3 Comparison of Intra-Cavity Cooling Schemes

It is important to note that atom-cavity experiments often suffer from parametric heating [38, 83] along the cavity axis which originates from intensity fluctuations of the lock laser trap (see Fig 1.1(b)). These arise from a non-perfect stabilization of the cavity frequency to the lock laser and, in our case, heat the atoms out of the intra-cavity traps on a timescale of a few hundred ms, if no cooling is applied. Practically this means that the cooling rate, which has not been considered so far, has to be higher than the parametric heating rate in order to achieve any cooling effect. Furthermore, the achievable steady-state mean photon number $\overline{m}$ and ground-state population p_0 (related to each other by Eq. (1.21)) will be higher than the above given theoretical limits and will depend on the net cooling and net heating rate A_- and A_+, respectively. The expected dependency is given by $\overline{m} = A_+/(A_- + A_+)$ [84].

Experimentally the parametric heating rate depends on the fluctuating daily performance of the rather advanced cavity lock system, cf. section 1.4. Therefore

	Method	$p_0^{(\mathrm{exp})}/\%$	$p_0^{(\mathrm{theo})}/\%$	Eq.	Comments
(i)	Pumping cavity	18(8)	91	(2.2)	$\delta = 2\pi \cdot 0\,\mathrm{MHz}$, $\Delta = 2\pi \cdot 20\,\mathrm{MHz}$, $n_p^{(\mathrm{opt})} = 0.15$
(ii)	Driving atom	9(8)	71	(2.3)	$\delta = 2\pi \cdot 0\,\mathrm{MHz}$, $\Delta = 2\pi \cdot 20\,\mathrm{MHz}$, $I_L^{(\mathrm{opt})} = 1\,\mathrm{mW/cm^2}$
(iii)	Standard Raman	—	91	(2.8)	Two counterpropagating running waves as Raman beams
(iv)	Carrier-free Raman	90.9(8)	98	(4.12)	One standing wave one $\perp$ running wave as Raman beams
(v)	EIT	—	98	(2.11)	Theoretical limit based on experimental values given in [82]

Table 2.1: Ground state occupation p_0 for different cooling methods applied to a cesium atom strongly coupled to our cavity. The theoretical values are calculated with the given equations and Eq. (1.21) for $\nu_z = 2\pi \cdot 200\,\mathrm{kHz}$. All experimental values are measured by taking motional sideband spectra (cf. subsection 4.2.4) directly after the atoms are cooled to their steady state with the respective cooling method. Errors are fit errors. (i, ii) The optimal intra-cavity photon number $n_p^{(\mathrm{opt})}$ and the optimal intensity $I_L^{(\mathrm{opt})}$ of the cooling beams are found by experimentally maximizing the lifetime of the atoms inside the cavity. (iii, iv) The theoretical values are calculated for $\Gamma_{\mathrm{rep}} = 2\pi \cdot 0.7\,\mathrm{MHz}$ that corresponds to the expected state-changing scattering rate calculated from the experimental parameters of the repumping laser ($I_{\mathrm{rep}} = I_{\mathrm{sat}}$, $\Delta_{\mathrm{rep}} = \omega_{\mathrm{rep}} - \omega_0 = 0$, see section 4.2 and Fig. 4.2 therein).

we cannot easily apply the theoretical limits to our experiment.

However, table 2.3 compares the theoretical limits without parametric heating taken into account to experimental values measured during this thesis work.

As expected, the theoretical limits show higher ground-state populations than their measured complements.

Furthermore, comparing the experimental results to each other, one finds that method (i) is more efficient than method (ii), as predicted by the theory. More importantly, method (iv) cools the atomic population close to the ground state, which is in good agreement with the theoretical expectation. In the experiments in chapter 4 we utilize method (i) to precool the atoms into the Lamb-Dicke regime (see Eq. (2.7)) where method (iv) is applied to reach the 2D motional ground state.

For method (iii) and (v) no quantitative experimental results are obtained here. Method (iii) is not favorable over method (iv) since it requires more resources and is harder to implement due to the limited optical access (see chapter 4).

Method (v) is a special case and illustrates a "negative" research result. EIT cooling of atoms inside the cavity has been studied extensively in our group [35, 81, 82]. In contrast to the Raman-cooling methods EIT cooling is based on near-resonant transitions. Therefore off-resonant Raman scattering hinders coherent population transfer, which is essential to sideband spectroscopy revealing p_0, see subsection 4.2.4. During my thesis work significant but unsuccessful effort has been taken to quantify the efficiency of this scheme beyond survival measurements, which do not offer a clear connection to p_0.

Concretely, we tried to apply heterodyne spectroscopy in order to extract the atomic temperature after EIT cooling via steady-state thermometry [85]. Experimentally, this method works only if the atom is driven close to the $F = 4 \rightarrow F' = 5$-transition of the cesium D_2-line. Therefore Ω_p in Fig. 2.3 needs to drive this transition, which necessarily implies that $\Delta_{\mathrm{con}} \approx 50\Gamma$, see Fig. 2.3(a). This leads to a rapid decrease of the cooling peak width $\Delta\delta_{\mathrm{abs}}$ (see Eq.(2.10)), that cannot be compensated by an arbitrarily large increase of Ω_{con} (power broadening), because the EIT-cooling condition $2\pi \cdot \nu_z = \delta_{\mathrm{abs}}$ needs to be fulfilled. Considering $\delta_{\mathrm{abs}} \propto 1/\Delta_{\mathrm{con}}$ (cf. Eq.(2.9)) but $\Delta\delta_{\mathrm{abs}} \propto 1/\Delta_{\mathrm{con}}^2$ (cf. Eq.(2.10)) it becomes evident that the cooling peak width Δ_{abs} shrinks with an increase of the detuning Δ_{con}. This effect is detrimental to EIT-cooling of atoms that are trapped in a standing-wave lattice. Here with increasing motional state number m_z the sideband transition frequencies decrease, due to the anharmonicity of the trapping potential, by about one lattice recoil frequency $\omega_{\mathrm{rec}} \approx 2\pi \cdot 2\,\mathrm{kHz}$ as $m_z \rightarrow m_{z+1}$: The resolved EIT-sideband cooling fails because only atoms in specific neighboring motional states fulfill the cooling condition that gets stricter with a narrower cooling peak width $\Delta\delta_{\mathrm{abs}}$. For our parameters one finds $\Delta\delta_{\mathrm{abs}} \approx 2\pi \cdot 4\,\mathrm{kHz}$ meaning that maximally two neighboring motional states can be efficiently cooled. This leads to a failure of the scheme since thermally excited population not being in one of these two states cannot be addressed.

In conclusion EIT cooling of cavity-coupled atoms only works for small laser-atom detunings and its quantitative performance is hard to measure without an

additional Raman setup for sideband spectroscopy. In contrast to this the carrier-free Raman method is versatile and its performance is easily quantified by its intrinsically available sideband spectroscopy. The cavity cooling schemes can serve for precooling but cannot reach a significant ground-state population within our current apparatus.

3 Non-Destructive Hyperfine State Detection Inside an Optical Cavity

Extraction of quantitative information from the system of interest is one of the main experimental challenges. In the proceeding section 2.3 it became clear that the main disadvantage of the EIT-cooling scheme was not connected to the scheme's performance, but to the fact that it was not possible to gain quantitative information about the temperature of an EIT-cooled atom.

Here a fast, reliable and non-destructive internal state-detection method is introduced and will be used in chapter 4 to extract the temperature of the atoms after Raman cooling inside the cavity.

The non-destructive state-detection scheme delivers binary information about the electronic ground states $F = 3, 4$ of cesium atoms coupled to the cavity. This information is of importance not only to the work presented within this thesis, but also to planned experiments like a two-atom entanglement scheme inside the cavity or the realization of a quantum-dot atom-cavity hybrid system.

3.1 Comparison to Other State-Detection Schemes

In many experiments the atomic hyperfine state is detected by the push-out technique [86]: Using a running-wave laser, atoms in $F = 4$ are pushed out of the trap by resonant radiation pressure, whereas atoms in $F = 3$ remain trapped. While this technique is useful in free space cold atom experiments with many atoms, it has several disadvantages in our case. First, the experiments described below are based on hyperfine state detection of a single atom. If the push-out technique is applied, the atom has to be reloaded (cf. chapter 1) after each single measurement leading to a MOT-loading limited repetition rate below 1 Hz and poor statistics. The push-out induced loss of the atom from its trap makes the technique a "destructive" scheme. Second, the atomic motional state has to be inferred from the detected hyperfine state *inside* the cavity. The given limited optical access would complicate the task to implement the needed push-out beam.

Another well known state detection method – developed in the ion community [75] – is based on electron shelving and detection of resonance fluorescence, and can be extended to neutral atom state detection [87,88]. The working principle of this scheme is to shine a laser on the atom that resonantly couples one of the two internal ground states to some short-lived excited state, but not the other one. If the measurement projects the atom into the resonantly coupled ground state (often

called *bright state*) atomic fluorescence is detected. If the atom is projected to the other ground state (*dark state*), ideally no light is measured at the detector. The possibility to use one and the same atom for many subsequent measurements is the advantage of this non-destructive scheme.

3.2 Non-Destructive State-Detection Scheme

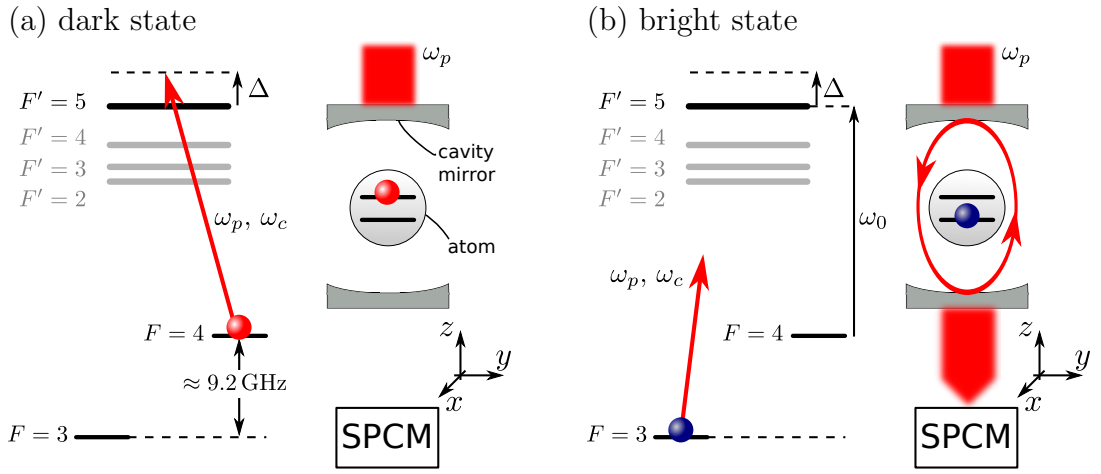

Figure 3.1: Internal state detection: Schematic Cs-level schemes and simplified detection setups are shown. (a) The atom in $F = 4$ couples via the excited $F' = 5$ state to the cavity. This coupling leads to a shift of the cavity resonance. Ideally nearly no light enters the cavity. The single photon counting module (SPCM) measures a low photon click rate. (b) The atom is in $F = 3$. Atomic resonances are far detuned from the cavity resonance. Atom-cavity coupling is negligible. The cavity resonance is not changed, probe light is coupled into the cavity and detected with the SPCM.

It is elegant and efficient to utilize the strong atom-photon interaction intrinsic to the atom-cavity system for a detection scheme based on the concept of a bright and a dark state [20, 89–92]. The rate of photons leaking out of the cavity contains the information on the internal atomic state. In our case the cavity-enhanced detection scheme is based on a dressed state shift: We tune the cavity to the blue side of the $F = 4 \rightarrow F' = 5$ D_2-line transition but on resonance with the probe laser ($\delta = \omega_p - \omega_c = 0$, $\Delta = \omega_p - \omega_0 \approx 2\pi \cdot 20\,\mathrm{MHz}$). In this regime cavity cooling assures good coupling during $F = 4$ state detection. An atom in $F = 4$ inside the cavity shifts the cavity-like dressed state out of resonance with the probe laser. The cavity transmission is significantly reduced. An atom in $F = 3$ inside the cavity leads to a transmission not different to the empty cavity case, since the cavity is far detuned ($\approx 9.2\,\mathrm{GHz}$) from the atomic resonance (see Fig. 3.1). Experimentally all state-detection based experiments described in this thesis follow the same procedure.

Fig. 3.2 shows the time line of a single experimental run. Typically – to gain statistics – about 100 runs are measured. The measurement sequence fulfills our two criteria of measuring the state inside the cavity and accumulating the data rapidly. The typical repetition number N can be > 100, leading to a data accumulation rate above 10 Hz. N is only limited by atom losses from the cavity. The cooling step (1) leads to intra-cavity lifetimes on the order of seconds. Here we use cavity cooling (see section 2.1) or Raman sideband cooling (see subsection 4.2.4). The manipulation step (3) defines the actual experiment. Raman laser or microwave manipulation are possible as well as intra-cavity cooling or heating measurements. State detection in (4) happens with the probe light as the only near resonant laser. In step (5) we apply the probe laser (see Fig. 3.1) together with a strong repumping laser (repumper) resonant the to $F = 3 \rightarrow F' = 4$ transition. If the atom is still well confined within the cavity mode, the count rate on the SPCM will be below some threshold level and we use the detection data for analysis. If the counts are above the threshold level the detection data of this repetition is discarded.

The principles of our cavity-enhanced detection scheme are also discussed in [33, 34].

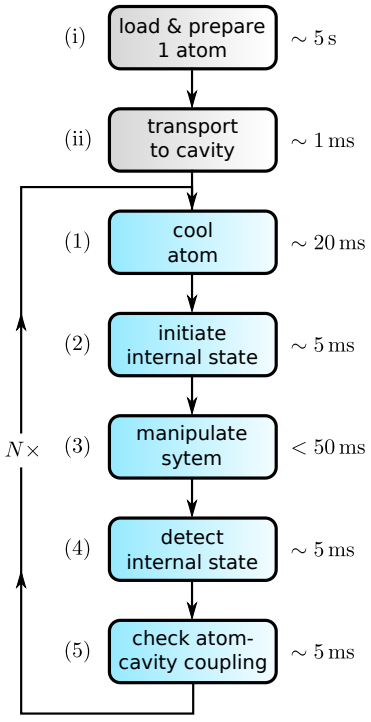

Figure 3.2: Time line of experiments with state detection.

3.3 Variable Threshold Method

The detection of the internal state in Fig. 3.2 could be considered a quantum non-demolition measurement [93, 94], if the probe laser would not change the internal spin state by off-resonant Raman scattering during the measurement process. In this case it is beneficial to measure as many photons as possible. To illustrate this, Fig. 3.3 shows typical measured cavity-transmission signals. (a) and (b) are the time traces of one strongly coupled atom (equal to one atom in $F = 4$, dark state) and of empty cavity transmission (equal to one atom in $F = 3$, bright state), respectively. The detected photon number in (a) significantly fluctuates on a timescale of tens of ms. These fluctuations arise from atom hopping along the lock-laser lattice (see also subsection 5.3.3), leading to a fluctuation of the atom-cavity coupling strength g, which becomes visible in the cavity transmission. In case of (b) the observed fluctuations happen on a longer timescale and cannot be at-

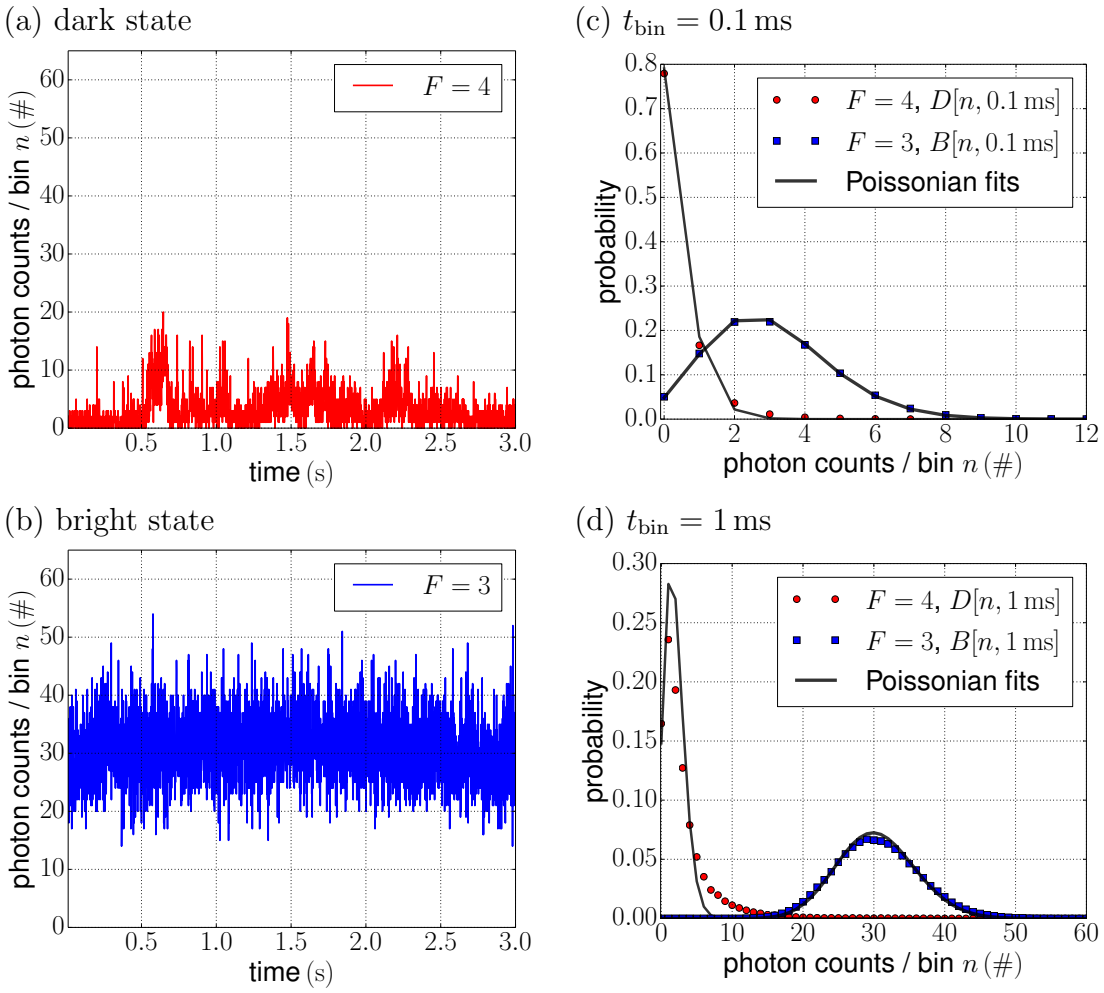

Figure 3.3: Measured cavity transmission for atoms in $F = 4, 3$. (a) and (b) show typical time traces of a strongly coupled atom in $F = 4$ (strong repumper on) and of the empty cavity (equal to $F = 3$) with a bin size of 1 ms. (c) and (d) show probability density functions (PDFs) with a bin size of 0.1 ms and 1 ms, respectively. The absolute measurement errors of the PDF data points are smaller than the data points. The PDFs are build from tens of traces like those shown in (a) and (b).

tributed to g-fluctuations since the cavity is empty. The fluctuations in (b) are explained by length variations of unwanted Fabry-Pérot interferometers in the optical setup in front of the cavity. The interferometers form between optical surfaces such as fiber ends, the science cell containing the cavity, the input cavity mirror, et cetera. The lengths of the interferometer arms change due to vibrations and thermal drifts, which leads to changes in the empty cavity transmission signal. Another effect leading to short time fluctuations of the empty cavity transmission signal is connected to the non-perfect cavity lock (the lock is described in sec-

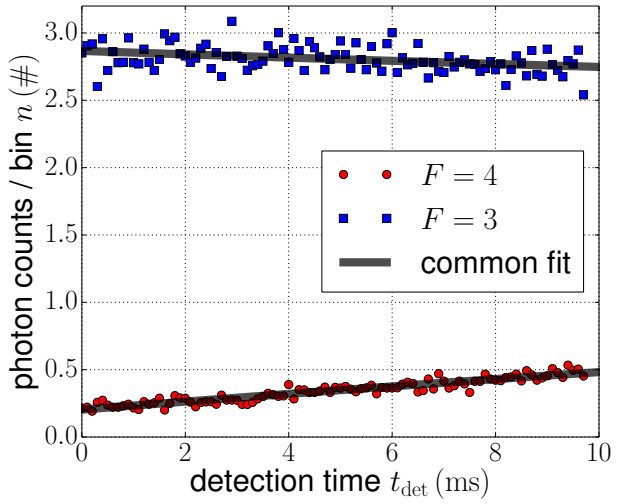

Figure 3.4: State detection raw data (bin size = 0.1 ms). Before the measurement the internal atomic state $F = 4, 3$ is prepared. Each of the two data sets is the average of more than 400 single measurements, reflecting the internal quantum jumps in an exponential change of the signal. Simultaneous exponential fits to the data are shown (see Eq. (3.1)).

tion 1.4). Due to lock fluctuations (close to 50 kHz) the cavity resonance changes and the probe laser transmission is decreased (short drops). For state detection this effect does not matter since it is much faster than our typical ms detection time. The fluctuations governing (b) do also exist in (a), but are superimposed by the more significant atomic motion effect. This can be seen in the bright and dark histograms $B[n, t_{\mathrm{bin}}]$ and $D[n, t_{\mathrm{bin}}]$ in (c) and (d) where more than 100 s of $F = 3$ and $F = 4$ time data are binned with different bin sizes t_{bin}. Further best fits of Poisson distributions to the data are shown. If the data was only shot noise limited without any of the above described fluctuations, it could be described by Poisson distributions on any time scale. Using a bin time of 0.1 ms in (c) the bright state data seems Poissonian, whereas the dark state data is broader than its best fit and therefore Super-Poissonian. For a bin size of 1 ms in (d) both histograms are clearly Super-Poissonian.

Aiming at measuring the internal atomic state, it seems to be beneficial to measure as long as possible since Fig. 3.3 illustrates that the measured normalized histograms (= probability distribution functions = PFDs) overlap less and less for longer detection times $t_{\mathrm{det}} = t_{\mathrm{bin}}$. This means discriminating the two states should be easier for longer detection times. In a histogram-based detection analysis, a measured number n of photons per bin would be evaluated with the measured PDFs. Here the detection time t_{det} is fixed and equals the bin time t_{bin}. If $D(n, t_{\mathrm{det}}) > B(n, t_{\mathrm{det}})$ the atom would be detected as dark, else it would be detected as bright. However, during the measurement two unwanted state-changing processes can happen which destroy a quantum nondemolition measurement. If the atom is projected into the dark state $F = 4$ at the beginning of the measurement, off-resonant Raman scattering via $F' = 4, 3$ can lead to a mainly probe-induced quantum jump to the bright state $F = 3$. On the other hand an initial projection of the atom into the bright state can also be changed to the dark state by off-resonant Raman scattering, involving the probe and the trapping lasers (dipole trap and lock laser). Both processes are detected during the state measurement and

$\tau_{4\to3}$	$\bar{T}_4$	$\tau_{3\to4}$	$\bar{T}_3$
(88.3 ± 7.6) ms	$(0.203 \pm 0.014)\,\mathrm{ms}^{-1}$	(207 ± 42) ms	$(2.867 \pm 0.014)\,\mathrm{ms}^{-1}$

Table 3.1: Decay constants and mean cavity transmissions of the dark and the bright state, deduced from data in Fig. 3.4. The errors are fit errors.

illustrated in Fig. 3.4. *The figure shows the detection data that will be used within this chapter to compare and benchmark different analysis techniques.* The atom has been prepared in a well defined internal state while a constant B-field of 0.1 G is applied along the y-direction, see Fig. 1.1. Starting a state detection in $F = 4$ or $F = 3$, a quantum jump from $4 \to 3$ or $3 \to 4$ can happen, respectively. Averaging over many individual realizations of these experiments, exponential changes of the cavity transmission signals are observed. The exponential cavity transmission traces are described by

$$T[t] = p_3[t] \cdot \bar{T}_3 + p_4[t] \cdot \bar{T}_4, \tag{3.1}$$

where $\bar{T}_3, \bar{T}_4$ are the mean cavity transmissions for an atom in $F = 3, 4$ and p_3, p_4 are the probabilities of the atom to be in $F = 3, 4$, respectively. The probabilities obey the two coupled rate equations

$$\frac{d}{dt}p_{4,3}[t] = \mp\frac{1}{\tau_{4\to3}}p_4[t] \pm \frac{1}{\tau_{3\to4}}p_3[t], \tag{3.2}$$

and $p_4[t] = 1 - p_3[t]$. The rate equations are solved for $p_4[t]$ and $p_3[t]$ with the initial condition $p_{4,3}[t] = 1$ for the red, blue curve in Fig. 3.4, respectively. The solutions depend on four parameters, are exponential functions of time, and are used in Eq. (3.1) for a common fit to the data. The resulting four optimal parameters are shown in table 3.1. We are mainly interested in the two decay constants $\tau_{4\to3}$ and $\tau_{3\to4}$, describing the decay from the dark to the bright state and vice versa.

If an atom was initially projected to one state, but then jumped to the other state, remaining there for the rest of the detection time[1], a histogram-based detection analysis would lead to a higher measurement error for longer detection times. The measurement error $\epsilon_{4,3}$ is defined as the probability to measure $F = 3, 4$ even though $F = 4, 3$ has been prepared in step (3) of Fig. 3.2. The fidelity of a measurement is commonly defined with the average readout error $\epsilon = (\epsilon_4 + \epsilon_3)/2$ [95, 96].

Using a histogram-based detection analysis would lead to a bad fidelity, since ϵ increases unnecessarily fast for long detection times due to the described quantum jumps. Therefore we choose a two dimensional optimization strategy [97]. The two parameters that are varied are the maximum time t_{det} taken into account for state detection and the threshold photon number n_{th}. If the photon number n detected within t_{det} fulfills $n < n_{\mathrm{th}}$ the atom is detected to be in the dark state, else it is detected to be in the bright state. Fig. 3.5 shows the mean detection error ϵ as a

[1] Higher order processes, meaning many jumps between the two states, can be neglected from now on since $1/t_{\mathrm{det}} \gg$ jump rates.

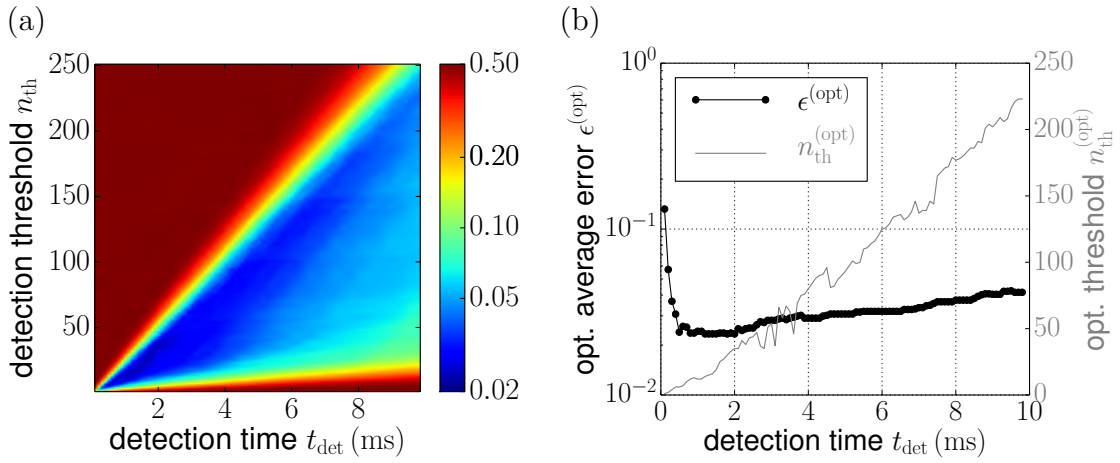

Figure 3.5: Variable threshold method ($t_{\mathrm{bin}} = 0.1\,\mathrm{ms}$). (a) shows a logarithmic color plot of the mean detection error ϵ as a function of the maximum detection time t_{det} and the detection threshold n_{th}. In (b) the minimum error $\epsilon^{(\mathrm{opt})}$ for each t_{det} in (a) is calculated. Further the corresponding optimal threshold $n_{\mathrm{th}}^{(\mathrm{opt})}$ is shown.

function of the detection time and the detection threshold. The underlying data is the same as in Fig. 3.4. The color plot in Fig. 3.5 (a) shows that choosing n_{th} too high (low) results in always detecting the dark (bright) state. These scenarios lead to a mean detection error of 50% (red areas in the plot). The part (b) of the figure shows the minimum mean error $\epsilon^{(\mathrm{opt})}$ which can be achieved by choosing the optimal threshold $n_{\mathrm{th}}^{(\mathrm{opt})}$ for a given maximum detection time t_{det}. The relative statistical uncertainty of $\epsilon^{(\mathrm{opt})}$ is smaller than 50% for all t_{det}, leading to a minimum error $\epsilon^{(\mathrm{opt})} = (2.4^{+1.0}_{-0.8})\%$ for $t_{\mathrm{det}} \in [1, 2]\,\mathrm{ms}$. The optimal threshold $n_{\mathrm{th}}^{(\mathrm{opt})}$ increases with the detection time, as expected from the time dependence of the PDFs (see Fig. 3.3 (c, d)). Detection times exceeding 2 ms lead to a decrease of the detection fidelity due to the described quantum jumps, while detecting for less than $\approx 0.5\,\mathrm{ms}$ reduces the fidelity due to the increasing overlap of the PDFs.

3.4 Maximum Likelihood Method

The state detection data is recorded as a time resolved sequence of photon clicks (cf. chapter 1). State detection based on the variable threshold approach implies choosing a reasonable detection time t_{det} (in our case 1 to 2 ms) and evaluating a single, time-independent variable, which is the photon number in a bin of size $t_{\mathrm{bin}} = t_{\mathrm{det}}$. Using the variable threshold method, a quantum jump within the detection time t_{det} can lead to a detection error. The photon arrival time information, however, can be used to reduce such errors. A time-resolved approach could avoid some of

	$\overline{\epsilon}_4/(\%)$	$\overline{\epsilon}_3/(\%)$	$\overline{\epsilon}/(\%)$
max. likelihood	1.37 ± 0.00	2.95 ± 0.00	2.16 ± 0.00
var. th. method	1.70 ± 0.12	3.02 ± 0.11	2.36 ± 0.03

Table 3.2: Comparison between maximum likelihood and variable threshold detection methods. The errors are the time averages of the data shown in Fig. 3.6 for $t_{\mathrm{det}} \in [1.0, 2.0]$ ms. The variance of the data in this time interval gives rise to the errors. Here statistical errors as in Fig. 3.6 are not taken into account, since the focus is on the state detection method.

the errors by taking into account the possibility of a quantum jump within t_{det}. Having detected a time-resolved sequence of photon clicks, we ask the question: What is the probability that this sequence has been generated under the condition of a dark (bright) atom *at the beginning* of the measurement? The answer is given by a maximum likelihood method, meaning Bayesian conditional probability calculus with uniform priors ($p_4(t=0) = p_3(t=0) = 0.5$). These probabilities are calculated to be [95, 98]:

$$\begin{aligned} p_4 = p[\{n_i\}|D_{t=0}] &= \left(1 - \frac{t_{\mathrm{det}}}{\tau_{4\to 3}}\right) \prod_{i=1}^{N} D(n_i, t_{\mathrm{bin}}) \\ &+ \frac{t_{\mathrm{bin}}}{\tau_{4\to 3}} \sum_{j=1}^{N} \prod_{i=1}^{j-1} D(n_i, t_{\mathrm{bin}}) \prod_{i=j}^{N} B(n_i, t_{\mathrm{bin}}) \\ p_3 = p[\{n_i\}|B_{t=0}] &= \left(1 - \frac{t_{\mathrm{det}}}{\tau_{3\to 4}}\right) \prod_{i=1}^{N} B(n_i, t_{\mathrm{bin}}) \\ &+ \frac{t_{\mathrm{bin}}}{\tau_{3\to 4}} \sum_{j=1}^{N} \prod_{i=1}^{j-1} B(n_i, t_{\mathrm{bin}}) \prod_{i=j}^{N} D(n_i, t_{\mathrm{bin}}). \end{aligned} \tag{3.3}$$

Tthe click data is binned with a bin size $t_{\mathrm{bin}} \ll t_{\mathrm{det}}, \tau$ with $N = t_{\mathrm{det}}/t_{\mathrm{bin}}$ bins $\{n_i\}$, containing the number of detected photons. In both equations in Eq. (3.3) the first summands describe the probability that the initially detected state at $t = 0$ is still there after t_{det}. The second summands describe quantum jumps within $t \in [0, t_{\mathrm{det}}]$, quantized by multiples of t_{bin}. The weighting factors in front of the PDFs arise from exponential probability functions in the limit $t_{\mathrm{bin}}, t_{\mathrm{det}} \ll \tau$ [97].

We implement Eq. (3.3) recursively (see [95]) using the decay constants that were fitted to the data (see table 3.1). Fig. 3.6(a) shows the result of the maximum likelihood approach. Between 1 and 2 ms of detection time the errors converge to their minimum values. These values are maintained which is in contrast to the variable threshold approach in (b) where the minimum values are not maintained for $t_{\mathrm{det}} > 2$ ms.

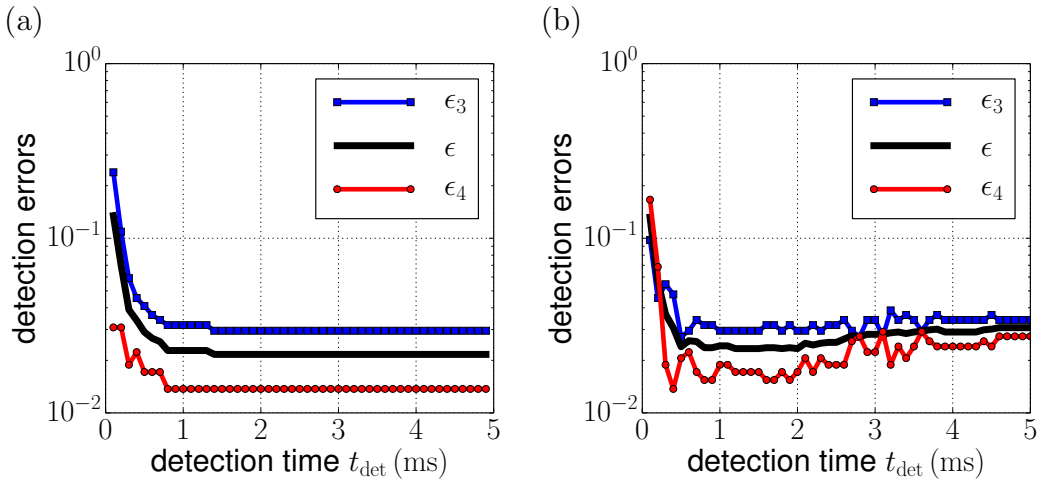

Figure 3.6: Comparison of state detection schemes with $t_{\mathrm{bin}} = 0.1\,\mathrm{ms}$. The state detection errors for atoms prepared in $F = 4$ (ϵ_4), $F = 3$ (ϵ_3) and the mean errors ϵ are plotted as functions of t_{det}. The maximum likelihood method is shown in (a); the variable cutoff results in (b) are the same as in Fig. 3.5. The statistical errors are smaller than 50% for all t_{det}.

Table 3.2 shows a comparison of the minimum time averaged errors the two methods produce. Atoms that have been prepared in $F = 4$ ($\overline{\epsilon_4}$) are significantly better detected with the maximum likelihood approach. Comparing the errors for atoms that have been prepared in $F = 3$ ($\overline{\epsilon_3}$), the methods are equivalent within the considered region. The reason for this is that our analysis cannot discriminate between preparation and detection errors. The preparation error for $F = 3$ is significantly higher than for $F = 4$ (see also Fig. 3.6), because here, for technical reasons, a σ^--polarized optical pumping beam resonant with $F = 4 \rightarrow F' = 4$ (level scheme: see Fig. 3.1) has been used. Under this configuration $|F = 4, m_F = -4\rangle$ is a dark state leading to inefficient $F = 3$-pumping. Therefore the shown detection data is limited by state preparation in the case of ϵ_3.

In conclusion we will use the maximum likelihood method for evaluating the data in the following section 4.2, because – compared to the variable threshold method – it is largely independent of the detection time and results in lower detection errors. Doing so, for each data set we measure the histograms as shown in Fig. 3.3 and extract the decay constants τ as in Fig. 3.4.

3.5 Limits of the Cavity-Enhanced Detection Scheme

The fidelity of state detection inside the cavity is limited by the overlap of the dark and bright histograms $D[n, t_{\mathrm{bin}}]$ and $B[n, t_{\mathrm{bin}}]$. The main factors leading to this overlap are:

- The low overall photon collection efficiency of $t^2/(t^2 + a^2)\eta_{\mathrm{det}} \approx 5\%$ (see table 1.1).
- The SPCM dark count rate of $\approx 0.5\,\mathrm{kHz}$ contributing $\approx 25\%$ to the dark histogram.
- Radial oscillations (along the x-direction) and hopping along the cavity axis (z-direction) see Fig.3.3 (a) are increasing the mean value and the width of the dark histogram.

An optimization of these points would lead to an improvement of the detection fidelity within a detection time on the ms scale. For the current parameters this timescale is limited by the decay constants given in table 3.1. Using the maximum likelihood method (Eq. (3.3)) it is remarkable that the resulting absolute errors in table 3.2 change by less than 1% if the decay constants τ are varied by a factor of 5. Changes in the decay constants due to changes in the experimental settings (laser powers, B-fields, etc.) will therefore only slightly affect the state detection procedure. This robustness of Bayesian analysis techniques is also observed in [99]. Changes of the histograms, however, are significant. These changes happen on a daily basis, mainly due to changes in the cavity lock performance, which are leading to more or less intra-cavity atomic heating. This leads to significant changes of the dark histogram (see bullet point 3 above) and is reflected in a variation of the mean detection error ϵ on the few percent level.

4 Carrier-Free Raman Manipulation of Atoms in an Optical Cavity

For neutral atoms the conditions for robust Raman cooling, i.e. the presence of resolved motional sidebands of appropriate coupling strength, can be challenging to fulfill. This is particularly true for setups with restricted optical access and unconventional optical potentials, such as cavity QED systems [17, 20] or micro-array traps [100].

Here, I describe a scheme for the Raman manipulation of trapped neutral atoms that exhibits a strong suppression of the carrier transition in the driven two-photon transfer and show how it can benefit the Raman cooling limit. Furthermore, the technique is applied to perform two-dimensional ground-state cooling of atoms strongly coupled to the cavity and to investigate their heating rate.

4.1 Raman Laser Setup

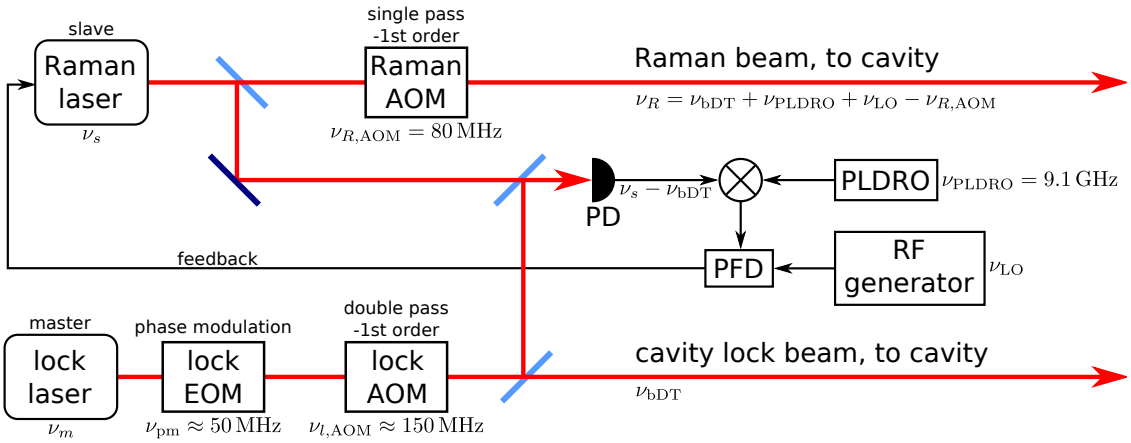

Figure 4.1: Simplified Raman setup. AOM ▶ acousto-optic modulator, PD ▶ photodiode, PLDRO ▶ phase-locked dielectric resonator oscillator, EOM ▶ electro-optic modulator. Note that the Raman beam is running single tone, since the phase frequency detector (PFD) cannot follow the fast phase modulation of the lock beam, which is needed for locking the cavity (cf. section1.4). The two-photon detuning is given with $\delta_{\mathrm{tp}} = 2\pi \cdot (\nu_R - \nu_{\mathrm{bDT}}) = \omega_R - \omega_{\mathrm{bDT}}$.

For the coherent transfer between the two cesium hyperfine ground states two laser sources with a frequency difference of about the hyperfine splitting ($\approx 9.2\,\mathrm{GHz}$) but stable with respect to each other on the scale of the effective ground-state width ($\lessapprox$ kHz) are needed. This is achieved with a fast and technically advanced optical phase-locked loop, described in [101–103]. The electronic and optical setup used for EIT measurements (see chapter 2) is described in [35], but two modifications have to be noted.

First, the former Raman laser (= slave laser) which was build in Littrow configuration is now exchanged by an interference filter laser (IFL) as described in section 1.3. This resulted in a better lock performance (more power in the carrier, higher lock bandwidth) and most importantly in a very high day-to-day stability.

Second, the laser is not locked to the MOT cooling laser as done for the EIT measurements, but stabilized to the lock laser (see section 1.4), since the intracavity standing-wave trap will be used as the second Raman arm. The Raman setup used for this work is shown in Fig. 4.1. Taking Raman spectra, the two-photon detuning δ_{tp} is adjusted by changing ν_{LO}.

4.2 Raman Sideband Transitions and Raman cooling

In this section we utilize the Raman laser setup from section 4.1 and the Bayesian method from chapter 3 to realize the manipulation of motional ground-state population and its non-destructive detection, respectively.

4.2.1 Geometrical Situation

In the experiments described here a single neutral cesium atoms is trapped inside the cavity using the techniques described in chapter 1. Fig. 4.2 shows the geometry of the optical potential, the orientation of the applied magnetic bias field of 1.0 Gauss and the position of additional laser fields.

In order to achieve coherent two-photon coupling between the $F = 3$ and $F = 4$ manifold (in the following: $|\downarrow\rangle = |F = 3, m_F = -3\rangle$, $|\uparrow\rangle = |F = 4, m_F = -4\rangle$) of the $6\,^2\mathrm{S}_{1/2}$ electronic ground state, we address the atom by a single Raman laser beam that propagates along the y-axis. This weak Raman light is phase-locked to the blue detuned strong dipole-trap light (845.5 nm) with a tunable frequency offset around the hyperfine splitting $\omega_R - \omega_{\mathrm{bDT}} \approx 2\pi \cdot 9.2\,\mathrm{GHz}$. For details on the technical realization of the phase lock see section 4.1.

The second field in the two-photon Raman coupling in our experiment is hence provided by the always present blue dipole-trap light [17], in contrast to the more common implementation via a second Raman beam [18–21]. The choice of blue detuned light, where atoms are confined around the intensity zeros of the trapping light, allows us to operate the optical trap at a detuning of $\Delta_{\mathrm{bDT}} \approx 2\pi \cdot 3\,\mathrm{THz}$ from the atomic resonance with minimal light shifts of atomic levels and low spontaneous

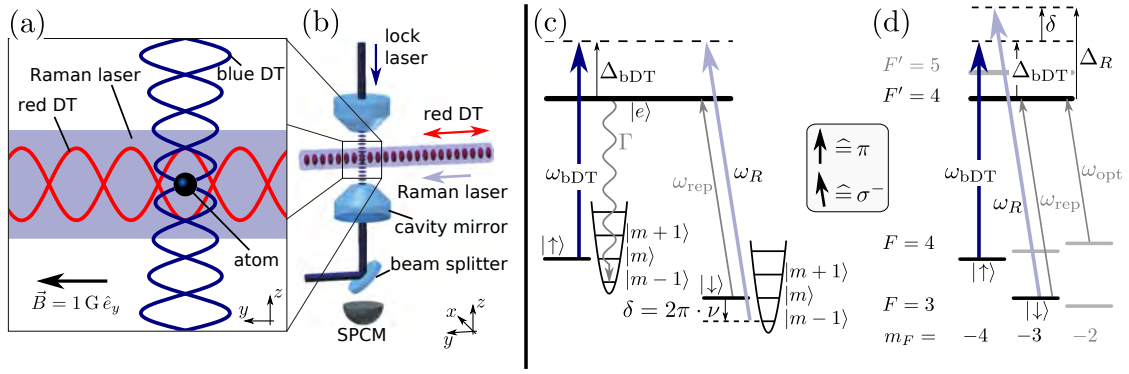

Figure 4.2: Experimental setup. (a) A single cesium atom is trapped in the optical lattice potential of the blue detuned and the red detuned standing-wave dipole trap (DT). (b) The atom is positioned inside an optical high-finesse Fabry-Pérot cavity. The resonantly enhanced cavity lock laser field acts as the blue detuned standing wave trap for the atoms. (c) Illustration of a Raman cooling cycle driven by the blue detuned dipole trap (ω_{bDT}) and the Raman laser (ω_R). (d) Details of the levels and transitions in ^{133}Cs involved in Raman manipulation and cooling. We define the two-photon detuning δ as the difference between the one-photon detunings: $\delta = \Delta_R - \Delta_{\mathrm{bDT}}$.

photon-scattering rates[1].

More importantly, however, the blue detuning provides the mechanism for the intrinsic suppression of the Raman carrier coupling that is central to the presented Raman scheme.

4.2.2 Motional State Coupling and Carrier Suppression

Intuitively the suppression of the carrier can be understood by considering the local Rabi frequency for a two-photon transition, $(\Omega_{\mathrm{bDT}}\Omega_R)/\Delta$, where Ω_{bDT}, Ω_R, and $\Delta \approx \Delta_{\mathrm{bDT}} \approx \Delta_R$ denote the local single-photon Rabi frequencies and detunings from resonance (cf. Fig. 4.2(d)). For atoms fixed at the intensity zero of the blue detuned trap light the single-photon Rabi frequency Ω_{bDT} and hence the local two-photon Rabi frequency will vanish.

Motional State Coupling

More formally, we take into account the external degree of freedom of the trapped atoms. The resonant couplings between the spin-motional states are described by

$$\Omega_{\uparrow m_y m_z, \downarrow m'_y m'_z} = \Omega_0 |\langle \uparrow m'_y m'_z | \sin[k_z \hat{z}]\, e^{i k_y \hat{y}}\, \hat{\sigma}^\dagger\, | \downarrow m_y m_z \rangle| \tag{4.1}$$

[1]This detuning also leads to a large beat length $d_{\mathrm{beat}} = \ell_0/3$ (see Eq. (1.1)) between the intracavity optical trap light and the probe light, which is beneficial for constant atom-cavity coupling and therefore leads to robust and high-fidelity state detection (see section 3.2).

where m_y, m_z, m'_y, m'_z denote the motional quantum numbers of the initial and the final state, $\hat{y}, \hat{z}$ are the position operators along the y- and z-axis and $k_y = 2\pi/\lambda_{\mathrm{rDT}}, k_z = 2\pi/\lambda_{\mathrm{bDT}}$ are the wave vectors of the red and blue detuned dipole trap fields. $\hat{\sigma}^\dagger = |\uparrow\rangle\langle\downarrow|$ represents the spin raising operator, and the bare two-photon Rabi frequency with an approximate experimental value of $\Omega_0 \approx 2\pi \cdot 0.3\,\mathrm{MHz}$ summarizes the dependency on laser powers, detuning and internal states.

In the Lamb-Dicke regime (see section 2.2) we can approximate the expression describing the geometry of the light fields in Eq. (4.1) and rewrite it in terms of harmonic oscillator raising $\hat{b}_z^\dagger, \hat{b}_y^\dagger$ and lowering operators $\hat{b}_z, \hat{b}_y$ as

$$\begin{aligned}\sin[k_z\hat{z}]\, e^{ik_y\hat{y}} &\approx (k_z\hat{z})\,(\hat{\mathbb{1}}_y + i\,k_y\hat{y}) \\ &= \eta_z(\hat{b}_z^\dagger + \hat{b}_z) + i\,\eta_y\eta_z(\hat{b}_z^\dagger\hat{b}_y^\dagger + \hat{b}_z\hat{b}_y^\dagger + \hat{b}_z^\dagger\hat{b}_y + \hat{b}_z\hat{b}_y).\end{aligned} \tag{4.2}$$

Here, η_y and η_z denote the Lamb-Dicke factors along the y- and z-direction with experimental values of about 0.1. Eq. (4.2) prescribes the selection rule $\Delta m_z = \pm 1$ for the standing wave Raman field configuration[2], i.e. carrier transitions with $\Delta m_z = 0$ are suppressed. The first order sidebands of the motion along the z-axis scale with $\Omega_0\eta_z$ and the sidebands coupling the motion along the y- and z-axis scale with $\Omega_0\eta_y\eta_z$.

Limits to Carrier Suppression

Theoretically and according to Eq. (4.2) full carrier suppression for atoms sitting in the perfect zero-crossing of the electric field amplitude of one of the Raman lasers is expected. Since this blue detuned Raman laser light is also a source of atomic confinement, atoms will localize close to the minimum of the light intensity. However, offset Raman light intensity at the trap minimum, for example due to the imperfect intensity balance of the two interfering beams forming an optical standing wave, will give rise to a residual carrier Raman coupling. In addition, external forces displacing the trap center from the intensity minimum can lead to a further increase of the carrier contribution.

In order to quantify these effects for our system we define the suppression factor

$$\mathcal{S} = \frac{\Omega_{\uparrow m_y m_z=0,\downarrow m_y m'_z=1}}{\Omega_{\uparrow m_y m_z,\downarrow m_y m_z}}\frac{1}{\eta_z} \tag{4.3}$$

as the ratio of the ground-state heating-sideband Rabi frequency to the carrier Rabi frequency along the z-axis, which we normalize by the Lamb-Dicke factor. Thus, in the Lamb-Dicke regime Eq. (4.3) yields $\mathcal{S} = 1$ for an atom addressed by two running wave Raman lasers and $\mathcal{S} \to \infty$ for perfect carrier suppression.

[2] In the Lamb-Dicke regime (see Eq. (2.7)) the approximation in Eq. (4.2) is valid and higher order sidebands do not need to be considered. Without this approximation the symmetry of the standing wave Raman field imposes the selection rule $\Delta m_z = \pm 1, \pm 3, \pm 5, ...$

If we assume that the Raman standing wave is formed by counter-propagating beams with an intensity ratio $\mathcal{R} \leq 1$, we obtain at the position of the atom the expression

$$\begin{aligned} e^{ik_z\hat{z}} - \sqrt{\mathcal{R}}\, e^{-ik_z\hat{z}} &= (1-\sqrt{\mathcal{R}})\, e^{ik_z\hat{z}} + 2i\sqrt{\mathcal{R}}\, \sin[k_z\hat{z}] \\ &\approx (1-\sqrt{\mathcal{R}})\hat{\mathbb{1}}_z + i(1+\sqrt{\mathcal{R}})\, \eta_z(\hat{b}_z^\dagger + \hat{b}_z) \end{aligned} \tag{4.4}$$

for the motional coupling along the z-axis in analogy to Eq. (4.2). The suppression factor is then given by $\mathcal{S} = \frac{1+\sqrt{\mathcal{R}}}{1-\sqrt{\mathcal{R}}}$. Our cavity with high reflectivity mirrors ($r^2 = \mathcal{R} \approx 1$, cf. table 1.1) has a finesse of $\mathcal{F} = \frac{\pi\sqrt{\mathcal{R}}}{1-\mathcal{R}} \approx 10^6$ and we therefore expect the carrier suppression to be limited at the $\mathcal{S} \approx \frac{4}{1-\mathcal{R}} \approx \frac{4\mathcal{F}}{\pi} \approx 10^6$ level due to the "running wave" component of the cavity mode.

A more stringent limit, however, is caused by gravitational acceleration g in the vertically orientated optical lattice with trap frequency ν_z. At a vertical position shift of $z_s = g/(2\pi\nu_z)^2 \approx 6\,\mathrm{pm}$ the atom experiences a field proportional to $\sin[k_z z]$, which can be Taylor expanded around the point $z = z_s$ and leads to a motional state coupling of

$$\begin{aligned} \sin[k_z\hat{z}] &\approx \sin[k_z z_s]\hat{\mathbb{1}}_{\tilde{z}} + \cos[k_z z_s]\; k_z\hat{\tilde{z}} \\ &= \sin[k_z z_s]\hat{\mathbb{1}}_{\tilde{z}} + \cos[k_z z_s]\, \eta_z(\hat{b}_{\tilde{z}}^\dagger + \hat{b}_{\tilde{z}}), \end{aligned} \tag{4.5}$$

where $\tilde{z} = z - z_s$. The gravitational sag therefore limits the suppression to $\mathcal{S} = \cos[k_z z_s]/\sin[k_z z_s] \approx 1/(k_z z_s) \approx 2 \times 10^4$.

4.2.3 2D Temperature Model

The expected relative height of the heating and cooling motional sidebands, which is a robust measure of atomic temperatures for 1D motional dynamics [75], also stays a robust measure for sidebands coupling motion in two dimensions.

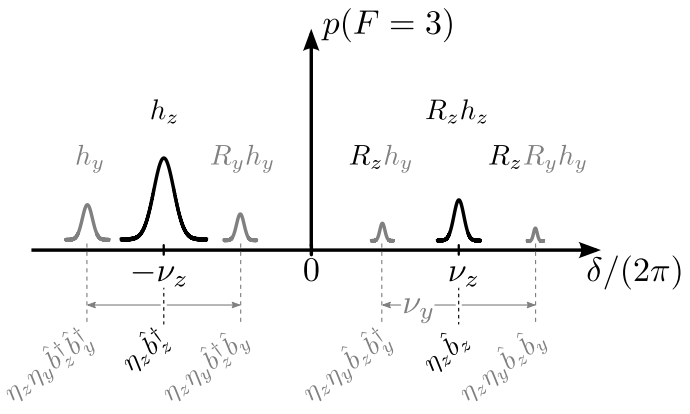

Figure 4.3: The relative heights of motional sidebands in the two-photon spectrum as a function of the atomic temperatures along both trap axes. For fitting the measured data the heights h_z and h_y will be assumed to be free parameters. See text for details.

To show this, two independent Boltzmann-distributions are assumed for the level populations of motional states m_i along the y- and z-axis

$$p_{m_i} = \frac{1}{\overline{m}_i + 1} \left(\frac{\overline{m}_i}{\overline{m}_i + 1} \right)^{m_i}, \qquad i = y, z. \tag{4.6}$$

The transfer probability of an atom initially prepared in $|\uparrow\rangle$ to the opposite spin state $|\downarrow\rangle$ after applying a Raman pulse of duration t is given by

$$p[t] = \sum_{m_y=0}^{\infty} \sum_{m_z=0}^{\infty} p_{m_y} p_{m_z} \sin^2[\Omega_{\uparrow m_y m_z, \downarrow m'_y m'_z}\, t/2]. \tag{4.7}$$

We determine the ratio R_z of the transition probabilities on the z-axis cooling ($\hat{b}_z$) and heating ($\hat{b}_z^\dagger$) motional sideband according to [75]

$$\begin{aligned} R_z &= \frac{\sum_{m_y=0}^{\infty} \sum_{m_z=1}^{\infty} p_{m_y} p_{m_z} \sin^2[\Omega_{\uparrow m_y m_z, \downarrow m_y m_z - 1}\, t/2]}{\sum_{m_y=0}^{\infty} \sum_{m_z=0}^{\infty} p_{m_y} p_{m_z} \sin^2[\Omega_{\uparrow m_y m_z, \downarrow m_y m_z + 1}\, t/2]} \\ &= \frac{\sum_{m_y=0}^{\infty} \sum_{m_z=0}^{\infty} p_{m_y} p_{m_z+1} \sin^2[\Omega_{\uparrow m_y m_z + 1, \downarrow m_y m_z}\, t/2]}{\sum_{m_y=0}^{\infty} \sum_{m_z=0}^{\infty} p_{m_y} p_{m_z} \sin^2[\Omega_{\uparrow m_y m_z, \downarrow m_y m_z + 1}\, t/2]} \\ &= \frac{\overline{m}_z}{\overline{m}_z + 1}, \end{aligned} \tag{4.8}$$

where we have used $\Omega_{\uparrow m_y m_z, \downarrow m'_y m'_z} = \Omega_{\uparrow m'_y m'_z, \downarrow m_y m_z}$ and $p_{m_i+1} = \frac{\overline{m}_i}{\overline{m}_i + 1} p_{m_i}$ in the last step.

Analog calculations yield the ratio of transitions involving the decrease and transitions involving the increase of one motional quantum along the y-axis

$$R_y = \frac{\overline{m}_y}{\overline{m}_y + 1}, \tag{4.9}$$

and they result in the relative scaling of all sidebands summarized in Fig. 4.3. The height factors h_y, h_z depend on the experimental details of the chosen Rabi spectroscopy pulse and do not play a role in the determination of the mean excitation numbers

$$\overline{m}_y = \frac{R_y}{1 - R_y} \quad \text{and} \quad \overline{m}_z = \frac{R_z}{1 - R_z}, \tag{4.10}$$

which are connected to the temperature by Eq. (1.21).

This analysis rigorously only applies to resolved sidebands. For the temperature estimation with degenerate sidebands we will estimate an upper limit for the individual mean excitation numbers $\overline{m}_y^{(\max)}$ and $\overline{m}_z^{(\max)}$ by attributing the height of the cooling sideband in its entirety to each motional axis.

4.2.4 Sideband Spectroscopy and Cooling

We start our experimental investigation by mapping out the two-photon spectrum of an atom trapped in the crossed standing-wave potentials to localize and identify accessible Raman transitions. After a successful single atom loading event, the measurement sequence initializes the atom with high fidelity in the state $|\uparrow\rangle$ by a 5 ms long optical pumping pulse of repump (ω_{rep}) and optical pump (ω_{opt}) light. These two beams are σ^--polarized and resonant with the $F = 3 \rightarrow F' = 4$ and the $F = 4 \rightarrow F' = 4$ of the D_2-line, respectively (see Fig. 4.2(d)). A single Raman

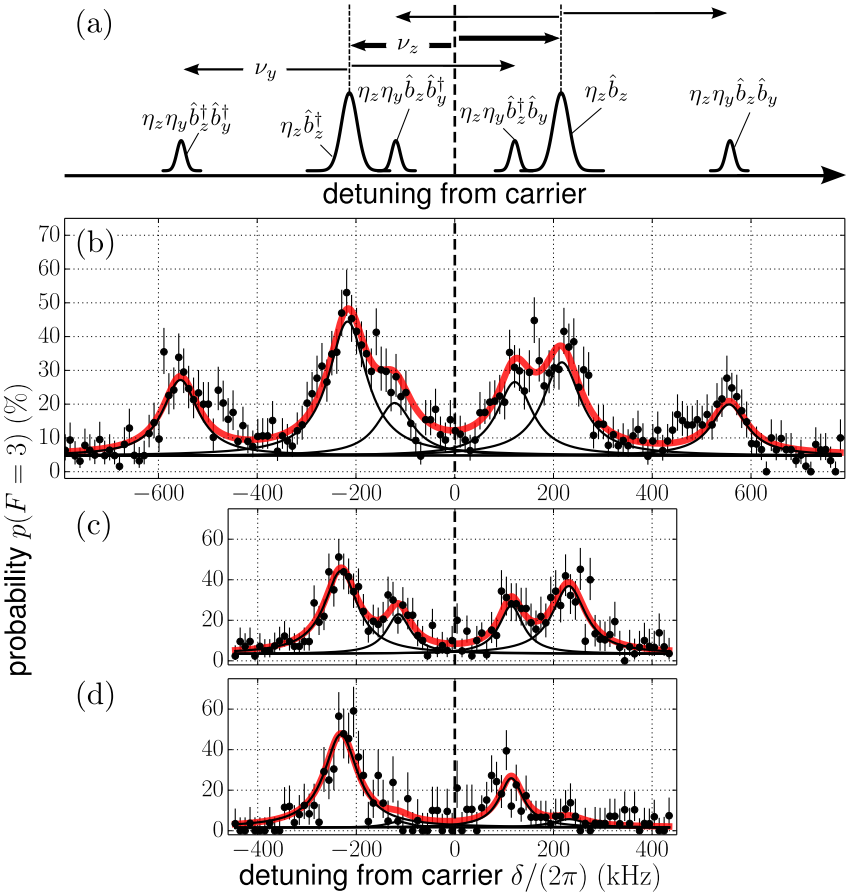

Figure 4.4: Raman spectra with carrier suppression. (a) Illustration of the transitions allowed by the Raman field geometry (cf. Eq. (4.2)). (b) Complete Raman spectrum after cavity cooling. Error bars indicate one standard deviation uncertainty intervals resulting from a total of about 60 state detections per data point. (c) Motional sideband spectra of single atoms after cavity-cooling with $\overline{m}_z = 4.5 \pm 2.4$ and (d) after Raman sideband cooling on the (cavity) z-axis cooling sideband with $\overline{m}_z = 0.10 \pm 0.01$ strongly reducing the sidebands corresponding to $\hat{b}_z$ transitions. The significant presence of the $\hat{b}_z^\dagger\hat{b}_y$ sideband shows that the cooling into the motional ground state along the z-axis does not effectively cool the motion along the y-axis.

laser pulse of 1 ms duration and about 1 mW power (waist radius 60 μm) is applied to the atom and followed by cavity-assisted readout of the hyperfine state of the atom, see chapter 3. The fast and non-destructive state detection also provides cavity-cooling and allows us to repeat the 70 ms long interrogation sequence up to 100 times (see Fig. 3.2) with the same atom, after which a new atom is loaded.

The results of our measurement, shown in Fig. 4.4(b), clearly reveal a strong suppression of the carrier transition in the two-photon spectrum. Within the signal-to-noise limits of our data we do not find a discernible carrier contribution, in agreement with the theoretically estimated suppression of the carrier Rabi frequency by a factor $> 10^4$ limited by gravitation sag, cf. subsection 4.2.2. A fit of six Lorentzian curves to the motional sidebands spectrum provides an estimate for the trapping frequencies along the y- and z-axis. By comparing the relative heights of the heating and cooling motional sidebands we furthermore extract the temperatures of the atoms (see subsection 4.2.3). The spectral data shown in Fig. 4.4(c) for cavity-cooled atoms (see subsection 2.1.1) yield a mean excitation number of $\overline{m}_z = 4.5 \pm 2.4$ quanta along the z-direction.

Next, we implement one-dimensional Raman cooling along the cavity direction. During a 20 ms long cooling interval we simultaneously drive the resolved $\hat{b}_z$ cooling sideband (see Fig. 4.4(a)) and apply the optical pumping and repumping light (see Fig. 4.2(c) and(d)). The cooling stage is followed by the recording of a Raman spectrum for temperature determination (Fig. 4.4(d)). We extract steady-state motional excitations $\overline{m}_y = 3.2 \pm 0.2$ and $\overline{m}_z = 0.10 \pm 0.01$ after Raman cooling.

In order to characterize how the cooling process of atoms is influenced by the suppression of the Raman carrier transition, we estimate its fundamental cooling limit [75,104]. For simplicity we only consider one spatial dimension in the following analysis. During a resolved sideband cooling cycle the atom is driven on the cooling sideband ($\delta = 2\pi \cdot \nu$) from the state $|\uparrow, m\rangle$ to $|\downarrow, m' = m - 1\rangle$. Resonant single photon excitation by the repumping light and spontaneous decay predominantly return the atom to the state $|\uparrow, m-1\rangle$ in the Lamb-Dicke regime (see Fig 4.2(c)). This pumping of the atom into the "dark" motional ground state $|\uparrow, 0\rangle$ is counteracted by heating due to off-resonant Raman excitation in the Lorentzian wing of the carrier and the blue sideband transition. For large ground-state occupations the cooling dynamics can be restricted to the ground and the first excited motional state and can be described by the rate equations [75]

$$\dot{p}_0 = p_1 \frac{(\eta\Omega_0)^2}{\Gamma_{\text{rep}}} - p_0 \left[\cancel{\left(\frac{\Omega_0}{4\pi\nu}\right)^2 \eta^2 \Gamma_{\text{rep}}} + \left(\frac{\eta\Omega_0}{8\pi\nu}\right)^2 \Gamma_{\text{rep}} \right] \tag{4.11}$$

and $\dot{p}_1 = -\dot{p}_0$, for the probabilities p_0, p_1 of the atom to be in the ground and the first excited state. The first term on the right hand side of Eq. (4.11) states the rate of the cooling cycle. Resonant Raman excitation on the red sideband is followed by repumping and decay on the carrier at a rate of Γ_{rep}. The second term, which contains the heating due to off-resonant excitation on the carrier followed by decay on the heating sideband, vanishes in our case due to the carrier suppression.

The leading heating mechanism is therefore given by off-resonant excitation on the heating sideband and repumping and decay on the carrier described in the third term. This results in a fundamental steady-state mean occupation number

$$\overline{m} \approx p_1 \approx \left(\frac{\Gamma_{\mathrm{rep}}}{2 \cdot 2\pi\nu}\right)^2 (\mathcal{X} + 1/4), \tag{4.12}$$

which is a factor of 5 smaller than for conventional Raman cooling (see Eq. (2.8)). However, we do not expect our measurements to explore this fundamental limit, due to the effects of technical heating during the cooling and spectroscopy sequence, as well as due to imperfections in the optical pumping. In addition to improving the cooling limit the carrier suppression should also somewhat relax the initial starting-temperature requirements for the onset of robust Raman cooling [18]. Due to the significant contribution from higher order motional sidebands at the border of the Lamb-Dicke regime this effect of carrier suppression will be very small.

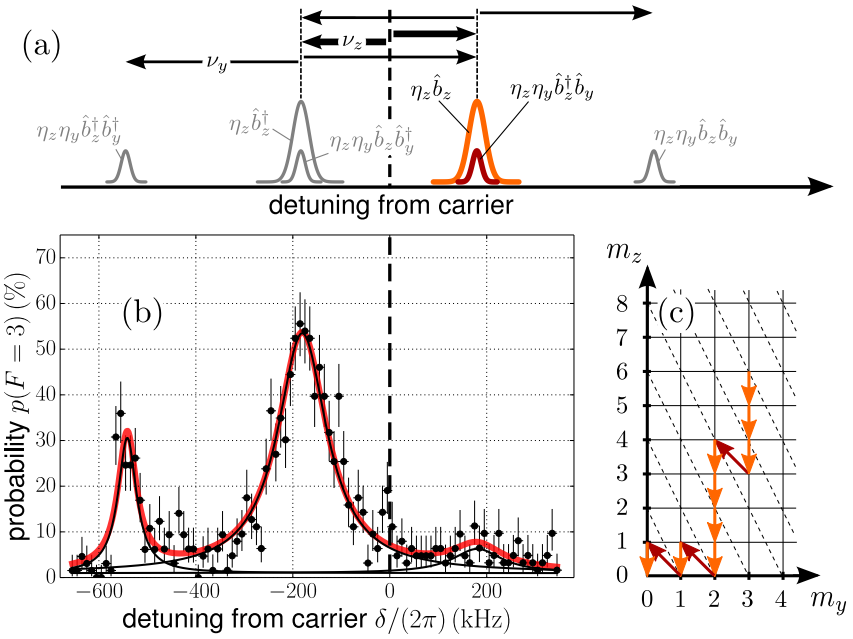

Figure 4.5: Continuous two-dimensional Raman cooling. (a) By adjusting the laser powers in the red and the blue dipole trap, the atomic trap frequencies along the y- and z-axis are matched such that $\nu_y = 2\nu_z$. By addressing the degenerate sidebands atoms are continuously cooled into the two-dimensional motional ground state. (b) The reduced heights of the degenerate $\hat{b}_z$ and $\hat{b}_z^\dagger\hat{b}_y$ sidebands in the Raman spectrum demonstrate successful ground-state cooling along both dimensions. (c) Schematic of an exemplary cooling trajectory. Dashed lines link points of equal motional energy of the atom.

In order to extend the Raman cooling from the cavity z-axis to the dipole trap y-axis one of the motional sidebands ($\hat{b}_z^\dagger\hat{b}_y$ or $\hat{b}_z\hat{b}_y$), which couple both directions, needs

to be addressed. Simultaneous cooling to the two-dimensional motional ground state is achieved in the experiment by adjusting the trapping frequencies to satisfy $\nu_y = 2\nu_z$. The two degenerate $\hat{b}_z^\dagger \hat{b}_y$ and $\hat{b}_z$ sidebands are addressed with a 20 ms long Raman, repump and optical pumping pulse and continuously cooled into the two-dimensional ground state (see Fig 4.5). From the height of the Raman sidebands after cooling we estimate upper limits for the mean excitation numbers of $\overline{m}_y^{(\max)} = 0.3 \pm 0.2$ and $\overline{m}_z^{(\max)} = 0.11 \pm 0.05$, respectively.

4.2.5 Intra-Cavity Heating Rate and Rabi Oscillations

Heating and position jumping of atoms in optical lattices formed by optical cavities have been noted in the past [65, 105]. Compared to standing wave potentials generated by counter-propagating running wave laser beams the resonantly enhanced dipole field inside Fabry-Pérot cavities is additionally affected by the noise of the cavity lock. Considering trap intensity fluctuations as the primary contribution (see also section 2.3), parametric heating in the approximately harmonic trap should lead to a linear increase of the heating rate with motional energy [38].

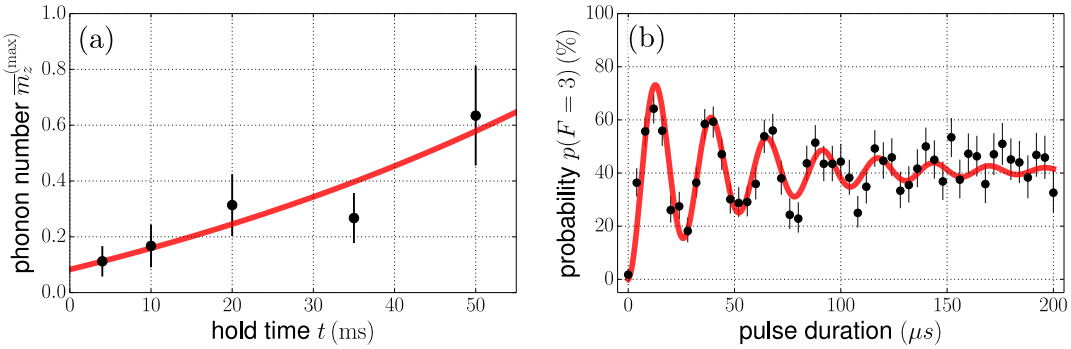

Figure 4.6: (a) Measurement of the heating rate along the z-axis (cavity) direction. The mean motional quantum number is recorded as a function of the hold time in the optical potential. The solid line fits the data with an exponential heating model (see text for details). (b) Coherent Rabi-oscillations on the z-axis motional sideband.

We directly measure the mean motional quantum number of single atoms $\overline{m}_z^{(\max)}[t]$ as a function of the hold time in the optical potential (see Fig. 4.6(a)). To account for the expected exponential increase in motional energy we fit the data with $\overline{m}_z^{(\max)}[t] = (\overline{m}_z^{(\max)}[t=0] + 1/2) \cdot \exp[\Gamma_H t] - 1/2$, which results in an initial maximum phonon number along the z-direction of $\overline{m}_z^{(\max)}[t=0] = 0.08 \pm 0.06$ and a heating-rate constant for low excitations of $\Gamma_H = (12 \pm 3)\,\mathrm{Hz}$. For these cold starting temperatures the low heating rate of less than one motional quantum in 50 ms allows atoms to remain well-localized during the timescales of most quantum optics experiments. Indeed, our experiment is in fact limited by spin relaxation due to spontaneous Raman scattering processes at the 100 ms timescale.

Finally we study coherent dynamics on the motional sideband. For this purpose an initial Raman cooling interval prepares the atom with high probability in the state $|\uparrow, m_z = 0, m_y = 0\rangle$. The excitation probability as a function of Raman pulse length on the $\hat{b}_z^\dagger$ heating sideband shows Rabi oscillation with a Rabi frequency of $2\pi \cdot (38.2 \pm 0.4)\,\mathrm{kHz}$ and a decay constant of $(55 \pm 7)\,\mu\mathrm{s}$ (see Fig. 4.6). Earlier measurements of carrier Rabi oscillations under similar experimental conditions but driven by microwave pulses have shown coherence times in excess of $100\,\mu\mathrm{s}$. We attribute the reduced coherence time to effects associated with the oscillation of the atom along the weakly confined x-direction. Since ν_z directly depends on the position along the x-direction, this motion strongly influences the sideband transitions.

4.3 Conclusion

With only one additional laser compared to a standard CQED-setup (see section 1.1) the Raman scheme is resource-efficient and – as demonstrated – can be applied to experiments with challenging optical access. The novel cooling method efficiently transfers atomic population into the 2D ground state on the few millisecond timescale, which enables high experimental repetition rates. In contrast to most cavity cooling schemes, where collective coupling to the cavity mode changes the cooling conditions (see subsection 2.1.3), it has the advantage of being readily applicable to more than one particle. Compared to other cooling experiments with additional Raman beams along the cavity direction, the presented scheme provides constant Raman coupling conditions for atoms at different axial positions inside the cavity.

5 Cavity-Modified Super- and Subradiant Rayleigh scattering

When more than one atom is placed into a cavity, the atomic dipoles radiate cooperatively into the cavity field. Simultaneously, this field acts back onto the atoms, providing a collective nonlinear interaction.

For large atomic ensembles super- and subradiant phenomena [23, 24] as well as cooling and self-organization [15, 25] have been observed in cavities. For instance, atoms can spatially order in such a way that cooperative emission maintains a strong cavity field: At some threshold the joint state of strong cavity field and ordered atom ensemble is energetically favorable compared to a non-ordered system in conjunction with a weak cavity field, and a phase transition occurs [106, 107], which was predicted by the famous Dicke model [27, 108].

With exactly two neutral atoms strongly coupled to a cavity field the experiments presented in this chapter realize the most elementary situation where both cooperative radiation and cavity backaction become relevant.

5.1 Experimental Setup

In the experiments described here exactly two neutral cesium atoms are trapped inside the cavity using the techniques presented in chapter 1. A sketch of the situation is provided by Fig. 5.1(a). The distances Δ_y and Δ_z are multiples of the respective lattice periodicities $\lambda_{\mathrm{rDT}}/2$ and $\lambda_{\mathrm{bDT}}/2$; for the trap geometry see Fig. 1.1. The relative phases of the driving laser field and the cavity-mode field at the atom positions are given by $\phi_{y,z} = 2\pi\Delta_{y,z}/\lambda_L = k_L\Delta_{y,z}$, where $\lambda_L = 852.3\,\mathrm{nm}$ is the driving laser wavelength and $k_L = 2\pi/\lambda_L$ the corresponding wave vector.

Due to a large beat length (see Eq. (1.1)) of $d_{\mathrm{beat}} = \ell_0/3$, the combined trapping potential confines the atoms close to the antinodes of the intra-cavity field. Therefore the atoms can only realize two patterns along the z-axis, which are described in table 5.1.

During the measurement three lasers are continuously turned on (see Fig. 5.1(b)): A strong repumping laser and a weak optical pumping laser (frequencies ω_{rep} and ω_{opt}) are shone in along the y-axis to keep most of the atomic population in the state $|F = 4, m_F = -4\rangle$. The co-propagating driving laser has a frequency $\omega_L = 2\pi c/\lambda_L$, an intensity $I_L \approx 2\,\mathrm{mW/cm^2}$, a detuning from the atoms $\Delta = \omega_L - \omega_0 \approx 2\pi \cdot 100\,\mathrm{MHz}$, and it is resonant with the cavity ($\delta = \omega_L - \omega_c = 0$). The detuning $\Delta \approx 2\pi \cdot 100\,\mathrm{MHz}$ is chosen to guarantee for good cavity cooling conditions, see

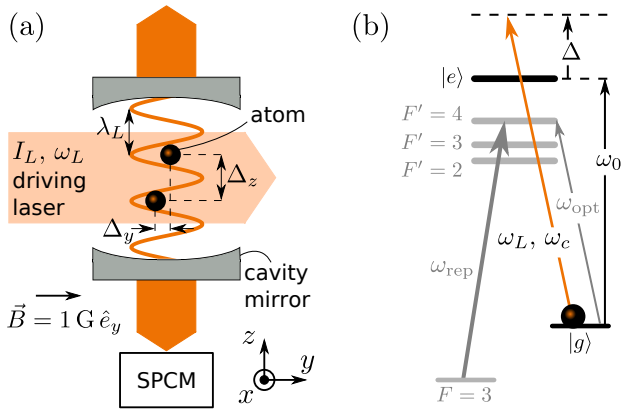

Figure 5.1: (a) Simplified experimental setup. A laser drives two trapped atoms (traps not shown) inside the cavity. The sine curve depicts the atom-cavity coupling strength along the z-axis. The single photon counting module (SPCM) detects the photons leaking through the lower cavity mirror. For two atoms inside the cavity, the measured count rate depends on the relative spacings Δ_y and Δ_z. (b) Atomic level scheme with the relevant lasers, their frequencies and the ^{133}Cs D_2-line transitions with $|g\rangle \equiv |F = 4, m_F = -4\rangle$ and $|e\rangle \equiv |F' = 5, m_F = -5\rangle$. All shown lasers are σ^--polarized. The cavity mode is $(\sigma^+ + \sigma^-)/\sqrt{2}$-polarized (see table 1.1).

subsection 2.1.2. Due to its large detuning, the laser light scatters off the atoms into the cavity mode predominately by Rayleigh scattering. The cavity output is detected by the SPCM.

	relative distance Δ_z	relative phase ϕ_z
λ-pattern	$n \cdot \lambda_L$	0
$\lambda/2$-pattern	$(n + 1/2) \cdot \lambda_L$	π

Table 5.1: Possible atomic patterns [109] along the cavity axis. These patterns are the only two configurations two atoms can realize along the cavity axis for our measurement setup. The factor n in an integer.

Fig. 5.2 shows an instructive measurement trace, selected to demonstrate the difference between two, one and zero atoms. In region (*i*), where two driven atoms couple to the cavity, the photon count rate jumps between a high ($\approx 12\,\mathrm{ms}^{-1}$) and a low ($\approx 2\,\mathrm{ms}^{-1}$) value. The high (low) photon count rates are interpreted as the atoms arranging in a pattern along the z-axis in which the scattered photons interfere constructively (destructively), leading to superradiant (subradiant) emission into the cavity mode. Around 1.7 s one of the two atoms is lost from the combined trapping potential, and a photon count rate with little variance and a mean of about $9\,\mathrm{ms}^{-1}$ in region (*ii*) is detected. Naively one would expect that two atoms,

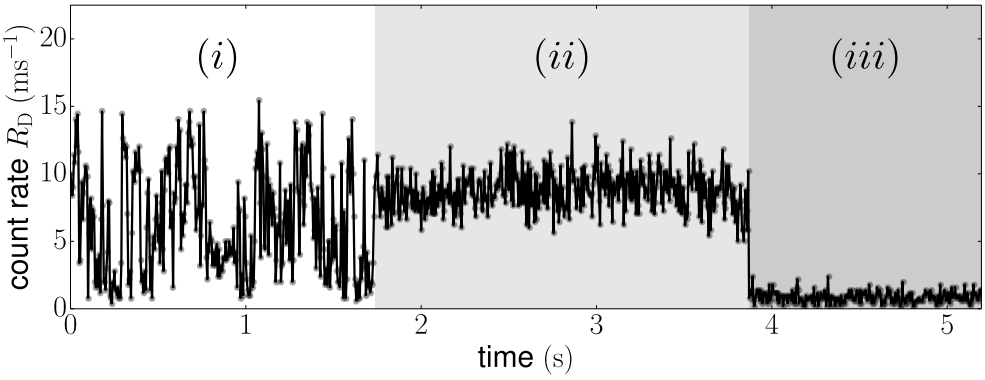

Figure 5.2: SPCM signal (single measurement trace) of driven atoms coupled to the cavity. In region (*i*), (*ii*), (*iii*) two, one and zero atoms are inside the cavity. The bin time is 5 ms.

which interfere constructively, emit four times as much photons as a single atom. This is clearly not the case and explained below in subsection 5.2.3 by the cavity backaction. From 3.9 s on (region (*iii*)), the cavity is empty and only background counts are measured.

5.2 Classical Description of Driven Atoms Inside a Cavity

Driven atoms coupled to a cavity are well described by the Jaynes-Cummings model, one of the toy models of quantum mechanics [1]. However, describing a system in classical terms, even though it is elegantly described by quantum theory, can offer benefits. Often classical pictures are more intuitively understood than quantum mechanical ones and help to develop new ideas which might not be easily developed using an abstract theory.

Here we describe a fully classical theory of radiating dipoles (= classical atoms) inside a classical cavity (= non-quantized cavity field). We recapitulate the main results of an instructive paper by the Vuletić group [26] and adapt them to our situation.

5.2.1 Driving One Atom Inside a Cavity

A classical atom is a polarizable particle with a complex polarizability [110]

$$\alpha = 6\pi\epsilon_0 c^3 \frac{\Gamma/\omega_0^2}{\omega_0^2 - \omega_L^2 - i(\omega_L^3/\omega_0^3)\Gamma} \overset{\text{RWA}}{\approx} \frac{6\pi\epsilon_0 c^3}{\omega_L^3}\mathcal{L}[\Delta], \tag{5.1}$$

with Γ as the dipole damping constant (see table 1.1). Using the rotating wave approximation (RWA) with $\Delta = \omega_L - \omega_0 \ll \omega_0$, implying $\omega_0^2 - \omega_L^2 \approx 2\omega_L(\omega_0 - \omega_L)$,

Parameter	Formula	Value
Cavity mode waist	$w_{0,\mathcal{M}} = w_{0,c}$	$23\,\mu$m
Round-trip time	$\tau = 2\ell_0/c$	1.0 ps
Cavity mode volume	$V = \pi w_{0,\mathcal{M}}^2 \ell_0/4$	$64 \times 10^3\,\mu\text{m}^3$
Max. coupling strength	$g_{\max} = \sqrt{3\pi\Gamma c/(2k_L^2 V)} = \sqrt{2}g_0$	$2\pi \cdot 18$ MHz
Cooperativity	$C = g^2/(\kappa\Gamma)$	30 to 50

Table 5.2: Relations that allow the development of intuitive classical formulas describing driven atoms inside a cavity. The definitions of our system parameters (ℓ_0, Γ, $\omega_{0,c}$, g_0) are found in table 1.1. The cooperativity is calculated for typical experimental values of the atom-cavity coupling strength g as determined below in subsection 5.3.2.

leads to the atomic line fucntion $\mathcal{L}[\Delta] = (-2\Delta\Gamma + i\Gamma^2)/(\Gamma^2 + 4\Delta^2)$.

We drive the atom with a laser beam of Gaussian peak intensity I_L and waist w_L. The atomic dipole scatters an electric field $E_\mathcal{M}$ into a specific spatial Gaussian mode $\mathcal{M}$ [26]:

$$E_\mathcal{M} = i\frac{g}{g_{\max}}\frac{6\mathcal{L}[\Delta]}{k_L^2 w_{0,\mathcal{M}}^2}E_L = i\frac{g}{g_{\max}}\beta E_L, \tag{5.2}$$

where a phase factor i accounts for the emission phase of the dipole into $\mathcal{M}$. The electric fields E are connected to the Gaussian peak intensities by $I = 1/2 \cdot \epsilon_0 c|E|^2$ and to the respective powers by $P = 1/2 \cdot \pi I w^2$. It is assumed that the Gaussian mode $\mathcal{M}$ with waist $w_{0,\mathcal{M}}$ is not too tightly focused $w_{0,\mathcal{M}} \gg \lambda_L$, which is fulfilled for our experiments. The scaling factor $g/g_{\max}$ with $g \leq g_{\max}$ takes into account that the dipole does not need to be situated in the center of $\mathcal{M}$. Note that the classical model describes pure Rayleigh scattering, because the dipole emits at its driving frequency ω_L.

With the knowledge of Eq. (5.2) we can address the problem of one driven atom which scatters into the mode $\mathcal{M}$ of a cavity and is trapped at an antinode of the intra-cavity field (see Fig. 5.1 but with only one atom). The only, but significant difference to the free space problem is the enclosure of $\mathcal{M}$ by two mirrors. In steady state, the field inside the cavity E_c has to reproduce itself after one round trip [26]:

$$E_c = 2E_\mathcal{M} + r^2 \exp[2ik_L\ell_0]E_c. \tag{5.3}$$

Within a round trip the atom scatters bidirectionally into the cavity mode $\mathcal{M}$ with field amplitude $E_\mathcal{M}$, while the cavity field accumulates a phase of $2k_L\ell_0$ and is reflected from the two mirrors with field reflectivity r. The values of all relevant parameters for our system are listed in table 1.1.

The atom is simultaneously driven by the driving laser field E_L and the intra-

Quantity	Formula	Unit
intra-cavity photon number	$n_p = 2\epsilon_0 \lvert E_c\rvert^2 V/(\hbar\omega_L)$	—
output power after one cavity mirror	$P_{\text{out}} = \frac{1}{4}\pi\epsilon_0 c w_{0,\mathcal{M}}^2 t^2 \lvert E_c\rvert^2$	W
count rate on SPCM	$R_{\text{D}} = \eta_{\text{oa}}\kappa n_p = \eta_{\text{det}} P_{\text{out}}/(\hbar\omega_L)$	1/ s

Table 5.3: Formulas relating typical measurement quantities to the classical equations established above. All quantities are directly proportional to each other. The values of our system parameters are found in tables 1.1 and 5.2. The overall detection efficiency η_{oa} is defined by Eq. (1.2)

cavity standing wave $2E_c$. With Eq. (5.2) one finds

$$E_{\mathcal{M}} = i\frac{g}{g_{\max}}\beta\left(E_L + \frac{g}{g_{\max}}2E_c\right). \tag{5.4}$$

The prefactor $g/g_{\max}$ is scaling the intra-cavity field twice: If for example the dipole is not centered in the cavity mode it first gets less excited by the intra-cavity field and than also scatters less light into $\mathcal{M}$ with the same argument as for the driving field E_L. Experimentally, the coupling g to the cavity can additionally be reduced due to the cavity mode polarization. The maximum possible coupling $g_{\max}$ for our system is given in table 5.2.

For a more intuitive understanding we use table 5.2 and rewrite Eq. (5.4) as

$$E_{\mathcal{M}} = i\frac{\mathcal{L}[\Delta]}{2}\cdot\left(\frac{g_{\max}}{\Gamma}\cdot E_L + \frac{g}{\Gamma}\cdot 2E_c\right)\cdot g\tau, \tag{5.5}$$

Now an interpretation of the involved factors is possible: The spatially homogeneous driving laser field polarizes the atoms addressing the strongest dipole transition and is therefore weighted with the maximal coupling rate $g_{\max}$. The polarization of the atoms induced by the cavity field scales with the reduced coupling rate g. Both terms are divided by the atomic damping rate Γ. The last factor in Eq. (5.5) is interpreted as the polarized atoms acting back onto the cavity field with the coupling rate g within one round-trip time τ.

We insert Eq. (5.5) into Eq. (5.3) and solve for the cavity field

$$E_c = -\frac{E_L}{2}\frac{g_{\max}}{g}\frac{1}{\frac{i}{2C\mathcal{L}[\Delta]} + \frac{\delta}{2\kappa C\mathcal{L}[\Delta]} + 1}, \tag{5.6}$$

where we introduce the cooperativity $C = g^2/(\kappa\Gamma)$, as one of the figures of merit in coupled atom-cavity systems, and approximate $r^2\exp[2ik_L\ell_0] = r^2\exp[2\pi i(\delta + \omega_c)/\omega_{\text{FSR}}] = r^2\exp[2\pi i\delta/\omega_{\text{FSR}}] \approx r^2 + 2i\delta r^2\ell_0/c$, using $\delta = \omega_L - \omega_c \ll \omega_{\text{FSR}} = \pi c/\ell_0$, and further as $r^2 + i\delta(1-r^2)/\kappa$, using that $\kappa = (1-r^2)/\tau$ for $r \approx 1$.

Table 5.3 relates Eq. (5.6) to typical measurement quantities, such as the SPCM count rate R_{D}.

Variation of g

Pumping the cavity on resonance, an increase of the atom-cavity coupling g leads to a decrease in the cavity-output power [34]. This effect is intuitively explained by the increasing distance between the normal modes of the system as g increases: Staying resonant with the cavity the singly excited dressed states are less and less populated and the intra-cavity photon number n_p and the count rate R_D decrease.

Driving the atom from the side one might expect that the situation is reversed and more light is scattered into the cavity mode due to a Purcell-like enhancement [111, 112].

Therefore, aiming at a high singal-to-noise ratio, it seems reasonable to maximize R_D by increasing g. Fig. 5.3 shows that this strategy does not lead to a higher count rate for our system parameters.

The power emitted into the cavity vanishes for the two limiting cases $g \to 0$ and $g \to \infty$. This behavior is studied and explained quantum mechanically in [113] and is also shown to hold in the strong driving limit, where the classical description would become invalid, since atomic saturation effects are not included[1].

Staying well in the weak atomic saturation limit, it is instructive to study the classical amplitude of the driven dipole. The amplitude of the electric field emitted by the dipole is imprinted in $E_\mathcal{M}$ in Eq. (5.5). The normalized amplitude of the driven dipole in steady state is defined as

$$a_\mathrm{dipole} = \left| \frac{E_\mathcal{M}}{E_L} \cdot \frac{1}{\frac{1}{2} \cdot \frac{g_\mathrm{max}}{\Gamma} \cdot g\tau} \right| . \tag{5.7}$$

It is normalized to the driving field strength E_L and therefore equals 1 for a resonantly driven dipole in free space. Within the Lorentz model this amplitude can be viewed as proportional to the displacement of the electron from its equilibrium position [114].

Fig. 5.3 shows that the dipole amplitude strongly depends on g. For $g \to 0$ the free space situation ($g \ll \kappa, \Gamma$) is recovered. The dipole oscillates with maximum amplitude but no light is emitted into the cavity mode $\mathcal{M}$ since the effective atom-cavity coupling is 0. As g and thereby C increase two effects set in.

On the one hand the increasing Purcell factor $2C$ directs the scattered light more and more into $\mathcal{M}$. For $g \to \infty$ all the scattered light is directed into the cavity. More quantitatively the count rate and the dipole amplitude are connected by $R_\mathrm{D} \propto a^2_\mathrm{dipole} \cdot 2C \cdot \kappa^2/(\delta^2 + \kappa^2)$.

On the other hand – since the dipole sits in an antinode of the intra-cavity field – the light that is scattered into the cavity and reflected from the cavity mirrors is exactly π out of phase with the driving field. Thus driving field and intra-cavity field more and more destructively interfere as g grows, leading to a smaller effective dipole drive, due to cavity backaction.

[1] Section 5.5 explains the limits of the classical theory.

Combination both effects an increase in g leads to an absolute increase of R_D due to the Purcell-like enhancement, until a_dipole gets so small that R_D starts to decrease again.

The blue region in Fig. 5.3 marks typical values of C that are experimentally realized within this chapter and correspond to atom-cavity coupling magnitudes g in an interval between 8 and 10 MHz. For our system the expected SPCM count rate R_D therefore becomes smaller as the coupling strength increases within this interval.

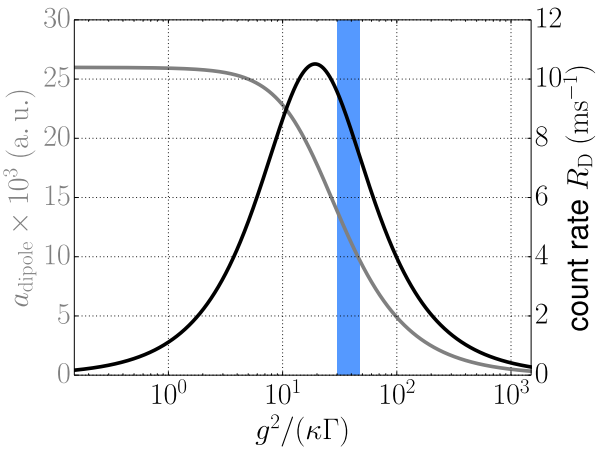

Figure 5.3: Transversal driving of a single dipole inside the cavity. The variation of $C = g^2/(\kappa\Gamma)$ by scanning g and its impact on the SPCM count rate R_D (black) and the dipole amplitude a_dipole (gray) are shown. Our typical experimental C values are marked in blue. Plot parameters from section 5.1.

5.2.2 Driving N Atoms Inside a Cavity

The classical approach for one driven atom inside the cavity can be generalized to N driven atoms that sit at arbitrary positions along the cavity (z-axis) and along the driving beam (y-axis) [26].

The position z_n of atom n effects its coupling to the standing wave cavity field. This is subsumed in the effective coupling strength per atom for the cavity

$$\mathcal{H} = \frac{1}{N}\sum_{n=1}^{N} \cos^2[k_L z_n]. \tag{5.8}$$

Furthermore the atoms scatter photons from the driving field into the cavity mode. To describe this process the relative phases along the driving laser and along the cavity axis matter and are included in the collective coupling strength per atom for the driving beam:

$$\mathcal{G} = \frac{1}{N}\sum_{j=n}^{N} \exp[ik_L y_n]\cos[k_L z_n]. \tag{5.9}$$

Here we have assumed that the atoms are still close to the maximum of the Gaussian cavity mode, even though they can be at different y-positions. The parameter $\mathcal{G}$

explains the role of the two atomic patterns, which were already mentioned in section 5.1. Along both axis (y, z), the two most interesting cases are realized for, first, an inter-atomic spacing that is an integer multiple of λ_L, and second a spacing of odd integer multiples of $\lambda_L/2$.

Exciting the atoms with the transversal driving laser, both the magnitude and the phase of the atom-cavity coupling matter: In the first case ($\mathcal{G} = \mathcal{H} = 1$) superradiant emission into the cavity mode $\mathcal{M}$ is measured [23, 106, 107], while in the second case ($\mathcal{G} = 0$, $\mathcal{H} = 1$) a subradiant state with no emission into $\mathcal{M}$ is formed. In contrast to this, for the excitation of atoms by the cavity field, only the magnitude of the atom-cavity coupling is important and super- and subradiant emission is not expected.

For an intuitive explanation we assume – as it is the case in our experiments – that two atoms sit at maximum coupling in an antinode of the intra-cavity field. The phase $\varphi_z^{(n)}$ at each of the two atom positions can be either 0 or π, both leading to $\mathcal{H} = 1$.

Therefore the relative phase $\phi_z = |\varphi_z^{(1)} - \varphi_z^{(2)}|$ along the cavity axis does not matter if the cavity is pumped. In a test experiment we coupled two atoms strongly to the cavity and pumped the cavity instead of the atoms. In contrast to the strong photon-count fluctuations observed in Fig. 5.2(i), here a signal showing little variance was measured.

If, however, the atoms are driven from the side and emit into the cavity, the collective coupling parameter for the driving beam $\mathcal{G}$ additionally enters the dynamics. Assuming $\varphi_y = 0$ for both atoms we get $\mathcal{G} = 1/2(1 \cdot \cos[\varphi_z^{(1)}] + 1 \cdot \cos[\varphi_z^{(2)}])$, leading to a net coupling of $\mathcal{G} = 0$ for $\varphi_z^{(1)} = -\varphi_z^{(2)}$, and of $|\mathcal{G}| = 1$ for $\varphi_z^{(1)} = \varphi_z^{(2)}$, respectively. Therefore, driving the atoms a change in the relative phase ϕ_z changes the collective coupling to the cavity: Atom hopping from field antinode to field antinode along the cavity axis leads to an interchange between sub- and superradiant emission into the cavity.

With the two collective coupling parameters at hand Eq. (5.5) is rewritten as for N atoms as $E_{\mathcal{M}} = iN\frac{\mathcal{L}[\Delta]}{2} \cdot \left(\mathcal{G}\frac{g_{\max}}{\Gamma} \cdot E_L + \mathcal{H}\frac{g}{\Gamma} \cdot 2E_c\right) \cdot g\tau$ and – as for a single atom – inserted into Eq. (5.3):

$$E_c = -\frac{E_L}{2}\frac{g_{\max}}{g}\frac{N\mathcal{G}}{\frac{i}{2C\mathcal{L}[\Delta]} + \frac{\delta}{2\kappa C\mathcal{L}[\Delta]} + N\mathcal{H}}. \tag{5.10}$$

Theoretically both directions, y and z are of equal importance. Experimentally, however, we do only observe clear dynamics (= atom hopping, cf. subsection 5.3.1) along the cavity axis, but not along the driving laser axis. This is why we describe the two directions separately. As a consequence we reserve the names λ- and $\lambda/2$-pattern for the z-axis only.

count rate (ms^{-1})	measurement	model	free space
one atom	9(1)	9.5	9
two atoms	12(2)	12.1	36

Table 5.4: Measured and calculated count rates for one and two atoms. We compare the data from Fig. 5.2 to the classical model for two constructively interfering atoms with $g = 8\,\mathrm{MHz}$. The free space scenario predicts a fourfold two-atom signal for the same single atom count rate.

5.2.3 The Influence of Strong Cavity Backaction

In our experiments the driving laser is resonant with the cavity and Eq. (5.10) becomes

$$E_c = -\frac{E_L}{2}\frac{g_{\max}}{g}\frac{N}{\frac{i}{2C\mathcal{L}[\Delta]}+N}, \tag{5.11}$$

where we consider the situation of N atoms ordered in a superradiant pattern ($\mathcal{G} = \mathcal{H} = 1$). In the bad cavity limit ($\kappa \gg g$ and C small) $R_\mathrm{D} \propto |E_c|^2$ (see table 5.3) scales with N^2, as it was reported for superradiant scattering from a Bose-Einstein condensate in free space [115]. Other experiments performed with ions in free space [116] or ions interacting with their mirror images [117] also show a strong N-dependence of the detected signal.

However, in the perfect cavity limit ($\kappa \to 0$ and C large) this dependency becomes negligible due to cavity backaction: The intra-cavity field builds up until it (almost) completely cancels the driving field at the positions of the N atoms. As shown in Fig. 5.2 and table 5.4 our system is close to the perfect cavity limit, thereby showing only a small difference in detected photon counts between the one- and the two-atom case.

5.3 Super- and Subradiant Two-Atom States

For $N = 2$ atoms, with the first atom fixed at an antinode of the cavity field, the coupling parameters in Eqs. (5.8) and (5.9) take the simple form

$$\begin{aligned}\mathcal{H} &= \frac{1}{2}(1+\cos^2[\phi_z])\\ \mathcal{G} &= \frac{1}{2}(1+\exp[i\phi_y]\cos[\phi_z]),\end{aligned} \tag{5.12}$$

where there relative phases read $\phi_{y,z} = |\varphi^{(1)}_{y,z} - \varphi^{(2)}_{y,z}|$. With Eqs. (5.10), (5.12) and table 5.3 the intra-cavity photon number n_p is computed and displayed in Fig. 5.4. Fig 5.4(a) shows the theoretical dependence of n_p from ϕ_z for two atoms with $\phi_y = 0$ (thick curve). For $\phi_z = 0$ the atoms realize the λ-pattern and superradiant Rayleigh

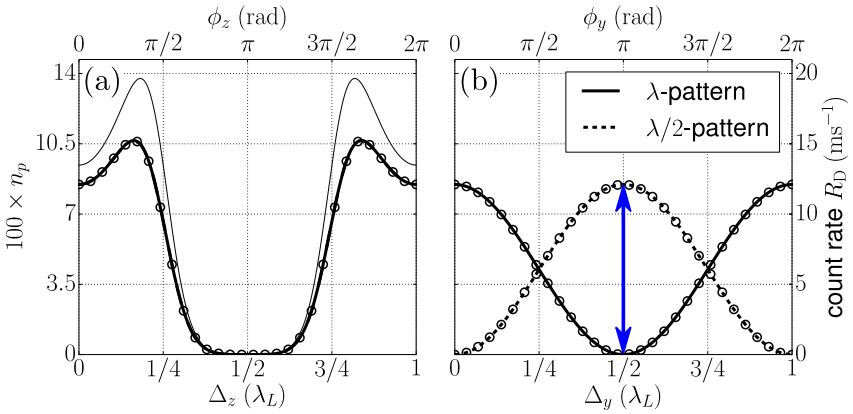

Figure 5.4: Classical (lines) and quantum mechanical (circles, see section 5.4) calculations for two driven atoms coupled to a cavity. (a) For $\phi_y = 0$ we show the intra-cavity photon number n_p for our system parameters (see section 5.1, $g = 8\,\mathrm{MHz}$, thick line) and, as a comparison, for a perfect cavity ($\kappa = 0$, thin line). The right axis shows the SPCM photon count rate R_D for our detection efficiency. (b) Expected n_p and R_D as a function of the relative driving laser phase ϕ_y for λ and $\lambda/2$-patterns. The blue double arrow illustrates the jumping between the two atomic patterns observed in Fig. 5.2(i). For this data ϕ_y is close to an integer multiple of π.

scattering into the cavity mode is expected. For $\phi_z = \pi$ ($\lambda/2$-pattern) the atoms are in a subradiant state, where no scattering into the cavity mode is predicted. Note that for $\phi_z = \pi/2$ the second atom sits at a zero-crossing of the intra-cavity field and therefore is decoupled from the cavity: the situation is equivalent to the one-atom case.

In order to compare our situation to the perfect cavity limtit, the thin curve is plotted with the same parameters as the thick one, but for $\kappa = 0$. In the perfect cavity limit no difference between the two superradiant atoms ($\phi_z = 0$) and a single emitter ($\phi_z = \pi/2$) is visible.

5.3.1 Jump Contrast and Relative Driving Phase

For each measurement trace two atoms are loaded randomly into our conveyor belt, realizing an arbitrary but fixed relative distance Δ_y and phase ϕ_y along the y-direction. Our data show that the upper and lower count rate levels of the two-atom traces are constant (cf. Fig. 5.5). This is interpreted with the atoms jumping back and forth between the λ- and the $\lambda/2$-pattern while Δ_y and ϕ_y remain fixed and corresponds to vertical jumps between the patterns in Fig. 5.4(b).

In addition, Fig. 5.4(b) illustrates the ϕ_y-dependence of the jump contrast. Besides traces such as Fig. 5.2(i) or Fig 5.5(c) where ϕ_y is close to 0 or π (maximum jump contrast), we do also observe traces with lower (see Fig 5.5(b)) or even van-

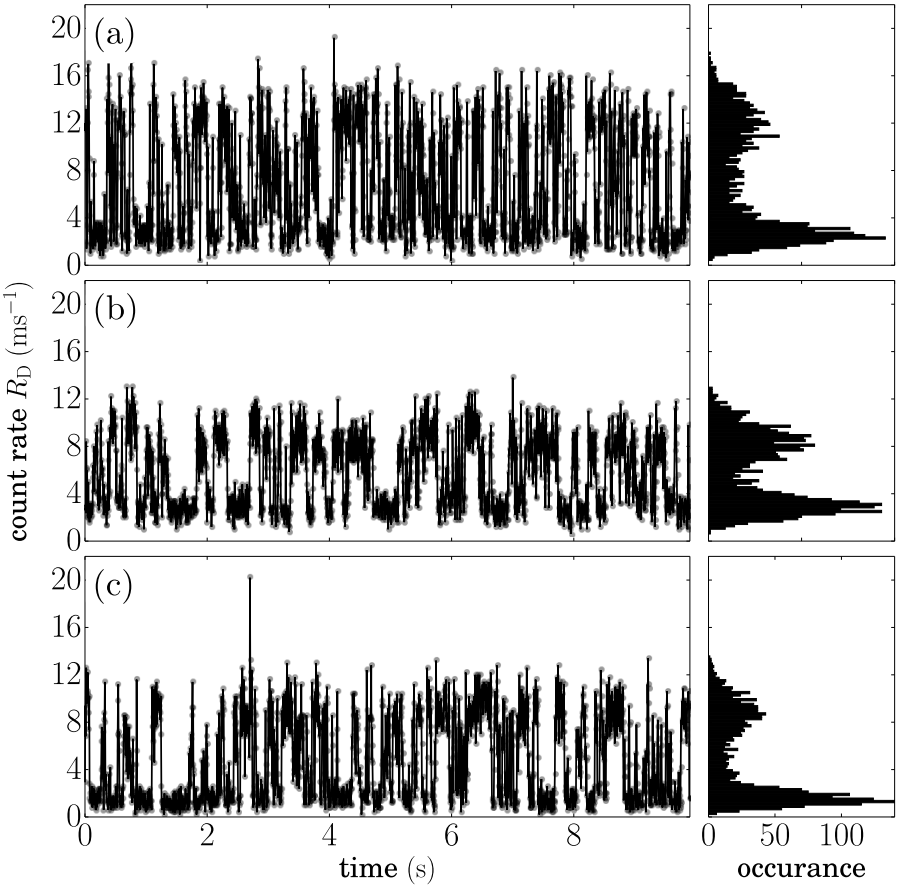

Figure 5.5: Three data traces of two driven atoms inside the cavity. The bimodal structure of the SPCM data arising from atom hopping between the λ- and $\lambda/2$-pattern is clearly visible in the time traces and in the corresponding count histograms. From the data we gain information about the phase ϕ_y and the atom-cavity coupling strength g (see text).

ishing jump contrast. The latter correspond to ϕ_y near $\frac{\pi}{2}$ or $\frac{3\pi}{2}$.

5.3.2 Extracting the Atom-Cavity Coupling Strength

We analyze the different mean values $R_{\mathrm{D}}^{(\mathrm{mean})}$ of the high and low count rate levels in our data. Example traces are shown in Fig. 5.5, where (a) shows a higher mean count rate $R_{\mathrm{D}}^{(\mathrm{mean})} \approx 7\,\mathrm{ms}^{-1}$, while (b) and (c) show lower mean values $R_{\mathrm{D}}^{(\mathrm{mean})} \approx 5\,\mathrm{ms}^{-1}$.

The expected mean count rate as a function of the atom-cavity coupling strength g is found by first evaluating Eq. (5.10) together with Eq. (5.12) at $\phi_y = \pi/2$, where both atomic patterns show the mean count rate as depicted Fig. 5.4(b).

For all recorded data traces $R_{\mathrm{D}}^{(\mathrm{mean})}$ is quantitatively evaluated by first subtracting the background from the data and then fitting the count histograms with two Gaussian functions. The mean value of the centers of the Gaussians is calculated and compared to the model. We find – in good agreement with former experiments [118] – that the atoms couple with an effective g between 8 and 10 MHz, depending on the radial atom positions within the cavity mode in each experimental repetition. Again, in analogy to the single-atom case depicted in Fig. 5.3, $R_{\mathrm{D}}^{(\mathrm{mean})}$ decreases as g increases.

5.3.3 Jump Dynamics and Cooling

The observation of hopping along the z- but not along the y-direction is explained by the fact that the dominating heating mechanism, parametric heating due to fluctuations of the intra-cavity lock laser intensity, is strong along the z-axis but negligible along the y-axis (see subsection 4.2.5). This claim is supported by the fact that 1D Raman cooling along the z-axis significantly reduces the hopping rate, see Fig. 5.6. To extract the jump rates from our noisy signals, we apply to our data the hidden Markov-model (HMM) approach presented in reference [119] with a time resolution of 50 μs, which is much faster than the inverse jump rates. The algorithm is based on two hidden states and calculates the probabilities of being in the super- and subradiant emission pattern. While Fig. 5.6(c) is measured under standard cavity cooling conditions [61], Fig. 5.6(d) shows data where an additional Raman sideband cooling beam is continuously irradiating the atoms. By only cooling on the ν_z-sideband frequency, we counteract the parametric heating, as shown in chapter 4, and reduce the jump rate, which is also extracted using the HMM model [119], from (39 ± 15) to (8 ± 4) Hz, corresponding to a factor[2] $\gtrsim 5$. For both cooling scenarios the jump rates from the super- to the subradiant state and vice versa are equal within the experimental uncertainty. This indicates that the

[2] In case of the Raman cooling data we only used data traces where clear count rate levels were visible. Traces with very little variance were excluded from the analysis since here it is not clear if two or only one atom couple to the cavity. Taking these excluded traces into account would reduce the jump rate for Raman cooling further.

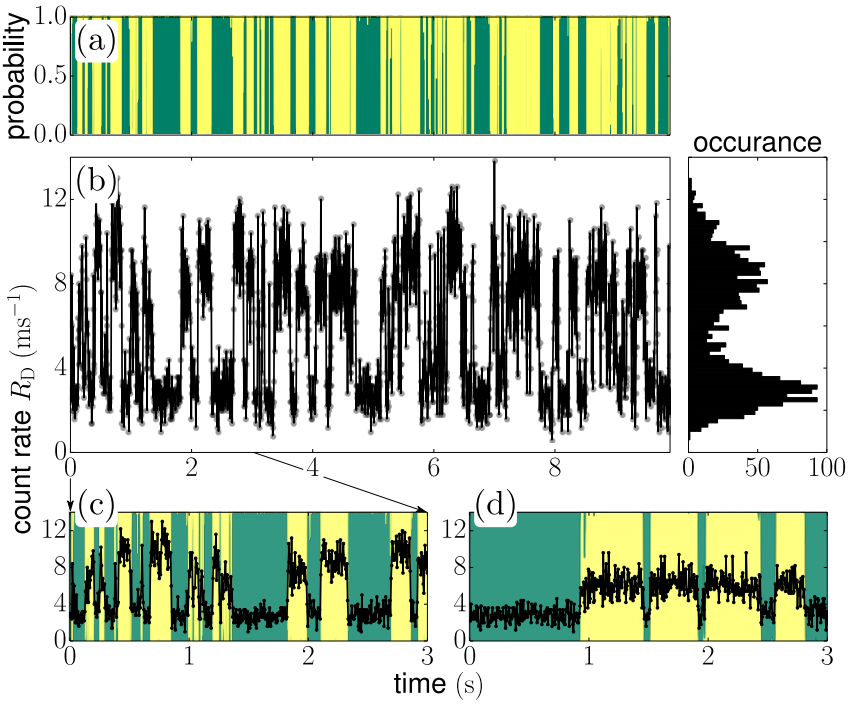

Figure 5.6: Motional dynamics between super- and subradiant states of two atoms. (a) HMM probabilities (see text) corresponding to the data in (b). The probabilities for the super- and subradiant two atom states are yellow and green, respectively. (c) and (d) compare data and HMM probabilities (background) with cavity cooling only, and with additional continuous Raman sideband cooling, respectively. The data bin time is 5 ms.

dynamics are governed by thermal excitations and not by collective forces which can lead to self-ordering [106].

5.4 Quantum Theory of Two-Atom Dicke States

Even though the classical theory can fully explain the observed effects of super- and subradiant Rayleigh scattering of two atoms, the examination of a quantum mechanical approach is advantageous for two reasons. First, new pictures and thoughts are developed as the problem is viewed from a different angle. Second, there are limits to the classical theory, which become evident as it is compared to a more general quantum theory.

5.4.1 Ideal Loss-Free Situation

Aiming at an intuitive picture, we start with a loss-free situation: The atomic excited state decay (Γ) and the cavity loss channel (2κ) are excluded from the dy-

	$\|gg\rangle$	$\|+\rangle$	$\|-\rangle$	$\|ee\rangle$
$\hat{S}_+$	0	$\|gg\rangle$	0	$\|+\rangle$
$\hat{S}_+^\dagger$	$\|+\rangle$	$\|ee\rangle$	0	0
$\hat{S}_-$	0	0	$\|gg\rangle$	$-\|-\rangle$
$\hat{S}_-^\dagger$	$\|-\rangle$	0	$-\|ee\rangle$	0

Table 5.5: Action of the Dicke operators on relevant two-atom states. It is notable that the symmetric operators $\hat{S}_+^{(\dagger)}$ cannot create the antisymmetric Dicke state $|-\rangle$, whereas the antisymmetric operators $\hat{S}_-^{(\dagger)}$ cannot create the symmetric Dicke state $|+\rangle$. This means the operators do not mix the symmetric and the antisymmetric states in the low excitation limit.

namics. The coherent internal dynamics of two atoms in a cavity under transversal driving is described by the Hamiltonian [120]

$$\begin{aligned}
\hat{H} &= \hat{H}_{\text{at}} + \hat{H}_{\text{cav}} + \hat{H}_{\text{at-cav}} + \hat{H}_L \quad \text{with} \\
\hat{H}_{\text{at}} &= -\hbar\Delta \sum_{n=1,2} \hat{\sigma}_n^\dagger \hat{\sigma}_n \\
\hat{H}_{\text{cav}} &= -\hbar\delta\, \hat{a}^\dagger \hat{a} \\
\hat{H}_{\text{at-cav}} &= \hbar \sum_{n=1,2} g_n (\hat{a}^\dagger \hat{\sigma}_n + \hat{a}\hat{\sigma}_n^\dagger) \\
\hat{H}_L &= \hbar/2 \left((\Omega_1^* \hat{\sigma}_1^\dagger + \Omega_1 \hat{\sigma}_1) + (\Omega_2^* \hat{\sigma}_2^\dagger + \Omega_2 \hat{\sigma}_2) \right).
\end{aligned} \tag{5.13}$$

The atomic Hamiltonian $\hat{H}_{\text{at}}$ depends on the atomic rising and lowering operators $\hat{\sigma}_n^\dagger = |e\rangle_n\langle g|$ and $\hat{\sigma}_n = |g\rangle_n\langle e|$, which change the internal state of atom n. The cavity field operators $\hat{a}^\dagger$ and $\hat{a}$ enter the cavity field Hamiltonian $\hat{H}_{\text{cav}}$ and create or annihilate photons, respectively.

The interaction between atom and cavity field is governed by $\hat{H}_{\text{at-cav}}$. The atom-cavity coupling strength of atom n is given with $g_n = g\cos[\varphi_z^{(n)}]$. If both atoms are at the antinodes of the intra-cavity standing wave, a λ-pattern for $\phi_z = |\varphi_z^{(1)} - \varphi_z^{(2)}| = 0$ with $g_1 = g_2$, and a $\lambda/2$-pattern for $\phi_z = \pi$ with $g_1 = -g_2$ is realized.

The operator $\hat{H}_{\text{L}}$ describes the interaction between atoms and the non-quantized transversal driving-laser field. The Rabor frequencies are given by $\Omega_1 = \Omega_L e^{i\phi_y/2}$ and $\Omega_2 = \Omega_L e^{-i\phi_y/2}$ with $\Omega_L = \Gamma\sqrt{I_L/(2I_{\text{sat}})}$ and $I_{\text{sat}} \approx 1.1\,\text{mW/cm}^2$ [37].

The relative phase ϕ_y and the detunings δ and Δ are defined in sections 5.1 and 5.3, respectively.

If one wants to understand the dynamics of the atom-cavity system it is instructive to transfer its inherent symmetry to the form of the Hamiltonian. We use the abbreviation $|ij\rangle = |i\rangle_1 \otimes |j\rangle_2$ for the two-atom state. If necessary the cavity state is included by $|ij, k_c\rangle = |i\rangle_1 \otimes |j\rangle_2 \otimes |k\rangle_c$.

Following [109] the symmetric and antisymmetric Dicke states $|\pm\rangle = (|eg\rangle \pm |ge\rangle)/\sqrt{2}$ are introduced. The Dicke states are created from the atomic ground state with the help of the Dicke operators

$$\hat{S}_\pm = \frac{1}{\sqrt{2}}(\hat{\sigma}_1 \pm \hat{\sigma}_2), \tag{5.14}$$

by $\hat{S}_\pm^\dagger|gg\rangle = |\pm\rangle$. The action of the Dicke operators on their natural basis vectors is shown in table 5.5.

Within the further discussion in this section the state $|ee\rangle$ will be neglected. This is allowed in the low excitation limit, where the population in $|ee\rangle$ is small.

Using Eq. (5.14) the atom-cavity interaction in Eq. (5.13) is written as

$$\begin{aligned} \hat{H}_{\text{at-cav}} &= \hat{H}_+ + \hat{H}_- \quad \text{with} \\ \hat{H}_\pm &= \hbar g_\pm(\hat{a}\hat{S}_\pm^\dagger + \hat{a}^\dagger\hat{S}_\pm) \quad \text{and} \\ g_\pm &= \frac{1}{\sqrt{2}}(g_1 \pm g_2) = \frac{g}{\sqrt{2}}(1 \pm \cos[\phi_z]), \end{aligned} \tag{5.15}$$

where – analog to the classical calculus – for the second equal sign of the last equation one atom is fixed at an antinode of the intra-cavity standing wave, while the other atom is free to move along the z-axis.

The laser-atom interaction is rewritten as

$$\hat{H}_L = \hbar/2 \cdot \sqrt{2}\Omega_L \left(\cos[\phi_y/2]\hat{S}_+ + i\sin[\phi_y/2]\hat{S}_- + \text{H.c.}\right). \tag{5.16}$$

Fig. 5.7 pictures the dynamics governed by $\hat{H}_L$ (a) and $\hat{H}_{\text{at-cav}}$ (b) in the low excitation limit.

For a relative driving phase $\phi_y = 0$ (e.g. both atoms at the same y-position) only the atomic state $|+\rangle$ is populated. If a λ-pattern is realized, $\hat{H}_+$ couples the atoms to the cavity mode and maximum cavity output can be detected, whereas a $\lambda/2$-pattern, coupled to the cavity by $\hat{H}_-$, leads to no cavity output.

For $\phi_y = \pi$ the situation is reversed and a $\lambda/2$-pattern leads to maximum cavity output.

Realizing any phase in between, emission of photons into the cavity mode is expected for both atomic patterns. A special case is $\phi_y = \pi/2$. Here no difference in the cavity output is predicted for either pattern, as already discussed for the classical calculations in section 5.3.

It is notable that the collective coupling rates are increased by $\sqrt{2}$ compared to the single atom rates, compare Eqs. (5.15), (5.16) to Eq. (5.13). This $\sqrt{N}$-enhancement is typical for Dicke dynamics [27, 108].

5.4.2 Master Equation Approach

For a quantitative comparison to the measured data and to the classical theory the master equation of the system is solved. Following [120], the dynamics of the

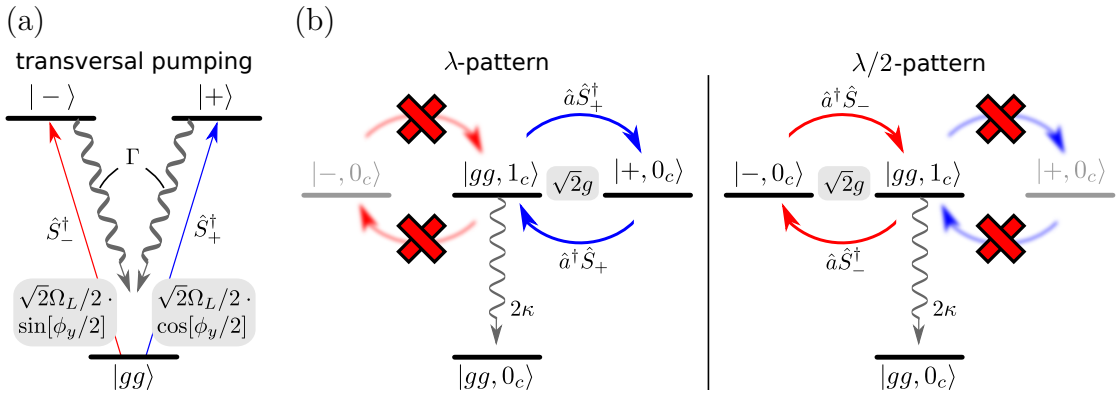

Figure 5.7: Quantum-mechanical picture of super- and subradiant scattering of two atoms in a cavity. (a) Driving laser pumping the Dicke states. As a function of the relative driving phase ϕ_y the symmetric $|+\rangle$ or antisymmetric $|-\rangle$ Dicke state is weakly excited. (b) Coupling to the cavity for λ-pattern, $\phi_z = 0$ and $\lambda/2$-pattern, $\phi_z = \pi$. Depending on the atomic pattern, only $|+\rangle$ or only $|-\rangle$ couples to the cavity. If the cavity-coupled Dicke state is pumped by the driving laser, the cavity mode is populated with photons ($|0_c\rangle \rightarrow |1_c\rangle$), which leave the system via the cavity loss channel 2κ and can be detected by the SPCM (see Fig. 5.1(a)).

system are described by the Lindblad master equation for the density matrix ρ of atoms and cavity mode:

$$\begin{aligned}\frac{\partial}{\partial t}\hat{\rho} = \frac{1}{i\hbar}[\hat{H},\hat{\rho}] + \frac{\Gamma}{2}\sum_{n=1,2}(2\hat{\sigma}_n\hat{\rho}\hat{\sigma}_n^\dagger - \hat{\sigma}_n^\dagger\hat{\sigma}_n\hat{\rho} - \hat{\rho}\hat{\sigma}_n^\dagger\hat{\sigma}_n) \\ + \kappa(2\hat{a}\hat{\rho}\hat{a}^\dagger - \hat{a}^\dagger\hat{a}\hat{\rho} - \hat{\rho}\hat{a}^\dagger\hat{a}).\end{aligned} \tag{5.17}$$

The Hamiltonian is given in Eq. (5.13) and the incoherent dynamics are governed by the atomic decay via Γ and the cavity decay via 2κ.

The master equation is numerically solved [121] for the steady-state density matrix $\hat{\rho}_{\mathrm{ss}}$ and the intra-cavity photon number is calculated according to $n_p = \langle\hat{a}^\dagger\hat{a}\rangle = \mathrm{Tr}\left[\hat{a}^\dagger\hat{a}\hat{\rho}_{\mathrm{ss}}\right]$, where Tr denotes the trace operation. With table 5.3 the SPCM count rate R_{D} is calculated. For our parameters the results fully agree with the classical calculus (see Fig. 5.4).

5.5 Limits of the Classical Description

The master equation approach also holds if the atoms are driven into saturation and the excited state populations $\rho_{ee}^{(n)} = \mathrm{Tr}\left[|e\rangle_n\langle e|\hat{\rho}_{\mathrm{ss}}\right]$ are not negligible. For our measurements $\rho_{ee}^{(n)} < 10^{-3}$.

The classical analog to ρ_{ee} is the squared amplitude a^2_{dipole} of the driven dipole (see Eq. (5.7)), which does not saturate as the intensity is increased. Therefore, for strong driving, which – without any notable difference in the theoretical results – is realized by decreasing Δ or increasing I_L, the classical theory is expected to fail in describing real world atoms. Specifically incoherent scattering, which is not

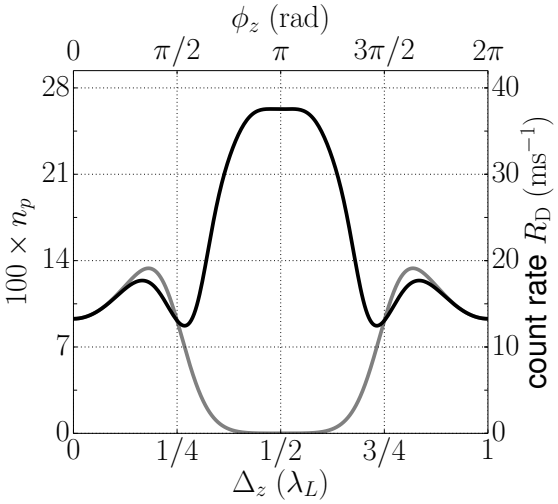

Figure 5.8: Comparison between quantum mechanical (black) and classical (gray) calculus for strong driving of two atoms inside a cavity. All parameters are chosen equally to Fig. 5.4, except for the laser-atom detuning that is reduced form $\Delta = 100\,\text{MHz}$ to 0. This leads to atomic saturation with $\rho_{ee}^{(n)} > 0.25$ for the $\lambda/2$-pattern ($\phi_z = \pi$), which is not taken into account in the classical approach.

included in the classical theory, becomes dominant for significant atomic populations $\rho_{ee}^{(n)}$. In this limit the behavior of the system changes significantly. Fig. 5.8 illustrates the quantum mechanical (black line) and the wrong classical (gray line) solution for strong driving. Here a higher detection rate in case of the $\lambda/2$-pattern ($\phi_z = \pi$) than in case of the λ-pattern ($\phi_z = 0$) is expected. In the $\lambda/2$-configuration $\rho_{ee}^{(n)}$ becomes large and incoherent scattering dominates compared to Rayleigh scattering: Interference effects become negligible and the Dicke-state picture, shown in Fig 5.7, is invalid. Reference [120] describes the strong driving limit is in more detail.

A last remark on the approximations that have been made as the classical theory was developed in subsection 5.2.1: The waist of the cavity mode $w_{0,\mathcal{M}}$, which scales inversely with g, was assumed to be much bigger than λ_L and the approximation for the cavity field decay rate $\kappa = (1 - r^2)/\tau$ only holds for $r \approx 1$. Therefore the fast cavity limit, also called Purcell limit [111,122], ($C \sim 1$, $\kappa > g, \Gamma$) is not covered by the classical theory since this limit is realized for large κ and g while at the same time Γ needs to be small.

6 Conclusion and Outlook

Within this thesis advanced motional control and cooperative effects of atoms strongly coupled to a high-finesse cavity have been shown.

6.1 Motional Control

On the one hand the investigated carrier-free Raman cooling scheme turned out to be the approach of choice for reaching the 2D motional ground state of atoms coupled to our cavity. On the other hand the presented measurements implement and characterize a method that should be valuable to a range of atomic physics experiments. It provides a robust experimental solution for ever more integrated and miniaturized setups, which make the fast and lossless preparation of cold atoms a significant challenge. We highlight that the absence of the carrier is a generic feature of any scheme that traps atoms in the zero-crossing of the electric field of one of the two Raman beams. Carrier-free Raman manipulation is therefore suitable for many blue detuned optical dipole potentials, including optical lattices, microtrap arrays and higher order paraxial (e.g. "doughnut") beams [123].

The 2D ground state cooling can further be extended to all three dimensions by implementing strong confinement along the x-direction, for example by a third standing wave dipole trap. Additionally the propagation direction of the Raman laser needs to be changed in this case to include a projection along the x-direction.

Finally due to its straightforward and established method for temperature extraction [75] the scheme can be applied to benchmark other less established and more complicated thermometrical measurement schemes. Indeed measurements comparing Raman-spectroscopy to heterodyne-spectroscopy [85] data have already been taken and we plan on publishing the material soon.

6.2 Cooperative Coupling

During the analysis of the cavity-modified super- and subradiant Rayleigh scattering of two atoms it became clear that the systems behavior is governed by the relative phases of the light fields at the atom positions. We demonstrated the extraction of information on these relative phases and employed carrier-free Raman cooling to reduce the jump rate between super- and subradiant configurations. Thereby we improved the control over the system to a level where the realization of two-atom entanglement schemes, which involve optical cavities and rely on the measured relative phase information, become feasible [124–126].

The classical analysis intuitively explained that the cavity output power for superradiant scattering of two atoms is almost equal to the single emitter case: the effect is based on cavity backaction which becomes strong in the good cavity limit. The quantum mechanical explanation reveals that our system and its inherent symmetry are well described by the language of cooperative Dicke states [108].

Recently the general interest in many-atom Dicke-physics proposals involving cavities [27, 106] is increasing [127]. In reference [107] self-ordering and a Dicke phase transition of 10^5 driven atoms inside a cavity have been observed. Extending our carrier-free Raman cooling scheme to reach 3D motional control (see above), we could be able to perform experiments in a regime where self-ordering can be studied with as few as 10 to 100 atoms [106]. Our ability to precisely control the intracavity atom number N would enable us to investigate the onset of self-ordering as one atom after another is added to the system.

Such experiments aiming at a bottom-up approach also start to emerge in the ion community, where collective coupling involving super- and subradiant states of two ions in a cavity has been reported [128].

Bibliography

[1] J. M. Raimond and S. Haroche, *Exploring the Quantum: Atoms, Cavities and Photons*, Oxford University Press, Oxford, UK (2006)

[2] E. Jaynes and F. Cummings, *Comparison of quantum and semiclassical radiation theories with application to the beam maser*, Proc. IEEE **51**, 89 (1963)

[3] S. Haroche and D. Kleppner, *Cavity Quantum Electrodynamics*, Phys. Today **42**, 24 (1989)

[4] T. Wilk, S. C. Webster, A. Kuhn, and G. Rempe, *Single-Atom Single-Photon Quantum Interface.*, Science **317**, 488 (2007)

[5] T. E. Northup and R. Blatt, *Quantum information transfer using photons*, Nat. Photonics **8**, 356 (2014)

[6] A. Kuhn, M. Hennrich, and G. Rempe, *Deterministic Single-Photon Source for Distributed Quantum Networking*, Phys. Rev. Lett. **89**, 067901 (2002)

[7] J. McKeever, A. Boca, A. Boozer, R. Miller, J. Buck, A. Kuzmich, and H. J. Kimble, *Deterministic Generation of Single Photons from One Atom Trapped in a Cavity*, Science **303**, 1992 (2004)

[8] M. Hijlkema, B. Weber, H. P. Specht, S. C. Webster, A. Kuhn, and G. Rempe, *A single-photon server with just one atom*, Nat. Phys. **3**, 253 (2007)

[9] W. Chen, K. Beck, R. Bücker, M. Gullans, M. Lukin, H. Tanji-Suzuki, and V. Vuletić, *All-Optical Switch and Transistor Gated by One Stored Photon*, Science **768** (2013)

[10] H. J. Kimble, *The quantum internet*, Nature **453**, 1023 (2008)

[11] J. Cirac, P. Zoller, H. J. Kimble, and H. Mabuchi, *Quantum State Transfer and Entanglement Distribution among Distant Nodes in a Quantum Network*, Phys. Rev. Lett. **78**, 3221 (1997)

[12] S. Ritter, C. Nölleke, C. Hahn, A. Reiserer, A. Neuzner, M. Uphoff, M. Mücke, E. Figueroa, J. Bochmann, and G. Rempe, *An elementary quantum network of single atoms in optical cavities*, Nature **484**, 195 (2012)

[13] M. H. Anderson, J. R. Ensher, M. R. Matthews, C. E. Wieman, and E. A. Cornell, *Observation of Bose-Einstein condensation in a dilute atomic vapor*, Science **269**, 198 (1995)

[14] Y. Colombe, T. Steinmetz, G. Dubois, F. Linke, D. Hunger, and J. Reichel, *Strong atom-field coupling for Bose-Einstein condensates in an optical cavity on a chip*, Nature **450**, 272 (2007)

[15] H. Ritsch, P. Domokos, F. Brennecke, and T. Esslinger, *Cold atoms in cavity-generated dynamical optical potentials*, Rev. Mod. Phys. **85**, 553 (2013)

[16] M. Bienert and G. Morigi, *Cavity cooling of a trapped atom using electromagnetically induced transparency*, New J. Phys. **14**, 023002 (2012)

[17] A. Boozer, *Theory of Raman transitions in cavity QED*, Phys. Rev. A **78**, 033406 (2008)

[18] A. Kaufman, B. Lester, and C. Regal, *Cooling a Single Atom in an Optical Tweezer to its Quantum Ground State*, Phys. Rev. X **2**, 041014 (2012)

[19] J. D. Thompson, T. G. Tiecke, a. S. Zibrov, V. Vuletić, and M. D. Lukin, *Coherence and Raman Sideband Cooling of a Single Atom in an Optical Tweezer*, Phys. Rev. Lett. **110**, 133001 (2013)

[20] A. D. Boozer, A. Boca, R. Miller, T. E. Northup, and H. J. Kimble, *Cooling to the Ground State of Axial Motion for One Atom Strongly Coupled to an Optical Cavity*, Phys. Rev. Lett. **97**, 083602 (2006)

[21] A. Reiserer, C. Nölleke, S. Ritter, and G. Rempe, *Ground-State Cooling of a Single Atom at the Center of an Optical Cavity*, Phys. Rev. Lett. **110**, 223003 (2013)

[22] P. Anderson, *More Is Different*, Science **177**, 393 (1972)

[23] S. Slama, S. Bux, G. Krenz, C. Zimmermann, and P. Courteille, *Superradiant Rayleigh Scattering and Collective Atomic Recoil Lasing in a Ring Cavity*, Phys. Rev. Lett. **98**, 053603 (2007)

[24] H. Keßler, J. Klinder, M. Wolke, and A. Hemmerich, *Steering Matter Wave Superradiance with an Ultranarrow-Band Optical Cavity*, Phys. Rev. Lett. **113**, 070404 (2014)

[25] A. Black, H. Chan, and V. Vuletić, *Observation of Collective Friction Forces due to Spatial Self-Organization of Atoms: From Rayleigh to Bragg Scattering*, Phys. Rev. Lett. **91**, 203001 (2003)

[26] H. Tanji-Suzuki, I. Leroux, M. H. Schleier-Smith, M. Cetina, A. Grier, J. Simon, and V. Vuletić, *Interaction between Atomic Ensembles and Optical Resonators: Classical Description*, Adv. At. Mol. Opt. Phys. **60**, 201 (2011)

[27] F. Dimer, B. Estienne, A. Parkins, and H. Carmichael, *Proposed realization of the Dicke-model quantum phase transition in an optical cavity QED system*, Phys. Rev. A **75**, 013804 (2007)

[28] S. Kuhr, *A controlled quantum system of individual neutral atoms*, Ph.D. thesis, Bonn (2003)

[29] W. Alt, *Optical control of single neutral atoms*, Ph.D. thesis, Universtiy Bonn (2004)

[30] D. Schrader, *A neutral atom quantum register*, Ph.D. thesis, Bonn (2004)

[31] Y. Miroshnychenko, *An atom-sorting machine*, Ph.D. thesis, Bonn (2006)

[32] I. Dotsenko, *Single atoms on demand for cavity QED experiments*, Ph.D. thesis, Bonn (2007)

[33] M. Khudaverdyan, *A controlled one and two atom-cavity system*, Ph.D. thesis, University Bonn (2009)

[34] S. Reick, *Internal and external dynamics of a strongly-coupled atom-cavity system*, Ph.D. thesis, Bonn (2009)

[35] T. Kampschulte, *Coherently driven three-level atoms in an optical cavity*, Ph.D. thesis, Bonn (2011)

[36] A. Thobe, *Quantum Jumps of One and Two Atoms in a Strongly Coupled Atom-Cavity System*, master thesis, Bonn (2009)

[37] D. Steck, *Cesium D line data*, Los Alamos Natl. Lab. (2010)

[38] M. Gehm, K. O'Hara, T. Savard, and J. Thomas, *Dynamics of noise-induced heating in atom traps*, Phys. Rev. A **58**, 3914 (1998)

[39] Analog Devices, *AD9954 data sheet*, Analog Devices (2009)

[40] R. P. Scott, C. Langrock, B. H. Kolner, and S. Member, *High-Dynamic-Range Laser Amplitude and Phase Noise Measurement Techniques*, IEEE J. Sel. Top. QUANTUM Electron. **7**, 641 (2001)

[41] C. Wieman and L. Hollberg, *Using diode lasers for atomic physics*, Rev. Sci. Instrum. **62**, 1 (1991)

[42] X. Baillard, A. Gauguet, S. Bize, P. Lemonde, P. Laurent, A. Clairon, and P. Rosenbusch, *Interference-filter-stabilized external-cavity diode lasers*, arXiv:0605046v1 pp. 1–12 (2006)

[43] M. Ito and T. Kimura, *Stationary and transient thermal properties of semiconductor laser diodes*, Quantum Electron. IEEE J. **17**, 787 (1981)

[44] R. W. P. Drever, J. L. Hall, F. V. Kowalski, J. Hough, G. M. Ford, a. J. Munley, and H. Ward, *Laser Phase and Frequency Stabilization Using an Optical Resonator*, Appl. Phys. B Photophysics Laser Chem. **31**, 97 (1983)

[45] E. D. Black, *An introduction to Pound-Drever-Hall laser frequency stabilization*, Am. J. Phys. **69**, 79 (2001)

[46] B. Schottstaedt, *An Introduction To FM*, URL https://ccrma.stanford.edu/software/snd/snd/fm.html

[47] W. Rosenfeld, *A high finesse optical resonator for cavity QED experiments*, master thesis, University Bonn (2003)

[48] J. J. Sakurai and J. Napolitano, *Modern Quantum Mechanics*, 2 edition, Addison-Wesley

[49] C. Cohen-Tannoudji, B. Diu, and F. Laloe, *Quantenmechanik, Band 1*, 4 edition, de Gruyter (2009)

[50] S. Hamann, D. Haycock, G. Klose, P. Pax, I. Deutsch, and P. Jessen, *Resolved-Sideband Raman Cooling to the Ground State of an Optical Lattice*, Phys. Rev. Lett. **80**, 4149 (1998)

[51] W. Happer, *Optical Pumping*, RMP **44**, 169 (1972)

[52] F. Schmidt-Kaler and R. Blatt, *Laser cooling of trapped ions* **20**, 1003 (2003)

[53] F. Diedrich, J. Bergquist, W. W. M. Itano, D. Wineland, and J. Wineland, *Laser cooling to the zero-point energy of motion.*, Phys. Rev. Lett. **62**, 403 (1989)

[54] V. Vuletic and S. Chu, *Laser cooling of atoms, ions, or molecules by coherent scattering*, Phys. Rev. Lett. **84**, 3787 (2000)

[55] P. Domokos, P. Horak, and H. Ritsch, *Semiclassical theory of cavity-assisted atom cooling* **4075**, 187 (2001)

[56] K. Murr, *On the suppression of the diffusion and the quantum nature of a cavity mode. Optical bistability: forces and friction in driven cavities*, J. Phys. B At. Mol. Opt. Phys. **36**, 2515 (2003)

[57] V. Vuletić, H. Chan, and A. Black, *Three-dimensional cavity Doppler cooling and cavity sideband cooling by coherent scattering*, Phys. Rev. A **64**, 033405 (2001)

[58] G. Hechenblaikner, M. Gangl, P. Horak, and H. Ritsch, *Cooling an atom in a weakly driven high-Q cavity*, Phys. Rev. A **58**, 3030 (1998)

[59] H. J. Metcalf and P. van der Straten, *Laser Cooling and Trapping*, Springer, New York (1999)

[60] M. Bienert and G. Morigi, *Cooling the motion of a trapped atom with a cavity field*, Phys. Rev. A **86**, 053402 (2012)

[61] S. Zippilli and G. Morigi, *Cooling Trapped Atoms in Optical Resonators*, Phys. Rev. Lett. **95**, 143001 (2005)

[62] S. Zippilli and G. Morigi, *Mechanical effects of optical resonators on driven trapped atoms: Ground-state cooling in a high-finesse cavity*, Phys. Rev. A **72**, 053408 (2005)

[63] J. Ye, D. Vernooy, and H. Kimble, *Trapping of Single Atoms in Cavity QED*, Phys. Rev. Lett. **83**, 4987 (1999)

[64] H. J. Kimble, J. Mckeever, J. R. Buck, a. D. Boozer, A. Kuzmich, H. Na, H.-C. Nägerl, and D. M. Stamper-Kurn, *State-Insensitive Cooling and Trapping of Single Atoms in an Optical Cavity*, Phys. Rev. Lett. **90**, 133602 (2003)

[65] P. Maunz, T. Puppe, I. Schuster, N. Syassen, P. W. H. Pinkse, and G. Rempe, *Cavity cooling of a single atom.*, Nature **428**, 50 (2004)

[66] S. Nußmann, K. Murr, M. Hijlkema, B. Weber, A. Kuhn, and G. Rempe, *Vacuum-stimulated cooling of single atoms in three dimensions*, Nat. Phys. **1**, 122 (2005)

[67] D. Leibrandt, J. Labaziewicz, V. Vuletić, and I. Chuang, *Cavity Sideband Cooling of a Single Trapped Ion*, Phys. Rev. Lett. **103**, 103001 (2009)

[68] B. L. Chuah, N. C. Lewty, R. Cazan, and M. D. Barrett, *Sub-Doppler cavity cooling beyond the Lamb-Dicke regime*, Phys. Rev. A **87**, 043420 (2013)

[69] H. Chan, A. Black, and V. Vuletić, *Observation of Collective-Emission-Induced Cooling of Atoms in an Optical Cavity*, Phys. Rev. Lett. **90**, 063003 (2003)

[70] M. H. Schleier-Smith, I. D. Leroux, H. Zhang, M. a. Van Camp, and V. Vuletić, *Optomechanical Cavity Cooling of an Atomic Ensemble*, Phys. Rev. Lett. **107**, 143005 (2011)

[71] M. Wolke, J. Klinner, H. Keßler, and A. Hemmerich, *Cavity cooling below the recoil limit*, Science **337**, 75 (2012)

[72] T. J. Kippenberg and K. J. Vahala, *Cavity Optomechanics: Back-Action at the Mesoscale*, Science **321**, 1172 (2008)

[73] G. Morigi, *Cooling atomic motion with quantum interference*, Phys. Rev. A **67**, 033402 (2003)

[74] C. Monroe, D. Meekhof, B. King, S. R. Jefferts, W. M. Itano, D. J. Wineland, and P. Gould, *Resolved-sideband Raman cooling of a bound atom to the 3D zero-point energy*, Phys. Rev. Lett. **75**, 4011 (1995)

[75] D. Leibfried, R. Blatt, C. Monroe, and D. Wineland, *Quantum dynamics of single trapped ions*, Rev. Mod. Phys. **75**, 281 (2003)

[76] V. Vuletić, C. Chin, A. Kerman, and S. Chu, *Degenerate Raman Sideband Cooling of Trapped Cesium Atoms at Very High Atomic Densities*, Phys. Rev. Lett. **81**, 5768 (1998)

[77] A. Kerman, V. Vuletić, C. Chin, and S. Chu, *Beyond optical molasses: 3D Raman sideband cooling of atomic cesium to high phase-space density*, Phys. Rev. Lett. **84**, 439 (2000)

[78] M. Fleischhauer and J. P. Marangos, *Electromagnetically induced transparency : Optics in coherent media* **77**, 633 (2005)

[79] G. Morigi, J. Eschner, and C. Keitel, *Ground state laser cooling using electromagnetically induced transparency*, Phys. Rev. Lett. **85**, 4458 (2000)

[80] C. F. Roos, D. Leibfried, A. Mundt, F. Schmidt-Kaler, J. Eschner, and R. Blatt, *Experimental demonstration of ground state laser cooling with electromagnetically induced transparency*, Phys. Rev. Lett. **85**, 5547 (2000)

[81] T. Kampschulte, W. Alt, S. Manz, M. Martinez-Dorantes, R. Reimann, S. Yoon, D. Meschede, M. Bienert, and G. Morigi, *Electromagnetically-induced-transparency control of single-atom motion in an optical cavity*, Phys. Rev. A **033404**, 1 (2014)

[82] T. Kampschulte, W. Alt, S. Brakhane, M. Eckstein, R. Reimann, A. Widera, and D. Meschede, *Optical Control of the Refractive Index of a Single Atom*, Phys. Rev. Lett. **105**, 153603 (2010)

[83] T. Savard, K. O'Hara, and J. Thomas, *Laser-noise-induced heating in far-off resonance optical traps*, Phys. Rev. A **56**, R1095 (1997)

[84] S. Stenholm, *The semiclassical theory of laser cooling*, Rev. Mod. Phys. **58**, 699 (1986)

[85] S. Manz, *Heterodyne spectroscopy with single atoms in a high-finesse optical cavity*, master thesis, Bonn (2012)

[86] S. Kuhr, W. Alt, D. Schrader, I. Dotsenko, Y. Miroshnychenko, W. Rosenfeld, M. Khudaverdyan, V. Gomer, A. Rauschenbeutel, and D. Meschede, *Coherence Properties and Quantum State Transportation in an Optical Conveyor Belt*, Phys. Rev. Lett. **91**, 213002 (2003)

[87] A. Fuhrmanek, R. Bourgain, Y. R. P. Sortais, and A. Browaeys, *Free-Space Lossless State Detection of a Single Trapped Atom*, Phys. Rev. Lett. **106**, 133003 (2011)

[88] M. J. Gibbons, C. D. Hamley, C.-Y. Shih, and M. S. Chapman, *Nondestructive Fluorescent State Detection of Single Neutral Atom Qubits*, Phys. Rev. Lett. **106**, 133002 (2011)

[89] M. Khudaverdyan, W. Alt, T. Kampschulte, S. Reick, a. Thobe, a. Widera, and D. Meschede, *Quantum Jumps and Spin Dynamics of Interacting Atoms in a Strongly Coupled Atom-Cavity System*, Phys. Rev. Lett. **103**, 123006 (2009)

[90] J. Bochmann, M. Mücke, C. Guhl, S. Ritter, G. Rempe, and D. L. Moehring, *Lossless State Detection of Single Neutral Atoms*, Phys. Rev. Lett. **104**, 203601 (2010)

[91] R. Gehr, J. Volz, G. Dubois, T. Steinmetz, Y. Colombe, B. L. Lev, R. Long, J. Estève, and J. Reichel, *Cavity-Based Single Atom Preparation and High-Fidelity Hyperfine State Readout*, Phys. Rev. Lett. **104**, 203602 (2010)

[92] J. Volz, R. Gehr, G. Dubois, J. Estève, and J. Reichel, *Measurement of the internal state of a single atom without energy exchange.*, Nature **475**, 210 (2011)

[93] V. Braginsky, Y. Vorontsov, and K. Thorne, *Quantum nondemolition measurements*, Science **209**, 547 (1980)

[94] S. Chaudhury, G. Smith, K. Schulz, and P. Jessen, *Continuous Nondemolition Measurement of the Cs Clock Transition Pseudospin*, Phys. Rev. Lett. **96**, 043001 (2006)

[95] A. Myerson, D. Szwer, S. Webster, D. Allcock, M. Curtis, G. Imreh, J. Sherman, D. Stacey, A. Steane, and D. Lucas, *High-Fidelity Readout of Trapped-Ion Qubits*, Phys. Rev. Lett. **100**, 200502 (2008)

[96] A. Keselman, Y. Glickman, N. Akerman, S. Kotler, and R. Ozeri, *High-fidelity state detection and tomography of a single-ion Zeeman qubit*, New J. Phys. **13**, 073027 (2011)

[97] A. Keselman, *High Fidelity Ion Qubit State Detection*, Ph.D. thesis, Weizmann Institute of Science (2010)

[98] C. E. Langer, *High Fidelity Quantum Information Processing with Trapped Ions*, Ph.D. thesis, University of Colorado (2006)

[99] S. Brakhane, *Kontrolle der Atom-Resonator-Wechselwirkung mit Hilfe einer Regelschleife*, master thesis, University of Bonn (2011)

[100] F. Nogrette, H. Labuhn, S. Ravets, D. Barredo, L. Béguin, a. Vernier, T. Lahaye, and a. Browaeys, *Single-Atom Trapping in Holographic 2D Arrays of Microtraps with Arbitrary Geometries*, Phys. Rev. X **4**, 021034 (2014)

[101] K. Schörner, *Ein phasenstabilisiertes Lasersystem für resonatorinduzierte Raman-Prozesse*, master thesis, Bonn (2008)

[102] M. Eckstein, *Three-Level Physics of a Single Atom Coupled to a High Finesse Cavity*, master thesis, Bonn (2010)

[103] S. Hild, *Resolved Raman sideband cooling in a doughnut-shaped optical trap*, master thesis, Bonn (2011)

[104] D. J. Wineland and W. M. Itano, *Laser cooling of atoms*, Phys. Rev. A **20**, 1521 (1979)

[105] M. Khudaverdyan, W. Alt, I. Dotsenko, T. Kampschulte, K. Lenhard, A. Rauschenbeutel, S. Reick, K. Schörner, A. Widera, and D. Meschede, *Controlled insertion and retrieval of atoms coupled to a high-finesse optical resonator*, New J. Phys. **10**, 073023 (2008)

[106] P. Domokos and H. Ritsch, *Collective Cooling and Self-Organization of Atoms in a Cavity*, Phys. Rev. Lett. **89**, 253003 (2002)

[107] K. Baumann, C. Guerlin, F. Brennecke, and T. Esslinger, *Dicke quantum phase transition with a superfluid gas in an optical cavity*, Nature **464**, 1301 (2010)

[108] R. Dicke, *Coherence in Spontaneous Radiation Processes*, Phys. Rev. **93**, 99 (1954)

[109] S. Fernández-Vidal, S. Zippilli, and G. Morigi, *Nonlinear optics with two trapped atoms*, Phys. Rev. A **76**, 053829 (2007)

[110] R. Grimm, M. Weidemüller, and Y. B. Ovchinnikov, *Optical dipole traps for neutral atoms*, Adv. At., Mol., Opt. Phys. **42**, 95 (2000)

[111] E. Purcell, *Spontaneous emission probabilities at radio frequencies*, Phys. Rev. **69**, 681 (1946)

[112] M. Motsch, M. Zeppenfeld, P. W. H. Pinkse, and G. Rempe, *Cavity-enhanced Rayleigh scattering*, New J. Phys. **12**, 063022 (2010)

[113] P. Alsing, D. Cardimona, and H. Carmichael, *Suppression of fluorescence in a lossless cavity*, Phys. Rev. A **45**, 1793 (1992)

[114] D. Meschede, *Optics, Light and Lasers*, Wiley-VCH, Weinheim (2006)

[115] S. Inouye, A. Chikkatur, D. Stamper-Kurn, J. Stenger, D. Pritchard, and W. Ketterle, *Superradiant Rayleigh scattering from a Bose-Einstein condensate*, Science **285**, 571 (1999)

[116] U. Eichmann, J. C. Bergquist, J. J. Bollinger, J. M. Gilligan, W. M. Itano, D. J. Wineland, and M. G. Raizen, *Young's Interference Experiment with Light Scattered from Two Atoms*, Phys. Rev. Lett. **70**, 2359 (1993)

[117] J. Eschner, C. Raab, F. Schmidt-Kaler, and R. Blatt, *Light interference from single atoms and their mirror images.*, Nature **413**, 495 (2001)

[118] S. Reick, K. Mølmer, W. Alt, M. Eckstein, T. Kampschulte, L. Kong, R. Reimann, A. Thobe, A. Widera, and D. Meschede, *Analyzing quantum jumps of one and two atoms strongly coupled to an optical cavity*, J. Opt. Soc. Am. B **27**, A152 (2010)

[119] S. Gammelmark, W. Alt, T. Kampschulte, D. Meschede, and K. Mølmer, *Hidden Markov model of atomic quantum jump dynamics in an optically probed cavity*, Phys. Rev. A **89**, 043839 (2014)

[120] S. Zippilli, G. Morigi, and H. Ritsch, *Collective effects in the dynamics of driven atoms in a high-Q resonator*, Eur. Phys. J. D **31**, 507 (2004)

[121] J. Johansson, P. Nation, and F. Nori, *QuTiP 2: A Python framework for the dynamics of open quantum systems*, Comput. Phys. Commun. **184**, 1234 (2013)

[122] T. G. Tiecke, J. D. Thompson, N. P. de Leon, L. R. Liu, V. Vuletić, and M. D. Lukin, *Nanophotonic quantum phase switch with a single atom.*, Nature **508**, 241 (2014)

[123] T. Kuga, Y. Torii, N. Shiokawa, T. Hirano, Y. Shimizu, and H. Sasada, *Novel Optical Trap of Atoms with a Doughnut Beam*, Phys. Rev. Lett. **78**, 4713 (1997)

[124] L. You, X. Yi, and X. Su, *Quantum logic between atoms inside a high-Q optical cavity*, Phys. Rev. A **67**, 032308 (2003)

[125] J. Metz, M. Trupke, and A. Beige, *Robust Entanglement through Macroscopic Quantum Jumps*, Phys. Rev. Lett. **97**, 040503 (2006)

[126] M. Kastoryano, F. Reiter, and A. Sørensen, *Dissipative Preparation of Entanglement in Optical Cavities*, Phys. Rev. Lett. **106**, 090502 (2011)

[127] M. Baden, K. Arnold, and A. Grimsmo, *Realization of the Dicke model using cavity-assisted Raman transitions*, arXiv:1404.0512v (2014)

[128] B. Casabone, K. Friebe, B. Brandstätter, K. Schüppert, R. Blatt, and T. E. Northup, *Collective coupling between two ions and a cavity for an enhanced quantum interface*, arXiv:1408.6266v1 pp. 1–8 (2014)

Danksagung

Mein erster Dank gilt Herrn Prof. Dr. Meschede für die Möglichkeit meine Arbeit in seiner Forschungsgruppe anzufertigen. Sein Einsatz für Fördermöglichkeiten und das Ermöglichen eines breiten wissenschaftlichen Austausches mit anderen Forschungsgruppen auf der einen Seite, und seinen persönlichen Zuspruch wie auch „freie Hand“ im Labor auf der anderen Seite, möchte ich hier lobend erwähnen.

Herrn Prof. Dr. Schlemmer danke ich für sein Engagement als mein Mentor im Rahmen der Bonn-Cologne Graduate School (BCGS) und für die Übernahme des Zweitgutachtens.

Ich bin der Studienstiftung des deutschen Volkes und der BCGS für ideelle als auch finanzielle Förderung während meiner Promotion sehr dankbar.

Mit Tobias Kampschulte als meinem Seniordoktorand und Sebastian Manz als meinem Masterstudent hatte ich sehr gute Karten gezogen. Tobias beeindruckte durch tiefe Ruhe und tiefes Wissen. Basti war nicht minder fit im Kopf und brachte den Biss mit, der aus einem guten Studenten einen guten Forscher macht.

Für viele gute Beiträge zu dieser Arbeit möchte ich dem Austauschstudenten Hajime Shinohara, den Masterstudenten Stefan Brakhane und Martin Eckstein, meinen beiden Nachfolgedoktoranden Natalie Thau und Tobias Macha, wie auch den Postdocs Wolfang Alt, Seokchan Yoon und Lothar Ratschbacher danken.

Tobias Macha, Dank an Dich für Dein Engagement, dass sich durch die Teilnahme an Messungen unter verschäften Bedingungen in der Schlussphase meiner Laborzeit gezeigt hat. Wolfgang stand immer mit Rat und Tat bei zahlreichen technischen Problemen im Labor zur Verfügung. Auch außerhalb der offiziellen Teestundensprechzeit und selbst an Wochenenden durfte ich von seiner erstaunlichen Fähigkeit den Nagel auf den Kopf zu treffen häufig profitieren.

Zu beinahe allen Mitgliedern der AG Meschede hatte/habe ich ein sehr gutes Verhältnis. Von den heimlichen Herrschern des Instituts, den Damen und Herren aus der Verwaltung, kann ich nur Gutes berichten. Auch die Werkstätten erledigten meine Aufträge zuverlässig und gut.

Für das Lesen und Korrigieren von Teilen dieser Arbeit danke ich Wolfgang Alt, Lothar Ratschbacher, Carsten Robens und Anna Hambitzer. Dank geht an Tobias Macha für die Komplettdurchsicht der Arbeit kurz vor Torschluss.

Besten Dank an alle Mitautoren und im speziellen an Lothar Ratschbacher, Wolfgang Alt, Dieter Meschede und Tobias Kampschulte für eine gute und effiziente Zusammenarbeit während der Publikationen, die das Herzstück dieser Arbeit bilden. Dank geht an Søren Gammelmark für die Bereitstellung seines HMM-Codes.

Ein herzliches „Dankschön“ an meine beiden Mitbewohner Maroula und Matze; ohne euren Pasta- und Schlümpfesupport wäre ich in der letzten Woche des Zusammenschreibens wohl klapperdürr geworden. Zur Belohnung werde ich in Zukunft wieder häufiger das „Lied vom Birnbaam“ für euch singen.

Anna Hambi, Du Python-Maus, vielen vielen Dank für Geist und Tat, besonders in der heißen Schlussphase meiner Arbeit!